Gravitational Lenses & Conical Feedhorns

Conception Graphique Patrice Malo '91

Stephen Avrum Torchinsky, B.Eng. (McGill)
Department of Astronomy, University of Edinburgh
Doctor of Philosophy

1991

ABSTRACT

The emphasis of this thesis is on cosmology experiments using a submillimetre continuum array receiver. Divided into two parts, the thesis initially explores an astrophysical model, followed by an experiment based on results of the model. The second part deals with some of the design considerations for SCUBA, the Submillimetre Common User Bolometer Array. The thesis touches on all aspects of a problem in astronomy: the theoretical modelling, an observational experiment, and the development of instrumentation.

Part I deals with the astronomical question of gravitational lenses and the microwave background. Simulations of an anisotropic submillimetre background due to dusty primeval galaxies are presented, along with the observations that would result when gravitational lensing by clusters of galaxies is considered. The experiment was tried with the single pixel bolometer system on the James Clerk Maxwell Telescope and it measured an upper limit on CBR anisotropy of $\Delta T/T < 4.6\times10^{-3}$ (95% confidence) towards the cluster Cl 2244 at the angular scale of 5″. The small angular scale is due to the aid of the cluster lensing effect.

The second part looks at the extensive design considerations for the feedhorn antennas and the bolometer integrating cavities in SCUBA. Single mode optics optimizes aperture efficiency and this is usually achieved by having a length of waveguide, but analysis here shows that one can still have a single moded device without a waveguide. A filter drum furthers SCUBA's capabilities by allowing the detector arrays to operate at higher frequency wavebands, as well as the primary wavebands. At the higher frequencies the feedhorns are overmoded, which is a case investigated in this thesis. The SCUBA Project will have the horns fabricated by an outside contractor according to the specifications derived in Part II.

In accordance with University of Edinburgh regulation 3.4.7, I declare that this thesis has been composed by myself, and that it is my own work except where specific reference to previous work has been clearly indicated.

Stephen Avrum Torchinsky

22 July, 1991

ACKNOWLEDGEMENTS

Academic

By far my greatest gratitude goes to John Peacock who took me seriously when I said I wanted to do something in cosmology. He suggested the cluster lensing project in November '89, and though merely an adopted supervisor at a late stage in (my) life, he took on the role completely and never seemed to expect anything less from me than he would from any of his other students.

The SCUBA team led by Colin Cunnigham, was very supportive, and readily accepted me into the project team family, despite previous events and a reputation as a loudmouth american. Thanks for the many discussions, and for Colin's insistence that all analyses should be written out properly and submitted as SCUBA documents. It forced me to write things down, and made the thesis writing that much easier. I'll mention particularly Mel Strachan, Maureen Ellis, and especially Peter Hastings who eagerly entertained my visitors with a complete SCUBA/CAD tour whenever I brought someone around. I'm also greatly indebted to Anthony Murphy, who patiently answered numerous E-mail messages during '88 and '89 and set me straight on aperture efficiency, beam modes, and Gaussian beams. Thanks are also due Wayne Holland for doing all the hands-on dirty work for the feedhorn and bolometer tests.

The following people have been very helpful: Keith Ballard and Alan Heavens for random Gaussian fields, Lance Miller for statistics and gas in clusters, Karl Glazebrook for all his Fortran subroutines, Paul Mitchell (later S.A.Root) for a plethora of .COM files, Chris Collins for cosmology in general, Stuart Lumsden for observations of Cl 2244, Claire Chandler for the data reduction (rescue), Phil Blanco for emission from galaxies, Alistair Glasse for the sky transmission model in Chapter 6, and Peter Brand for enthusiastic discussions on all subjects of my choosing, and his.

I'd also like to thank the following readers: John Peacock, Alan Heavens, Lance Miller, John Cooke, Adrian Webster, and everyone who gets beyond the next two pages.

The frontispiece depicting the JCMT observing submillimetre arcs from gravitational lensing was expertly drawn by Patrice Malo, Graphiste.

Financial

I list my funding in order of magnitude: The Natural Science and Engineering Research Council of Canada provided me for the final two years, and I'm very grateful to Morley Bell and to Paul Feldman who fought so valiantly to convince NSERC that I should be awarded the scholarship. The Committee of Vice-Chancellors of Great Britain gave me an Overseas Research Award which brought my fees as a bloody foreigner of $\sim$£5000 down to the $\sim$£2000 that "home" students pay (*i.e.* SERC pays). Funding for the observing trip described in Chapter 4 was very generously provided by the Panel for the Allocation of Telescope Time (operated by SERC), and I'm grateful to Liz Gibson and John Cooke for dealing with the administrative headaches involved. The government of Québec guaranteed and paid the interest on loans during my 3+ years in Edinburgh. My Mom and my Dad contributed during my first, lean, year so that I could live like a mensch, and also payed for a couple of trips back to the Old Country. I gave Astronomy tutorials during the '88-'89 year ($\sim$£300). Finally, the Department of Astronomy waived my "Research Costs" during the '88-'89 year (£400), and they paid for the flight to the land of my ancestors (£300).

Otherwise

First of all, is my mate Dutch Peter Visscher who was there for me throughout, right from the time of Mad Mary of Morningside; Andrea Menn with whom I stormed around Scotland in '88; The denizens of 11 Marchmont Road: Mark Wiegand and Paul McIlvenny who rescued me from Morningside, Rockin' Keith Burns, Geoff Craig, et puis toutes les Filles de Marchmont: Sarah Wilson, Nathalie Verschelde, et surtout, d'abord, ma jolie Sorcière bien aimée, Valérie Combes qui souffrait tous avec moi pendant les dernières mois. I'd like to thank Dr. Nandy for being such a reasonable landlord, and especially for the automatic washing machine.

[The Greats that went before me: JAMES DUNLOP! Andrewwww Mead; Phil Puxley (still the Greatest); and the Alright Rev. Tobes Moore who actually had enough faith in me to brave the harsh winters of the New World and take a job in Ottawa; Stuuuuuuuuuuuuuuuuuaaaaaaaaaaaaaaaaaaarrrrrrrrrrrrrrrt; and of course the very, very Groot, Shepherd A Root.] [I'm grateful to Moorhouse for leaving us his cassette

player, to Phil Blanco and Phillippe Eenens for their late night company towards the end.] [My contemporaries: Claire (especially for her non-linear moments), Keef, Penny and Karl.] [And some of the Kids: Big Boy BBBBbbbbBy Nichol, Thonio (where should we go now?), Suzie the other Techie, Pippa (thanks for doubling the jewish population), Kathy (phwoar), and Bob Mann (King of Social Organization).] [New Oldies: Phil James, and tea drinkin' Tom Broadhurst] [Chris Collinses: Chris Collins and Lorenzo's, Chris Collins and Chinese Home Cooking, Chris Collins and Mama's, Chris Collins and Jacques Derrida. (Je parlerai donc d'une thèse.

Contents

List of Acronyms and Abbreviations

CBR	Cosmic Blackbody Radiation
CDM	Cold Dark Matter
cD	cluster "D" galaxy
CNC	Computer Numerically Controlled
COBE	Cosmic Background Explorer
dec	declination
DIRBE	Diffuse InfraRed Background Experiment
FIRAS	Far InfraRed Absolute Spectrophotometer
FWHM	Full Width Half Maximum
IRAM	Institut de Radio Astronomie Millimétrique
JCMT	James Clerk Maxwell Telescope
L-G	Laguerre-Gauss
NRC	National Research Council (Canada)
NWO	Nederlandse Organisatie voor Wetenschappelijk Onderzoek
RA	Right Ascension
ROE	Royal Observatory, Edinburgh
rpm	revolutions per minute
SCUBA	Submillimetre Common User Bolometer Array
SERC	Science and Engineering Research Council (United Kingdom)
S-Z	Sunyaev-Zel'dovich
TE	Transverse Electric
TM	Transverse Magnetic
UKT14	United Kingdom Telescope instrument # 14

1 Introduction

In recent years, observations at wavelengths shortward of 1 mm and longward of $\sim 200\,\mu$m have been actively pursued. This submillimetre region is particularly interesting from the point of view of star formation studies, as well as observational cosmology. As to the former, future submillimetre observations promise to uncover dust enshrouded protostars in the process of becoming stars. In cosmology, the existence of the Cosmic Background Radiation makes submillimetre observations essential. The CBR can be used as a diagnostic by studies of its spectral and spatial morphologies, and also by using it as a background source to fuel foreground effects such as Compton scattering in clusters of galaxies (the Sunyaev–Zel'dovich effect), or gravitational lensing by massive objects such as clusters or strings. This thesis is concerned with the latter effect, and explores the possibility of detecting an anisotropic excess to the CBR which might arise from an early population of dust covered primeval galaxies. Gravitational lensing by a galaxy cluster can amplify the flux from such a source by redirecting stray photons into the telescope beam.

Opening the submillimetre window to the universe is technologically non-trivial, which explains the relative newness of the field. Aspects of radio astronomy at one end, and infrared astronomy at the other are brought together to create this new submillimetre regime. Detectors need to be cooled in order to be sensitive to the "heat" radiation from submillimetre sources as in the infrared, however, the detectors cannot lie naked on a chip as in an infrared array. Instead, the radiation must be collected by a feedhorn antenna and waveguide system, and then dumped onto the detector which sits in an integrating cavity. This is the well understood radio technique, with the important difference that radio detectors need not be cooled to temperatures in the region of 1 K. Technologically, the submillimetre regime brings together aspects of radio and infrared astronomy, and also introduces the concept of single moded optics which improves aperture efficiency.

Ever since Galileo first used a telescope to view the moon in 1610 astronomers have been intimately involved with the development of new instruments. Most often, the needs of a specific experiment governs the direction in which instrumentation progresses. In some cases, scientific research progresses by the influence of existing technology, and an available instrument will inspire a new experiment. Galileo's scientific leap forward took this path when he applied the already common mariner's tool of the telescope to astronomy.

A submillimetre continuum camera called SCUBA (Submillimetre Common User Bolometer Array) is being developed at the Royal Observatory Edinburgh, perhaps mainly for galactic astronomy, but there are many applications to observational cosmology. The present thesis investigates a way in which SCUBA can be used to search for primeval galaxies by using the gravitational lens effect of clusters of galaxies, and it also presents some of the technical considerations involved in designing the feedhorn antennas for the camera. The Cosmic Background Radiation makes submillimetre astronomy in cosmology essential, and experiments can be designed with SCUBA in mind.

Organization of the Thesis

This thesis is organized into two main parts emphasizing first the astronomy and then the receiver development. The underlying theme is Submillimetre Continuum Astronomy, and the thesis follows a progression from developing an astrophysical model through the observational experiment associated with the model, and finally to some of the details involved in designing an instrument that will improve the experiment.

Part I begins in Chapter 2 with a review of some of the theory in galaxy formation models which postulate the existence of a submillimetre background radiation due to primeval galaxies. In addition, the Sunyaev-Zel'dovich effect is also reviewed in Chapter 2. Chapter 3 presents the development of a model to simulate the gravitational lens effect of clusters. The anisotropic submillimetre background is modelled using a Gaussian power spectrum approach, and this is used in turn as the source field which undergoes gravitational lensing. Simulations of particular clusters are presented along with a discussion. The results are important within the context of the Sunyaev–Zel'dovich effect. Chapter 4 presents the results and data analysis from a submillimetre observing run that attempted to detect the amplified flux due to gravitational lensing

described in Chapter 3.

The sensitive measurements required are perhaps beyond the scope of the instrument used for the observations of Chapter 4, and this leads naturally to the second part of the thesis. Bolometer sensitivities have been improved with new cryogenic techniques bringing temperatures down to 0.1 mK, and to go along with this, submillimetre continuum receivers should employ single mode optics to reduce background loading. Part II investigates conical feedhorn and integrating cavity design for the Submillimetre Common User Bolometer Array which will eventually be used on the James Clerk Maxwell Telescope. In particular, a proper understanding of wave-mode attenuation in feedhorns is presented in Chapter 6, and also feedhorns which are overmoded are properly analyzed in Chapter 7. The behaviour of radiation inside the integrating cavity is the subject of Chapter 8.

Finally, the summary in Chapter 9 also includes some suggestions for future cosmology work for SCUBA.

Part I

Modelling and Observation of the Microwave Background

2 Introduction to Part I

The most powerful diagnostic in cosmology is the Cosmic Blackbody Radiation (CBR) and in particular, the spectral and spatial non-uniformities that might exist. Departure from a perfect blackbody spectrum, and anisotropy on different angular scales are probes of the early universe that provide the only observational clues to galaxy formation. Quantifying and identifying any bump in the background radiation is vital for the understanding of cosmology.

One modification to the CBR which occurs well after its origin, is the Sunyaev-Zel'dovich effect. The validity of this effect is the only generally accepted CBR distortion which has yet to be satisfactorily detected by observations. This consensus amongst theorists is due to to the very minimal assumptions that require the existence of the S-Z effect. One need only postulate that a background radiation field exists originating from a source behind a mass of hot gas. The detection of X-ray emission from clusters of galaxies clearly indicates that hot gas exists between the galaxies, and only a handful of people take exception to the assumption that the background blackbody radiation is cosmological [Arp *et al.* 1990]. The S-Z effect is of small magnitude, but it has great potential as a cosmological probe, most significantly as an independent measure of the Hubble time H_0^{-1}.

Another well understood phenomenon is the action of light being deflected by massive objects through the force of gravity. A gravitational well, such as a galaxy cluster, can be considered as a lens refracting background radiation generally towards an observer. As with the S-Z effect, this is an experiment involving observations towards a cluster of galaxies. In microwave astronomy, gravitational lensing by clusters has not had the great attention given to the S-Z effect because fluctuations on the CBR are required in order to make it an interesting investigation. Nevertheless, it is at the submillimetre wavelengths, and at angular scales less than $10''$ that non-uniformities in

the CBR are most likely to occur. There is great potential for gravitational lenses to probe for anisotropies in the CBR at very small angular scales.

With the advent of submillimetre imaging devices, such as the Submillimetre Common User Bolometer Array (SCUBA), the time is ripe for microwave searches for background anisotropy, using the enhancing capabilities of a huge gravitational lens. The background sources are effectively spread out by the gravitational lens since photons which would otherwise go elsewhere are re-directed towards the observer. Consequently, anisotropies in the cosmic background are lensed-up to appear at larger angular scales. Gravitational lensing by clusters can be used in this way to probe the small scale angular anisotropy which would otherwise be beyond the capability of telescope beams.

1.1 Dusty Primeval Galaxies

Galaxy formation models must accurately describe the nature of a microwave background, and this has proven a difficult task, but one theory which has been particularly successful to date, and so acquired the monicker "standard", is the standard Cold Dark Matter (CDM) model of cosmology [see *e.g.* Blumenthal *et al.* 1984]. The universe undergoes an initial inflationary period of exponential expansion and this predicts a critical ($\Omega = 1$) universe [Guth 1981]. After a radiation dominated phase, recombination occurs and the thermal radiation from this "surface of last scattering" reaches us as the well known CBR. Galaxy formation in the standard model is described as hierarchical, in which small structures form first and these eventually amalgamate into larger structures forming the galaxies, clusters of galaxies, and clusters of clusters.

The smoothness of the CBR, both spectrally, and spatially, impose very rigid constraints on the hierarchical theories of galaxy formation. The CBR is known to be highly thermalized [Mather *et al.* 1990] and spatially very smooth [see Kolb & Turner 1990] except for a well measured dipole which is interpreted as arising from our peculiar velocity with respect to the CBR. The CBR reaches us basically unhindered right from the surface of last scattering, and is therefore a direct indication of the smoothness of the universe at that early time. However, in order for hierarchical galaxy formation to occur, there must have been perturbations in the original mass distribution. These bumps would act as the gravitational wells towards which particles stream, and in this way structure is built up as blobs coalesce and eventually form stars, galaxies and clus-

ters. The bumps in this initial mass spectrum would necessarily be evident in the CBR, however observations show severe lower limits on angular anisotropy and this in turn limits the amount of structure that can form within the standard CDM model, yet large scale structure must still be explained [Maddox *et al.* 1990, Collins *et al.* 1991]. The standard model, although successful in many respects, must still reconcile the apparent paradox of CBR smoothness and the large scale structure observed in the later universe, but refinements to the theory may prove successful [see *e.g.* Peacock 1991].

Early galaxies, or proto-galaxies, are thought to form their initial population of stars rapidly, in a burst. Local observations support this assumption in that Milky Way halo stars with large orbital eccentricities (and which are therefore very old) are also comprised partly of metals, so there must have been a generation of stars before them [Partridge 1974]. The existence of highly luminous, star bursting galaxies, such as Arp 220, also lend credence to the hypothesis that first galaxies formed stars in brief burst.

Mostly, the first galaxies would all have formed within a relatively short time span when the universe was $\sim 10\%$ of its present age (at redshift, $z \simeq 10$). Extragalactic observations help define the epoch of galaxy formation. Quasars as far away as $z = 4.7$ have been detected and their redshifts measured by emission features of metals. It must be deduced that star formation has occured previous to that time.

Searches for primeval galaxies have polarized into two camps: dust *vs.* no dust. In the first case, the idea is that a brief but furious burst of star formation, and the subsequent violent death of short lived, massive stars gives rise to large amounts of dust enveloping the next generation of stars. Such a dusty shroud will reprocess most of the light, and the re-radiation will be in the far infrared, and the submillimetre wavebands. On the other hand, if the primeval galaxies do not form stars in a very short lived dust producing phase, then the ultra luminous primeval galaxies at large redshifts will be near-infrared sources. The present thesis is concerned with submillimetre continuum detectors, so that the dusty primeval galaxy scenario is chosen here, and in particular, the possibility of using gravitational lensing to help the search for primeval galaxies is investigated.

Bond, Carr & Hogan [1986, 1990] have done extensive calculations incorporat-

ing dust grain shapes, emissivity and distribution, as well as epoch of galaxy formation ($10 \gtrsim z \gtrsim 2$) and predict departure from a perfect blackbody of magnitudes up to $\Delta T/T \simeq 10^{-3}$ at angular scales of the order of $10''$. They provided predictions for future experiments with various instruments including the Submillimetre Common User Bolometer Array (SCUBA, see Part II) and the already highly successful Cosmic Background Explorer (COBE) [Mather 1982, Gulkis *et al.* 1990, Mather *et al.* 1990]. COBE measured the CBR with a 7° beam and found the submillimetre background to be a Planck function to within 1% peak flux in the range $10\,\mathrm{mm} < \lambda < 0.5\,\mathrm{mm}$. Despite COBE, there is still room for significant anisotropy and dust excess levels, especially at the shorter wavelengths ($\lambda < 500\,\mu\mathrm{m}$), and the 14 models in Bond *et al.* are designed to survive the COBE result.

2.2 The Sunyaev - Zel'dovich Effect

Photons from the CBR passing through the hot gas of a galaxy cluster are Compton scattered with the less energetic ones (Rayleigh-Jeans) mostly taking energy from the hot electrons. All the photons pass through the hot gas and when an observer sees them, there are fewer Rayleigh-Jeans photons, and more Wien photons. This is the Sunyaev-Zel'dovich (S-Z) effect.

First proposed in 1969 [Zel'dovich & Sunyaev] and later applied to observations of galaxy clusters [Sunyaev & Zel'dovich 1972], the exciting potential of the S-Z effect as a probe of the early universe was soon appreciated. Originally, Sunyaev and Zel'dovich intended the effect as a method of determining the characteristics of the hot gas in clusters (electron temperature, and mass), however, combined with X-ray observations, detection of the S-Z effect can in principle lead to a calculation of the cluster's angular diameter distance, independent of the distance ladder based on standard candles, and more importantly independent of cosmological assumptions (Ω_0, H_0). The S-Z effect could then provide a measurement of H_0 [Silk & White 1978].

Furthermore, since the effect has a specific wavelength dependency, a shifted S-Z spectrum is a direct measurement of the cluster's velocity relative to the CBR [Sunyaev & Zel'dovich 1980a,b]. Knowledge of peculiar velocities would greatly constrain galaxy formation models by allowing a distinction between cosmological and Doppler redshift. In this way, the gravitational interaction between clusters of galaxies could be separated

from the effect of the expansion of the universe.

With such fruits to bear, the S-Z effect has naturally incurred the interest of a number of ambitious observers [Birkinshaw *et al.* 1978, Birkinshaw 1979, Birkinshaw *et al.* 1981a,b; White & Silk 1981; Andernach *et al.* 1983; Birkinshaw & Gull 1984; Birkinshaw *et al.* 1984; Chase 1985 and references therein]. A tentative measurement of the effect in the cluster 0016+16 of $\Delta T/T = -1.38\,\mathrm{mK}$ at 10.7 GHz has been reported, but to date no measurement of the corresponding submillimetre increment has been made. There is no general agreement that a detection of the S-Z effect has occurred, and this is due mostly to the very great difficulty imposed by an experiment in which the desired signal is expected to be five orders of magnitude less than the CBR itself.

The S-Z effect can be derived from the Kompaneets equation [1956] which is the general kinetic equation for plasmas:

$$\frac{\partial N}{\partial t} = \frac{\sigma_{\mathrm{T}} n_{\mathrm{e}} h}{m_{\mathrm{e}} c} \nu^{-2} \frac{\partial}{\partial \nu} \nu^4 \left(N^2 + N + \frac{kT_{\mathrm{e}}}{h} \frac{\partial N}{\partial \nu} \right), \tag{2.1}$$

where $N = (c^2/2h)\nu^{-3} F_\nu$ is the occupation number of photons. When the background spectrum is much smaller than the electron brightness temperature, $T_{\mathrm{B}} \ll T_{\mathrm{e}}$ the final term on the right hand side of Eq. 2.1 dominates the process and the following is derived:

$$\frac{\partial N}{\partial t} \simeq \frac{\sigma_{\mathrm{T}} n_{\mathrm{e}}}{m_{\mathrm{e}} c} kT_{\mathrm{e}} \left(4\nu \frac{\partial N}{\partial \nu} + \nu^2 \frac{\partial^2 N}{\partial \nu^2} \right), \tag{2.2}$$

which is the first order Fokker-Planck expansion of Compton scattering. The first term can be considered as the contribution by 'convection': In this case, the net energy gain from Compton scattering (or 'mixing'). The second is a 'diffusion' term which describes how the background energy is spread out across the spectrum. Both these terms are essential to give a proper estimate of the effect. When the illuminating background blackbody is inserted in Eq. 2.2 a correction to the observed spectrum is deduced:

$$\Delta F_{\mathrm{SZ}} = y F_{\mathrm{B}} \left[x \left(\frac{e^x + 1}{e^x - 1} \right) - 4 \right] \left(\frac{x e^x}{e^x - 1} \right) \; + \; \mathrm{O}(\tau_{\mathrm{T}}^2). \quad x = \frac{h\nu}{kT_{\mathrm{B}}}. \tag{2.3}$$

Eq. 2.3 is correct to first order in the optical depth τ_{T}. The Comptonization parameter y is

$$y = \frac{kT_{\mathrm{e}}}{m_{\mathrm{e}} c^2} \tau_{\mathrm{T}}, \qquad \tau_{\mathrm{T}} = \int \sigma_{\mathrm{T}} n_{\mathrm{e}} dl. \tag{2.4}$$

In the limits of small x (Rayleigh-Jeans) and large x (Wien) one can see the qualitative effect is that of creating a decrement at the longer wavelengths

$$\Delta F_\nu \simeq -2yF_\nu$$

and an increment in the background spectrum at the shorter wavelengths

$$\Delta F_\nu \simeq yF_\nu(x-4)x.$$

The S-Z effect is a shift of the blackbody spectrum towards the higher frequencies. The magnitude of the decrement/increment is shown in Fig. 2.1.

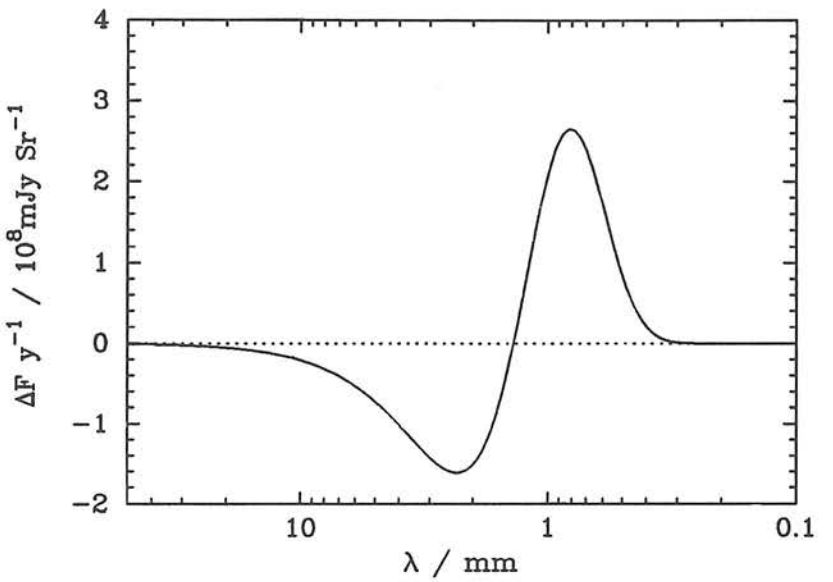

Figure 2.1: *The S-Z effect modifies the blackbody spectrum by a decrement at wavelengths shortward of the peak, and an increment at wavelengths longward of the peak.*

2.2.1 Determination of H_0 with the S-Z Effect

The method of using a measurement of the S-Z effect along with X-ray observations to determine the deceleration parameter q_0 was first outlined by Silk & White [1978]. This is equivalent to finding the density parameter Ω_0 in a universe with no cosmological constant. It is also possible to use this experiment to find the present Hubble parameter H_0. The first step towards H_0 begins with X-ray observations of the candidate cluster in order to determine the electron temperature T_e. Assuming an isothermal,

uniform gas cloud in a spherically symmetric galaxy cluster, the surface brightness of the X-ray bremsstrahlung in the direction to the centre of the cloud is

$$I_X = 2Ar_c n_e T_e^{-\frac{1}{2}} e^{x_e} g \tag{2.5}$$

where A is a constant, r is the radius of the cloud, n_e is the electron number density, and g is the Gaunt factor. Observations on either side of $x_e = 1$ (*ie.* $h\nu < kT_e$ and $h\nu > kT_e$) allow the determination of the electron brightness temperature. Knowing the shape of the X-ray surface brightness spectrum suffices to achieve this. A measurement of the S-Z effect (Eq. 2.3) then gives the electron number density n_e once the electron temperature is known. Going back to the X-ray brightness (Eq. 2.5), the angular diameter of the cloud is solveable. The absolute radius of the cloud, along with its angular extent simply lead to the angular diameter distance

$$D_a = \frac{r_c}{\theta} = \frac{2c}{H_0\Omega_0^2(1+z)^2}\left[\Omega_0 z + (\Omega_0 - 2)\left(\sqrt{1+\Omega_0 z} - 1\right)\right] \tag{2.6}$$

$$= \frac{cz}{H_0} \qquad \text{for small } z$$

Organization of Part I

Part I of this thesis is composed of the following two chapters in which first of all a model of galaxy clusters as gravitational lenses is developed. It will be shown how this effect enhances anisotropy in a background field from 5″ scale up to 10″ or 20″. This is compared to the S-Z effect of various clusters. The last chapter of this part presents the results of a submillimetre observation towards the cluster Cl 2244. This was a single pixel experiment which measured an upper limit on anisotropy towards Cl 2244 of $\Delta T/T < 4.6\times10^{-3}$ (95% confidence) on an angular scale of of $\sim 5''$. The small angular scale is achieved through the gravitational lens effect.

3 The Microwave Background through Clusters

The bending of light by the force of gravity has been a well understood phenomenon since 1919 when Einstein's theory of General Relativity established its validity during the total eclipse of that year. Alignment of a source and lens (some massive object) with the observer could result in light from the source reaching the observer from several paths forming an "Einstein Ring" [Einstein 1936]. In circumstances when the source is slightly off line, partial rings, or arcs are formed. This is the case in the recent discovery by Soucail *et al.* [1987a,b, 1989; Fort *et al.* 1988] of "Luminous Arcs" found in the clusters Abell 370, Cl 2244−02 [Lynds & Petrosian 1986, 1988; Petrosian 1989], and eight other clusters [Fort 1990] which are the first observed incidents of gravitational lensing where the lens is a cluster of galaxies. The importance of this discovery is immense: understanding the morphological distortion by lensing of an extended background source is a direct probe of the matter distribution in the lensing object, which turns out to be mostly the dark inter-galactic matter. Furthermore, the cluster itself can be used as as a giant telescope with which to probe the population of high redshift normal galaxies [Tyson 1990].

The modelling presented in this chapter is mainly motivated by the possibility of searching for CBR anisotropy using gravitational lensing, but the relevence in the context of the S-Z effect is also important. Gravitational lensing of a bumpy submillimetre background will interfere with the S-Z effect. The action of the cluster as a gravitational lens would yield a measurement of CBR anisotropy different from that of a normal anisotropy experiment, and this could naively be attributed to the S-Z effect.

Chapter Organization

Section 3.1 reviews the basic theory of gravitational lenses, in particular setting up the scheme for simulating the effect of general mass distributions. This is followed

in Section 3.2 with models for the mass distributions in clusters of galaxies, and then Section 3.3 with models of the gas distribution in clusters which is used to compute the S-Z effect. In Section 3.4 a model is developed which mimics the expected emission from a population of dusty primeval galaxies, and the morphology of this population is simulated by the random Gaussian fields generated in Section 3.5. Finally the simulations of observations through three specific clusters is presented in Section 3.6. An important conclusion is that gravitational lensing of background submillimetre sources, and the S-Z effect are competing or complementary effects of the same order of magnitude. The Chapter also shows that gravitational lensing by clusters of galaxies is a useful tool for probing background anisotropy. This is discussed in Section 3.7.

3.1 Gravitational Lensing by Clusters

The schematic of a simple gravitational lens system in Figure 3.1 shows a spherically symmetric mass distribution L inflicting a gravitational acceleration radially inwards on the light ray originating from the source S. The analysis which follows is well understood, and a review of the basic theory can be found in Blandford & Kochanek [1987a]. The transverse impulse imparted on a passing photon is given by General Relativity as twice that expected by a Newtonian argument:

$$\dot{p}_\perp = 2ap_0/c \tag{3.1}$$

where a is the acceleration due to gravity, and p_0 is the photon momentum.

The angular change of direction of the light ray in a time dt (*i.e.* along the light path $d\ell$) is then $d\alpha_0 = (dp/p_0)$ and so the total deflection α_0 is the integrated deflections suffered by the photon along the light path ℓ:

$$\alpha_0 = \int_{t_1}^{t_2} \frac{1}{c}\frac{\dot{p}}{p_0} c dt = \frac{2}{c^2}\int_{-\infty}^{\infty} a d\ell \tag{3.2}$$

From Figure 3.1, geometric argument easily shows the relationship between the observer-source angle φ, the observer-image angle θ, and the deflection angle α_0. This is the so called "lensing equation":

$$D_{\rm OS}(\theta - \varphi) = D_{\rm LS}\alpha_0,$$

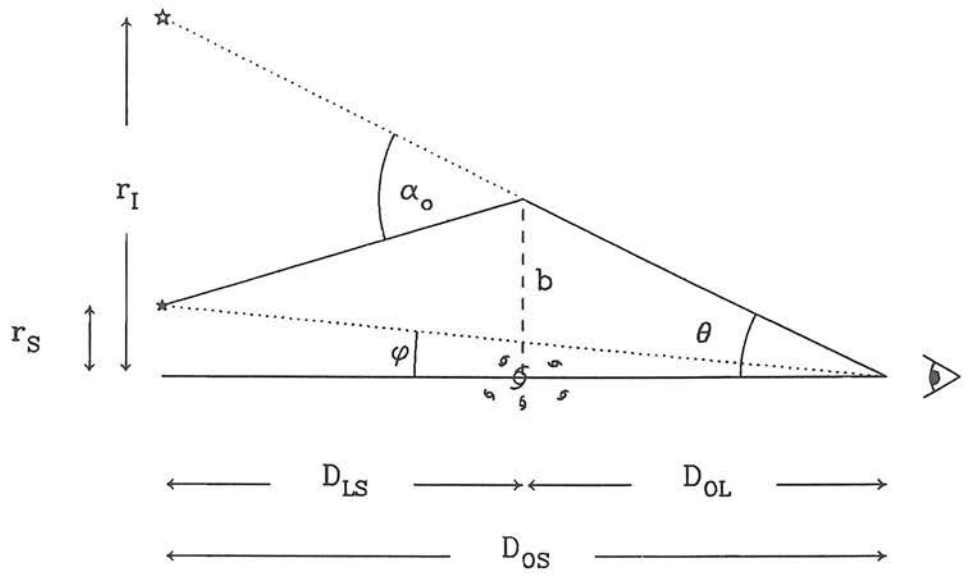

Figure 3.1: *The gravitational lens system. A mass distribution L is responsible for the gravitational deflection for light from the source S to the observer O. The angles α_0, φ, and θ are here exaggerated for clarity. All distances are angular diameter distances.*

which can be easily generalized to include the plane orthogonal to the one shown in Fig. 3.1

$$D_{\rm OS}(\vec{\theta} - \vec{\varphi}) = D_{\rm LS}\vec{\alpha}_0, \tag{3.3}$$

where $\vec{\theta}$, $\vec{\varphi}$ and $\vec{\alpha_0}$ are now 2D vectors on the sky. The distances from the observer to the lens, to the source, and from the lens to the source ($D_{\rm OL}$, $D_{\rm OS}$ and $D_{\rm LS}$ in Fig. 3.1) are the angular diameter distances in a given cosmology and are derived from Weinberg [1972 Eq. 15.3.23]:

$$D_{\rm AB} = \frac{2c}{H_0\Omega_0^2(1+z_{\rm B})}\left[2\left(\frac{\Omega_0-1}{1+z_{\rm B}} - \frac{\Omega_0-1}{1+z_{\rm A}}\right) + \frac{\sqrt{1+\Omega_0 z_{\rm A}}}{1+z_{\rm A}} - \frac{\sqrt{1+\Omega_0 z_{\rm B}}}{1+z_{\rm B}}\right]. \tag{3.4}$$

The deflection angle α_0 is a function of the "impact length" $b = D_{\rm OL}\theta$.

The acceleration of a beam of radius θ (within the impact radius b) relative to itself is $a = 4\pi G\rho b$ from which the gravitational deflection angle can be derived in terms of the mass within the beam $M(b)$

$$\alpha_0 = \frac{4G}{c^2}\frac{M(b)}{b}. \tag{3.5}$$

Two extreme examples as an illustration are the point mass lens, and the isothermal singular spherical mass distribution. The deflection angle in the case of the former is given directly by Eq. 3.5. The singular isothermal mass distribution, which has an inverse square dependence on distance,

$$\rho = \sigma_{\rm v}^2/2\pi G r^2 \tag{3.6}$$

generates a constant angle of deflection, independent of the impact parameter;

$$\alpha_0 = \text{const} = 4\pi\sigma_{\rm v}^2/c^2, \tag{3.7}$$

where $\sigma_{\rm v}$ is a characteristic velocity dispersion of the mass distribution (the one measured at large distance from the centre).

Instead of the mass density ρ, a useful tool is the mass potential Ψ, defined by Poisson's equation,

$$\nabla_{\rm 3D}^2\Psi = 4\pi G\rho(\vec{r}), \tag{3.8}$$

or this can be projected onto the plane of the sky and the two-dimensional mass distribution potential is derived:

$$\nabla_{\rm 2D}^2\Psi = 4\pi G\Sigma(\vec{r}), \tag{3.9}$$

where derivatives are taken with respect to the space coordinates at the plane of the lens. The deflection angle is then simply $\alpha_0 = \nabla\Phi$ with

$$\Phi = \frac{2}{c^2}\frac{D_{\rm OL}D_{\rm LS}}{D_{\rm OS}}\Psi.$$

The lensing equation (Eq. 3.3) is re-organized to create the deprojection equation

$$\vec{r}_{\rm S} = \vec{r}_{\rm I} - \vec{\nabla}\Phi. \tag{3.10}$$

In this way, a given point on the image plane can be mapped (deprojected) to its position on the source plane. Note that the image to source mapping is many to one, and it is therefore easier to begin on the image plane.

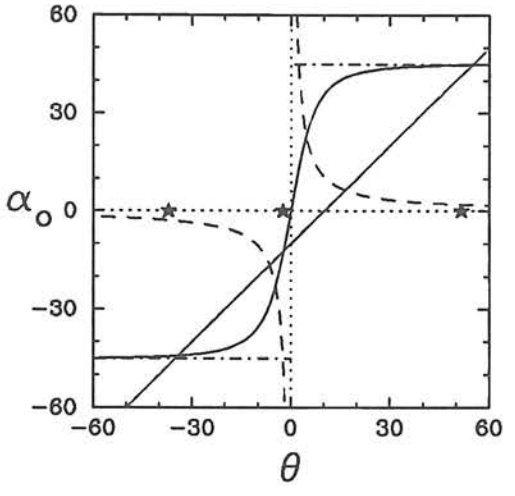

Figure 3.2: *The deflection angle for the mass distribution approximating Abell 370 is plotted against image position angle θ; all angles are measured in arcseconds. The straight line corresponds to the left hand side of the lensing equation (Eq. 3.3) with the source position angle $\varphi = 10''$. Intersection of the straight line with the $\alpha_0(\theta)$ line indicates the image locations (denoted by stars). There are three images, but for source positions greater than $\sim 15''$ there is only one image. The dash-dot line corresponds to the constant deflection angle of a singular isothermal mass distribution with the same velocity dispersion as A370, and the dashed line is for the point mass lens.*

3.2 Cluster Mass Models

The "best model" of Grossman & Narayan [1989, hereafter GN] quite successfully reproduces the position and morphology of the main arcs seen in A370. The elliptical generalization of a two dimensional, isothermal, non-singular mass distribution (Eq. 3.11) simulates the intra-cluster dark matter between the galaxies which turns out to be the dominant factor in the lensing effect.

$$\Sigma(\vec{r}) = \frac{\sigma_v^2}{2Gr_c}\left[1 + (1-\epsilon)\frac{x^2}{r_c^2} + (1+\epsilon)\frac{y^2}{r_c^2}\right]^{-\frac{1}{2}}. \tag{3.11}$$

The galaxy cluster is thus characterized by the asymptotic velocity dispersion σ_v, the core radius r_c, and the ellipticity ϵ.

GN start with the mass distribution and integrate to get the deprojection (Eq. 3.10). The present analysis follows that of Kochanek & Blandford [1987, hereafter KB] who start with the mass potential and differentiate to get the deprojection (Eq. 3.10) – a

numerically easier task. The potential used is non-singular, ellipsoidal, and, with an appropriate choice of α, it behaves as an isothermal distribution at large distance from the centre.

$$\Psi = \frac{2\pi r_c \sigma_v^2}{3\alpha}\left(\left[1+(1-\epsilon)\frac{x^2}{r_c^2}+(1+\epsilon)\frac{y^2}{r_c^2}\right]^{\alpha}-1\right), \tag{3.12}$$

where α is the called the *softness* (not to be confused with the deflection angle α_0). The mass distribution is easily found from the potential using Poisson's equation,

$$\Sigma(\vec{r}) = \frac{2\sigma_v^2}{3Gr_c}\left[1+(1-\epsilon)\frac{x^2}{r_c^2}+(1+\epsilon)\frac{y^2}{r_c^2}\right]^{\alpha-2}\left[1+\alpha(1-\epsilon)\frac{x^2}{r_c^2}+\alpha(1+\epsilon)\frac{y^2}{r_c^2}\right], \tag{3.13}$$

and the mass distribution of KB is then similar to GN when the softness $\alpha \simeq 0.6$ (see Fig. 3.3).

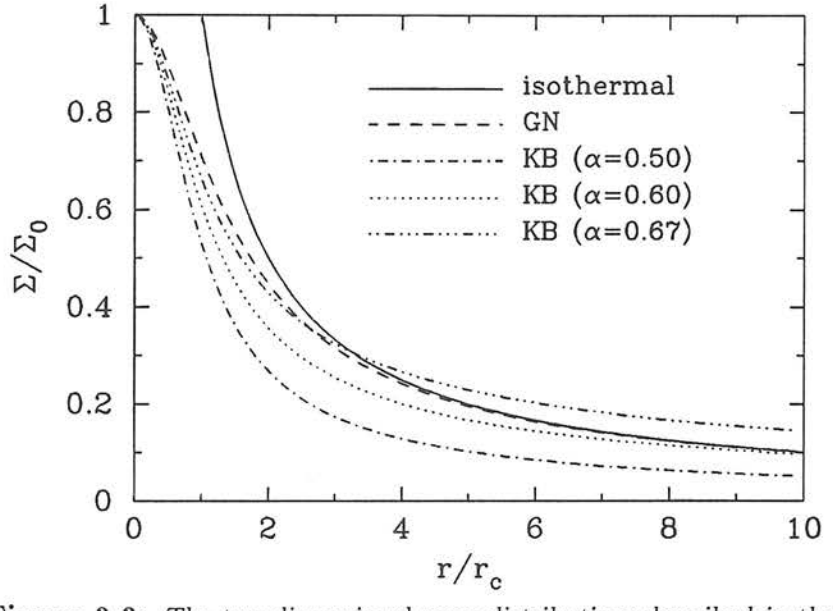

Figure 3.3: *The two dimensional mass distributions described in the main text are plotted here along with the theoretically ideal case of the spherically symmetric, isothermal mass distribution. The distribution of KB is similar to that of GN for $\alpha = 0.6$. The distribution of GN is a slightly better approximation to the isothermal distribution.*

Although in the thin lens analysis above, the two dimensional mass distribution is all that is needed, for the calculation of the Sunyaev–Zel'dovich effect discussed later (Section 2.2) the full three dimensional mass distribution is required. The two dimensional distribution is easily derived from the three dimensional distribution by a projection along the line of sight,

$$\Sigma(\vec{r}) = \int_{-\infty}^{+\infty} dz\, \rho\left(\vec{R}\right). \tag{3.14a}$$

For rigour, $\vec{r}$ is the angular position vector on the sky, but for the cluster radii of interest, these are small enough to be directly related to the physical radius. The spherical radius $\vec{R}$ is related to the cylindrical radius in the usual way ($R^2 = r^2 + z^2$). One can recover the three dimensional distribution from the two dimensional distribution after some assumptions are made. For example, if an observed circular distribution arises from a spherically symmetric three dimensional mass distribution, then the deprojection can be derived as in KB:

$$\rho(\chi) = \frac{1}{\pi r_c} \int_{\infty}^{\chi} \frac{d\Sigma(\chi')}{d\chi'} \frac{d\chi'}{\sqrt{\chi' - \chi}} \qquad \text{[Eq'n A3 of KB]} \tag{3.14b}$$

where $\chi = r^2/r_c^2$. Hence for circular models, the three dimensional mass distribution of KB derived from Eq. 3.13 is the following:

$$\frac{\rho}{\rho_0} = \left(1 + \frac{R^2}{r_c^2}\right)^{\alpha - 5/2} \left(1 + \frac{2\alpha}{3} \frac{R^2}{r_c^2}\right) \tag{3.15a}$$

For GN it is

$$\frac{\rho}{\rho_0} = \left(1 + \frac{R^2}{r_c^2}\right)^{-1}. \tag{3.15b}$$

These are plotted in Fig. 3.4.

The two dimensional elliptical mass distribution of Eq. 3.13 can arise from a variety of three dimensional configurations which can be described as a disk or rugby ball at various inclinations to the line of sight. In order to generalize the cluster model to non-spherical distributions, one can replace R^2 in Eqs. 3.15 by $R_\epsilon^2 = \epsilon_x x^2 + \epsilon_y y^2 + \epsilon_z z^2$, with $\epsilon_x + \epsilon_y + \epsilon_z = 1$. The ellipticity in the plane of the line of sight ϵ_z does not affect the gravitational lensing calculations because of the thin lens approximation, and it will be shown in Section 2.2.1 that it can also be neglected for calculations of the S-Z effect.

3.3 Gas in Clusters

X-ray observations of clusters have been used to trace the gas distribution, and through some assumptions this leads to the mass distribution in the cluster. Here, however, the gravitational lensing of the cluster traces its mass much more intimately, as

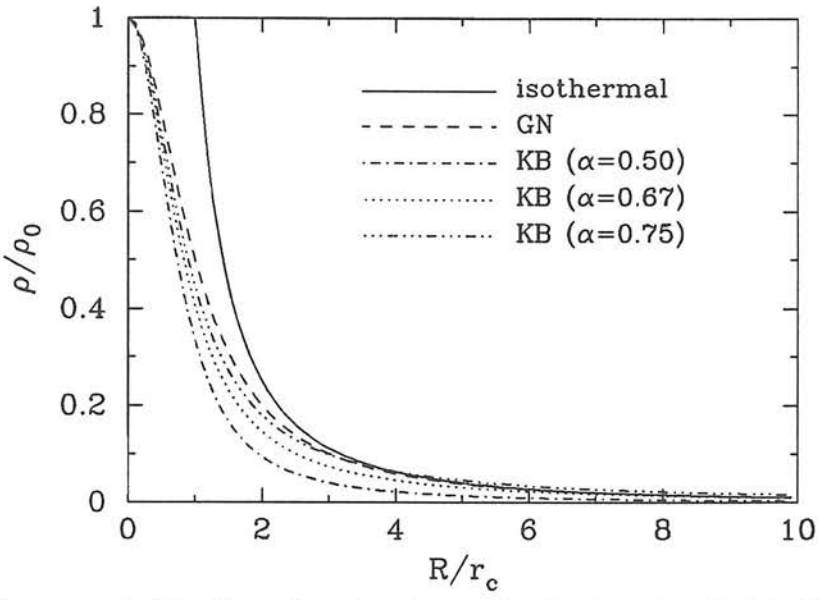

Figure 3.4: *The three dimensional mass distributions described in the main text are plotted here along with the theoretically ideal case of the spherically symmetric, isothermal mass distribution. The 3d distribution of KB is similar to that of GN for $\alpha = 0.75$, which is somewhat different than their 2d counterparts. All of the models are fairly good approximations to the isothermal distribution at large distances.*

shown by GN who reproduced the optical luminous arcs in A370. In order to compare the gravitational lensing of submillimetre background sources, to the S-Z effect, the same recipe for mass–gas relationship is followed, but with the goal of deriving the gas distribution from the mass distribution.

The usual assumption has the gas (or electron number density n_e) tracing the total mass distribution ρ according to a simple power law [Lea 1975, Gull & Northover 1975, Cavaliere & Fusco-Femiano 1976, Sarazin & Bahcall 1977, for a review see Sarazin 1988],

$$n_e/n_0 = (\rho/\rho_0)^{\beta}. \tag{3.16}$$

For the case of an isothermal gas cloud in hydrostatic equilibrium, the index β is well defined as

$$\beta \equiv \mu M_H \sigma_v^2 / kT_e \tag{3.17}$$

where μ is the mean atomic mass, M_H is the proton mass, σ_v is the line of sight velocity dispersion of the galaxies in the cluster, and T_e is the electron brightness temperature.

X-ray brightness morphology of clusters is well fitted by a spherical gas distribution similar to the mass distribution used by GN (Eq. 3.15b),

$$\frac{n_e}{n_0} = \left(1 + \frac{r^2}{r_c^2}\right)^{-3\beta_{JF}+1/2} \quad \text{[Jones \& Forman 1984]}, \tag{3.18}$$

and the best values for β_{JF} based on a large number of clusters was in the range $0.5 < \beta_{JF} < 0.8$. An experiment based on Eq. 3.17 has been performed by Mushotzky [1984] and data amassed from velocity dispersions of clusters with well determined X-ray brightness, gives a range of $0.5 < \beta_{JF} < 5.0$, with the average value of $\beta_{JF} = 1.2$. The index of Jones & Forman can be translated to the notation used here based on the model of GN: $\beta = 3\beta_{JF} - 0.5$. Therefore the Jones & Forman data implies a range of β from 1 to ~2. The Mushotzky result is equivalent to $\beta = 3.1$. For the ellipsoidal generalization of the spherical mass distribution given in Eq. 3.15a, the Thompson optical depth can be calculated to be the following:

$$\tau_T = \sigma_T n_0 r_c \left[1 + \frac{2\alpha}{3}\frac{r_\epsilon^2}{r_c^2}\right]^{\beta} \left[1 + \frac{r_\epsilon^2}{r_c^2}\right]^{\beta(\alpha-5/2)+1/2} \mathcal{I}(\alpha, \beta, r_\epsilon), \tag{3.19a}$$

where

$$\mathcal{I}(\alpha, \beta, r_\epsilon) = \int_{-\infty}^{+\infty} (1+bu^2)^{\beta} (1+u^2)^{\beta(\alpha-5/2)}\, du, \tag{3.19b}$$

with

$$r_\epsilon^2 = \frac{\epsilon_z(\epsilon_x x^2 + \epsilon_y y^2)}{(\epsilon_x \theta_x^2 + \epsilon_y \theta_y^2 + \epsilon_z)}, \tag{3.19c}$$

and

$$b = \frac{2\alpha}{3}\left[1 + \frac{r_\epsilon^2}{r_c^2}\right]\left[1 + \frac{2\alpha}{3}\frac{r_\epsilon^2}{r_c^2}\right]^{-1}. \tag{3.19d}$$

Ellipticity in the plane of the line of sight appears only in the expression for r_ϵ. However, unless the cluster is inordinately elongated along the line of sight, then terms of order θ^2 can be neglected in comparison to terms of order unity. Any dependence on ϵ_z then drops out, and, using the same eccentricity convention as for the two dimensional mass distributions, Eq. 3.19c becomes $r_\epsilon^2 = (1-\epsilon)x^2 + (1+\epsilon)y^2$.

At this point, it is useful to test the cluster mass model against an observational constraint. In particular, the claimed detection of the S-Z effect by Birkinshaw *et al.*

[1981] will be used as the comparison. In that work, the microwave dimunition was looked for towards the cluster 0016+16 and the result at 10.7 GHz in a 3.'3 beam was $-1.36\,\mathrm{mK} \pm 0.28\,\mathrm{mK}$. This implies a $\Delta F/F$ at 10.7 GHz of -4.5×10^{-4}, and the Comptonization parameter is therefore $y = 2.1\times10^{-4}$. Figure 3.15 shows the dependence of the Comptonization parameter y on the gas distribution index β. The parameters used to simulate the cluster 0016+16 are primarily based on available observational data so that β becomes the only free parameter to make the model consistent with the Birkinshaw *et al.* result. The cluster is considered to be isothermal with electron brightness temperature $T_e = 10^8\,\mathrm{K}$ being consistent with the lower limit obtained by White *et al.* [1981] of $T_e > 7.0\times10^7$. The redshift and optical core radius are taken from Koo [1981]: $z = 0.541$ and $r_c = 45''$. The central electron density is assumed to be $n_0 = 1.0\times10^{-3}\,\mathrm{cm}^{-3}$ (see also Section 3.6.3). The measurement by Birkinshaw *et al.* is consistent with a gas index of $\beta = 1.2$. Note that for $\beta \gtrsim 1.5$ the change in the Comptonization parameter is no longer significant.

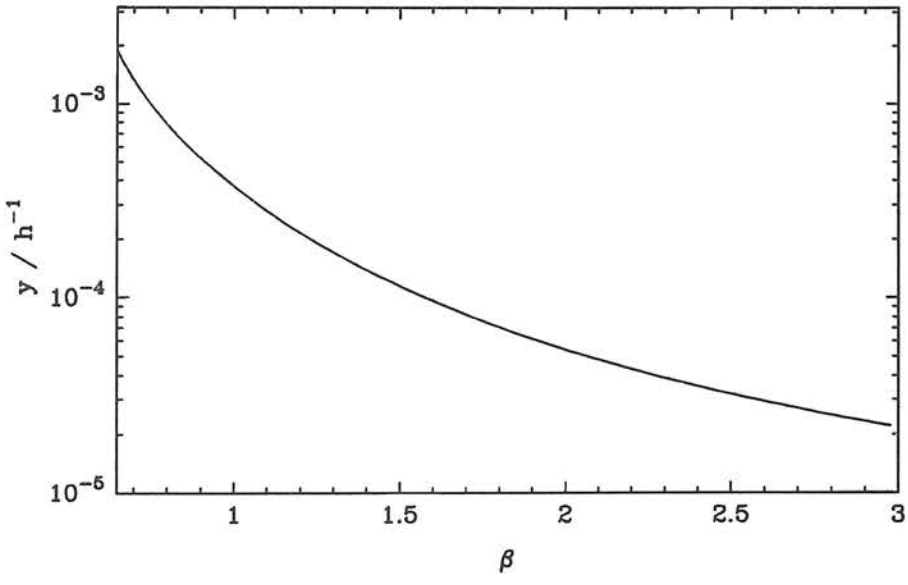

Figure 3.5: *The Comptonization parameter as it would be measured by a 3.'3 beam when looking towards the cluster* 0016+16 *is plotted against the gas index* β. *The measurement of Birkinshaw* et al. *is consistent with* $\beta = 1.2$ *in the model used here.*

3.4 The Submillimetre Background

The basic argument of dusty primeval galaxies presented in the introduction to this Part motivates the development of a simple toy model in which foreground submillimetre radiation is added to the CBR in the form of a grey body where the discrete components of the primordial dust emission are more or less homogeneously distributed, and comprise a fraction ξ of the entire sky. The broad spectrum of a blackbody allows a single temperature to be used for modelling the spectral shape of the primordial dust. All the primeval galaxies are expected to emit at temperatures of the order of 50 K, and since the population would be constrained to an epoch from redshifts of 2 to 10 or so, there would not be a very heterogenous spectral shape resulting. The following greybody model is sufficient.

$$F = F_{\rm B} + \xi F_{\rm d}, \tag{3.20}$$

where $F_{\rm d}$ is a Planck function at temperature $T_{\rm d}$, and $F_{\rm B}$ is the CBR at temperature $T_{\rm B} = 2.735\,{\rm K}$. *viz.*

$$F_{\rm d,B} = \frac{2h\nu^3}{c^2}(e^{x_{\rm d,B}} - 1)^{-1} \quad \text{with} \quad x_{\rm d,B} = h\nu/kT_{\rm d,B}. \tag{3.21}$$

This can be raised to a DC level so that anisotropy due to dust is measured relative to the CBR:

$$\Delta F = \xi\,(1 + \delta_r)\,F_{\rm d} \tag{3.22}$$

where δ_r is a normalized anisotropy in the range $\delta_r \geq -1$ with $\langle \delta_r \rangle = 0$. The anisotropy on various angular scales described by Bond *et al.* is seen as the "hot spots" which are formed by lines of sight intersecting the primeval galaxies ($\delta_r > -1$), and the "cold spots" which see right through to the CBR ($\delta_r = -1$). Figure 3.6 shows the allowable values for the grey body fraction ξ, and the redshifted temperature $T_{\rm d}$ given the constraints set by COBE early last year. Figure 3.7 shows the CBR added to the dust component with $\xi = 0.001$ and $T_{\rm d}$=5 K.

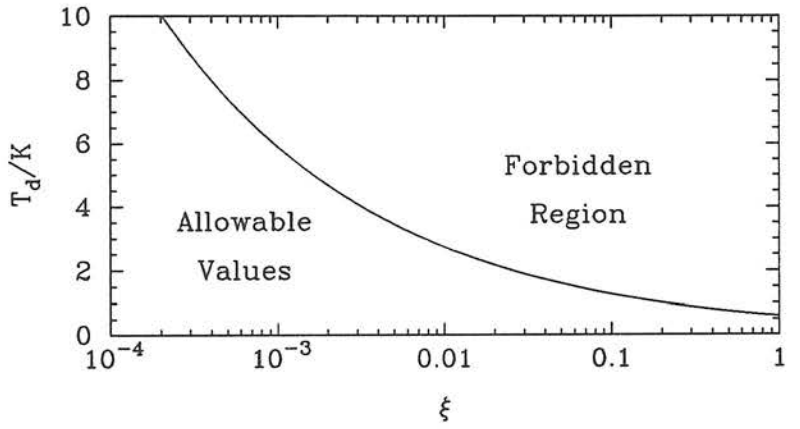

Figure 3.6: *COBE's sensitive measurement of the CBR places fairly rigid constraints on the allowable redshifted dust temperature T_d and the sky filling factor ξ in the grey body approximation of the primeval dust contribution (Eq. 3.22). All values to the left of the curve are permitted.*

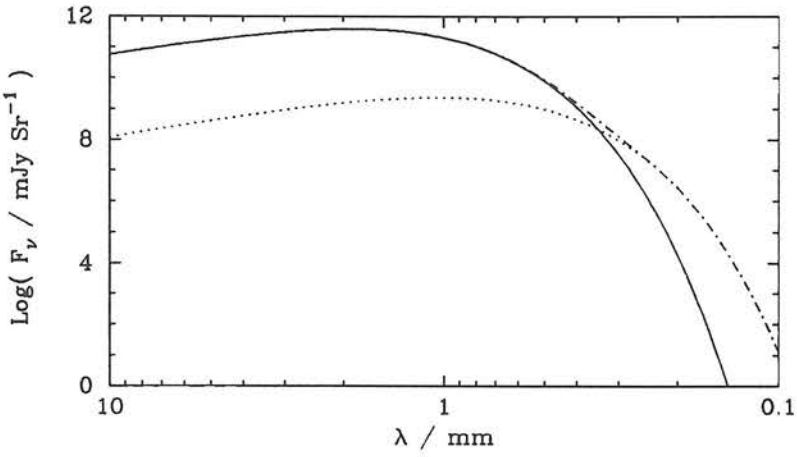

Figure 3.7: *The* 2.735 K *cosmic blackbody which peaks at* $\lambda = 1.865\,\mathrm{mm}$ *as measured by COBE is plotted along with a grey body of* 5 K *with a filling factor of 0.001 (dotted line). When the two are added together, the resulting 'excess' is well within the 1% peak flux limitation on the blackbody which is the COBE constraint to date. COBE measured the CBR in the range* $10\,\mathrm{mm} > \lambda > 0.5\,\mathrm{mm}$.

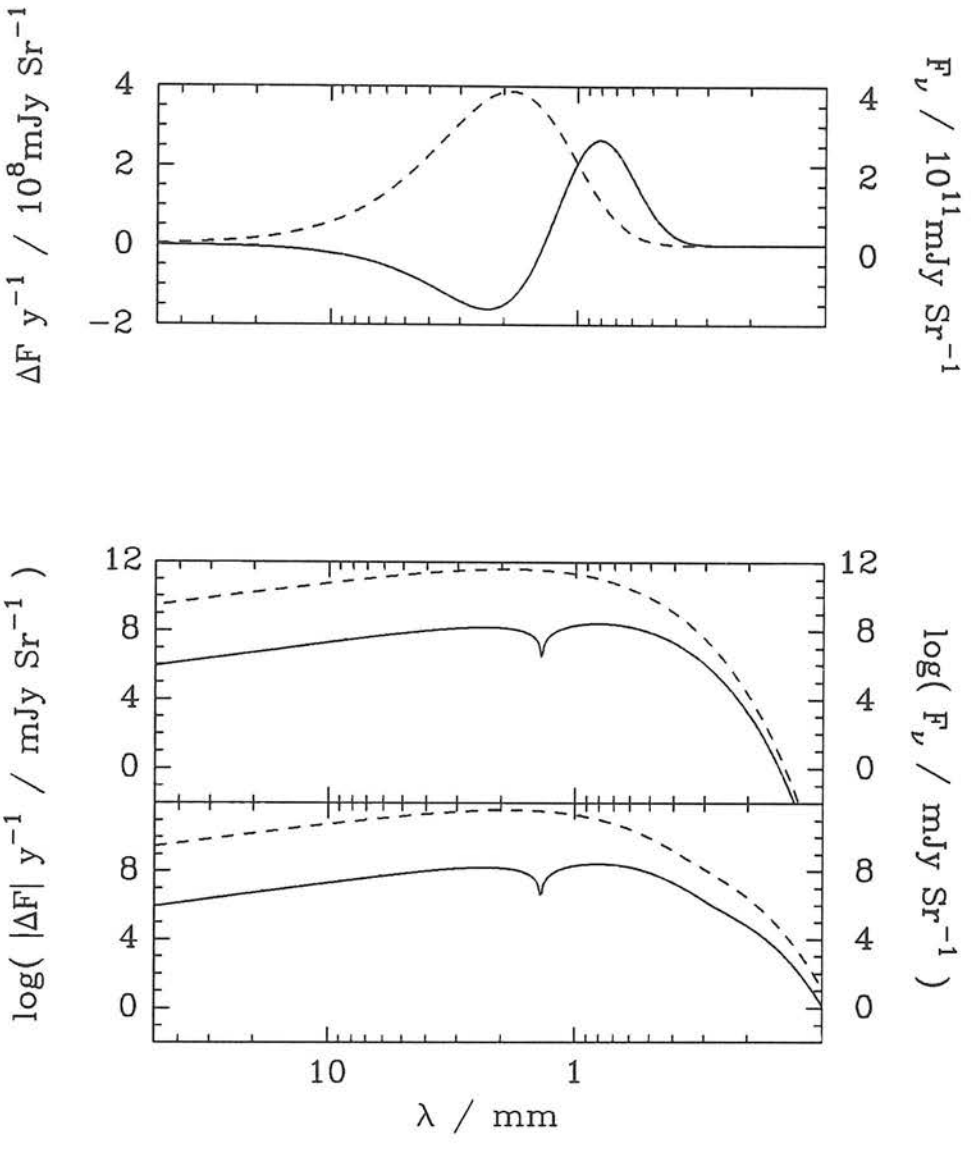

Figure 3.8: a) *The distinctive spectrum of the Sunyaev-Zel'dovich effect is plotted here along with the CBR (dashed line, right-hand scale). It has a maximum distortion to the CBR at a wavelength of 800 μm. For A370, $y \simeq 10^{-2}$ through the centre of the cluster, so the percent flux distortion $\Delta F_\nu / F_\nu \simeq 0.8\%$ is less than the postulated primordial dust excesss $\Delta F_\nu / F_\nu \simeq 2\%$.* b) *The magnitude of the S-Z effect is plotted on a log scale to show in* c) *the effect of the primordial dust background on the S-Z spectrum at short wavelengths.*

3.5 Gaussian Models for Background Fluctuations

The next necessary step in these simulations is to produce a map of the submillimetre sky, given that the maximum amplitude of fluctuations is known. This can be done meticulously by considering the many aspects of a cosmological model, such as the Einstein field equations for the various particles before and after recombination, and choosing a candidate for the cold dark matter particle, if any [see *e.g.* Bond 1988]. Additionally, there are parameters including the bias in galaxy formation, and the density parameter Ω (*i.e.* whether it is an open, flat, or critical universe), as well as the Hubble time H_0^{-1}. However, without delving too deeply into these things, it is still possible to obtain a reasonable realization of angular anisotropies in the submillimetre sky.

The goal here is to produce simply a field of random fluctuations. Principally, the desired aspects of the field are the predominant length scale of the fluctuations, and its peakiness. Since little is known about the distribution of the dusty primeval galaxies, the use of a Gaussian power spectrum is as justifiable as any means which has the required parameters. The starting point is then a random phase, Gaussian power spectrum in $k-$space (the frequency of the fluctuations),

$$|\delta_k|^2 = k^{-\gamma} \exp(-k^2/k_0^2). \tag{3.23}$$

The peakiness of the field is controlled by γ, and the length scale is controlled by k_0. The range of these parameters will produce fields that can be compared to more elaborate theories such as Bond *et al.* [1986, 1990]. The above frequency space spectrum (Eq. 3.23) is fourier transformed to get the $r-$space profile (the angular scale):

$$\delta_r = \left(\frac{L}{2\pi}\right)^2 \iint d^2k \; \delta_k \, e^{-i\vec{k}\cdot\vec{r}}, \tag{3.24a}$$

$$\delta_k = \frac{1}{L^2} \iint d^2r \; \delta_r \, e^{i\vec{k}\cdot\vec{r}}. \tag{3.24b}$$

The k_0 is related to the spatial scale of the fluctuations by $k_0 = 2\pi/r_0$, where r_0 is the length scale (*e.g.* $10''$, see Fig. 3.11), and L is the side of the 'box'. In the simulations of Figs. 3.11 and 3.14 a square field of $L = 120''$ on a side was produced by filling a

256×256 element array with magnitudes given by Eq. 3.23, and random phases to create the complex power spectrum in the frequency space. The array is then operated on by a Fast Fourier Transform, and this begets a mishmash of blobs of uncertain morphology as in Figs. 3.11 and 3.14. The random numbers are generated using the NAG Fortran routine G05CAF, and the FFT is performed by C06FUF.

For a given incarnation of the sky, as described above, the mean amplitude of fluctuations on various angular scales can be found by convolving the spectrum with the desired beam size. The spatial spectrum $\delta_{r/q}$ is the smeared out version of the original sky δ_r which is achieved through the Fourier transform,

$$\delta_{r/q} = \mathcal{F}\left\{\delta_k e^{-k^2 q^2/2}\right\}. \tag{3.25}$$

The variance Δ^2 is a measure of the mean amplitude of fluctuations at a given smearing angle q. This is calculated simply by taking the power in the k–space spectrum and then the Fourier transform for the mean space amplitude,

$$\begin{aligned}\Delta^2 &= \left(\frac{L}{2\pi}\right)^2 \int_0^\infty 2\pi k\, dk\ |\delta_k|^2\, e^{-k^2 q^2}, \\ &= \Delta_0^2 \left(1 + k_0^2 q^2\right)^{(\gamma-2)/2}, \end{aligned} \tag{3.26}$$

Δ_0 is a normalizing constant equal to the *rms* of the spectrum (Eq. 3.23). Figure 3.9 plots the variance over a range of smearing angles, for four different power spectrum indices and with length scale $r_0 = 10''$. Setting the power index $\gamma = 1.2$ and the length scale $r_0 = 10''$ compares well to the rigorous calculations of Bond [1988, Fig. 7.2].

The examples of sky fields with fluctuations predominantly on the scale of $10''$ in Fig. 3.10 show the insensitivity of this method to the power spectrum index. The sky fields were each generated using the same random phases in the k – space grid, but with different power spectrum indices. The resulting random fields shown in Fig. 3.10 are essentially the same. Power spectrum indices greater than 2 are not considered since this would imply a greater average anisotropy amplitude for larger beam sizes (see Fig. 3.9, and Eq. 3.26). This would contradict a realistic physical picture. The field with $r_0 = 10''$ and $\gamma = 1.2$ will be used as the source plane for the simulations of gravitational lensing discussed in Section 3.6. (Fig. 3.11 shows this field in a larger format for clarity).

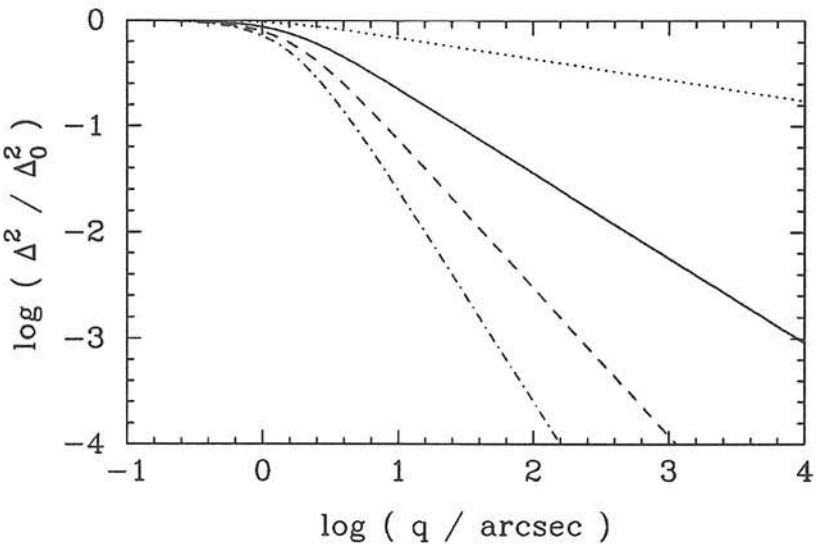

Figure 3.9: *For a length scale $r_0 = 10''$ a random phase Gaussian power spectrum, with power indexes $\gamma = 0, 0.6, 1.2,$ & 1.8 (dash-dot line, dashed line, solid line, and dotted line), the variance Δ^2 (Eq. 3.26) is plotted against a beam smearing width of q. With the parameters $\gamma = 1.2$ and $r_0 = 10''$, there is good comparison to the rigorous calculations of Bond [1988, Fig. 7.2].*

The above work is repeated for the length scale $r_0 = 5''$.

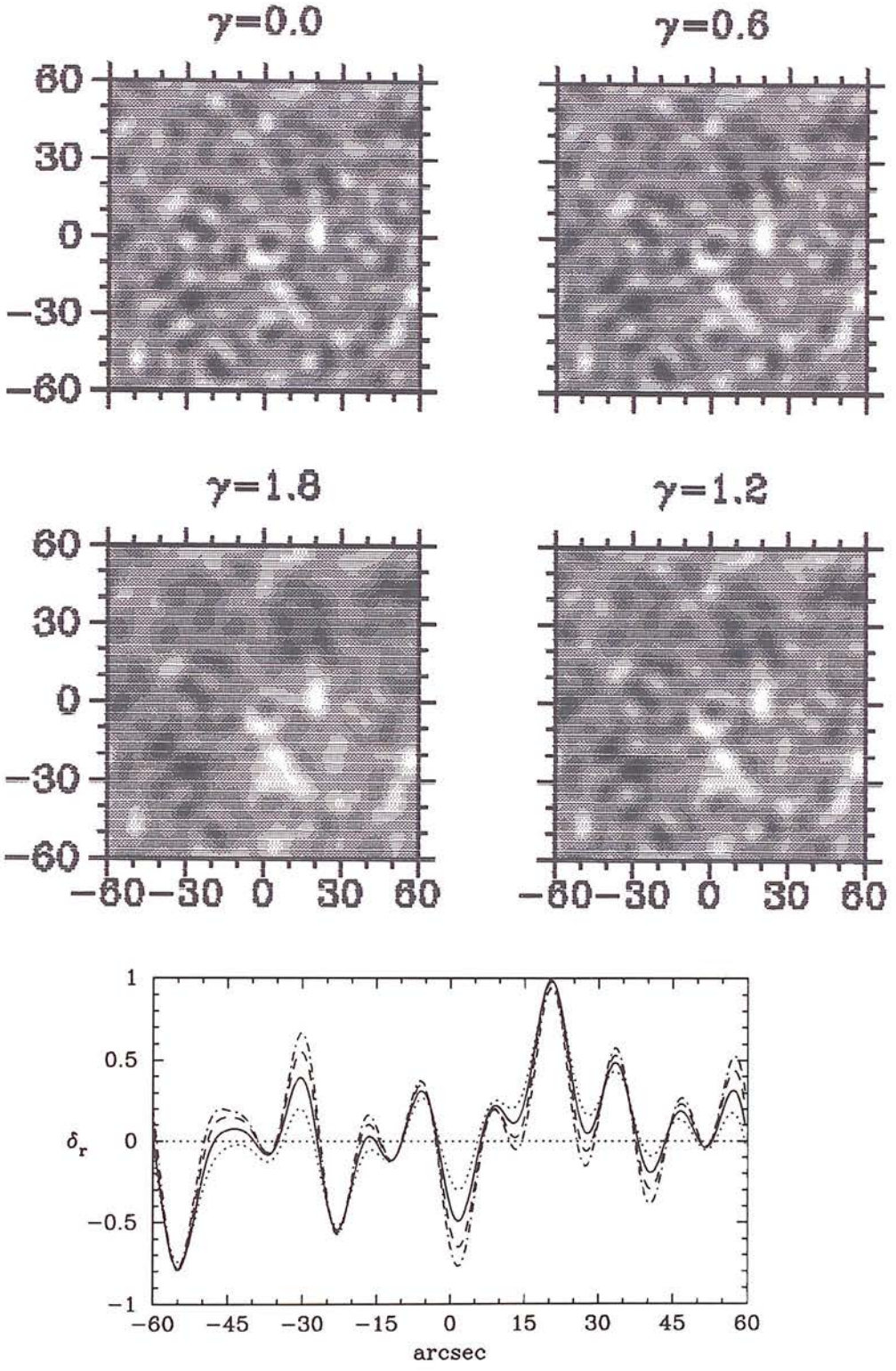

Figure 3.10: *Simulated fluctuations which are predominantly on the scale of* 10″ *are generated by a Gaussian power spectrum. These are four examples of sky fields that can be created with various power spectal indices. Clockwise from the top left they are:* $\gamma = 0.0,\ 0.6,\ 1.2$ *&* 1.8. *The bottom figure shows a cross section through the centre of the grid, parallel to the x-axis. From* $\gamma = 0.0$ *to* 1.8 *as above, the cross sections are the dash-dot line, the dashed line, the solid line, and the dotted line. A "decrement" of* $\delta_r = -1$ *corresponds to the pure CBR.*

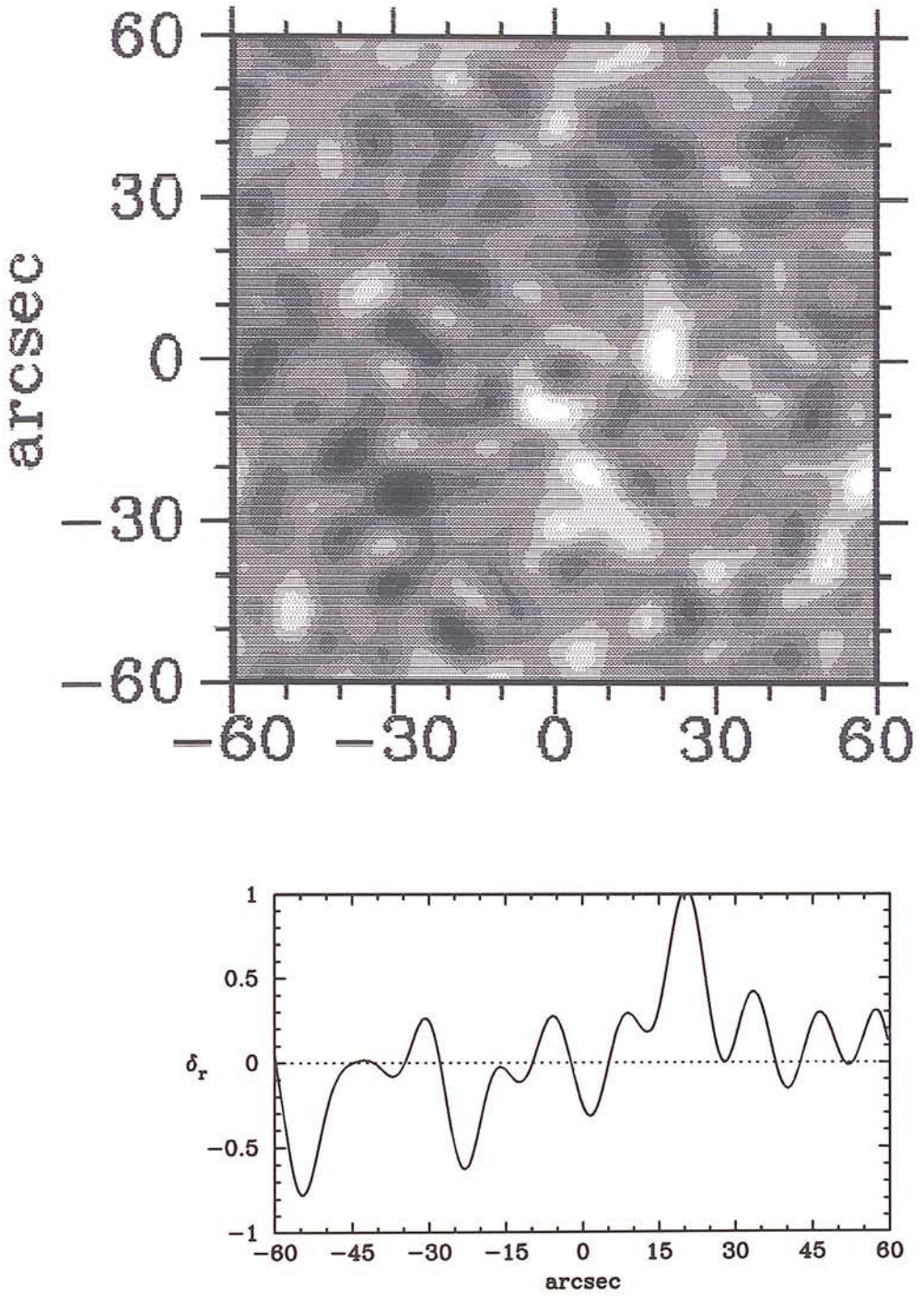

Figure 3.11: *This sky field with $\gamma = 1.2$ and $r_0 = 10''$ will be used as the source plane for the simulations in Section ~~2.4.~~ 3.6*

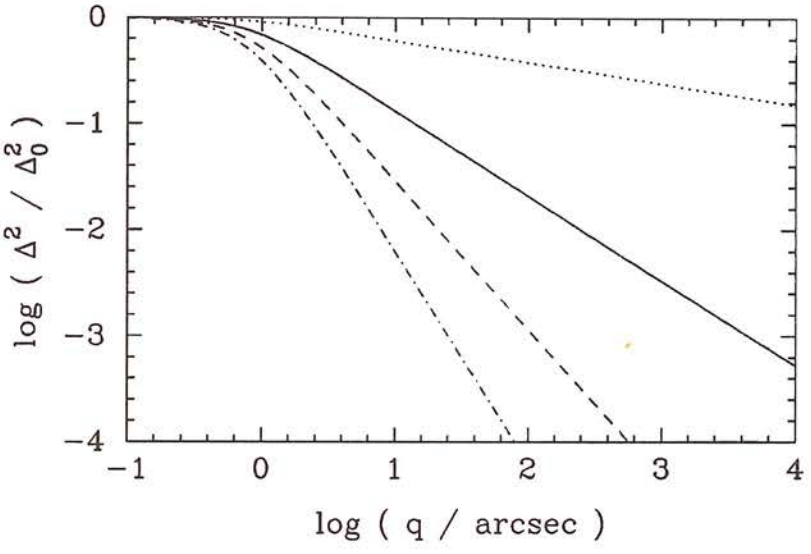

Figure 3.12: *For a length scale $r_0 = 5''$ a random phase Gaussian power spectrum, with power indexes $\gamma = 0, 0.6, 1.2,$ & 1.8 (dash-dot line, dashed line, solid line, and dotted line), the variance Δ^2 (Eq. 3.26) is plotted against a beam smearing width of q.*

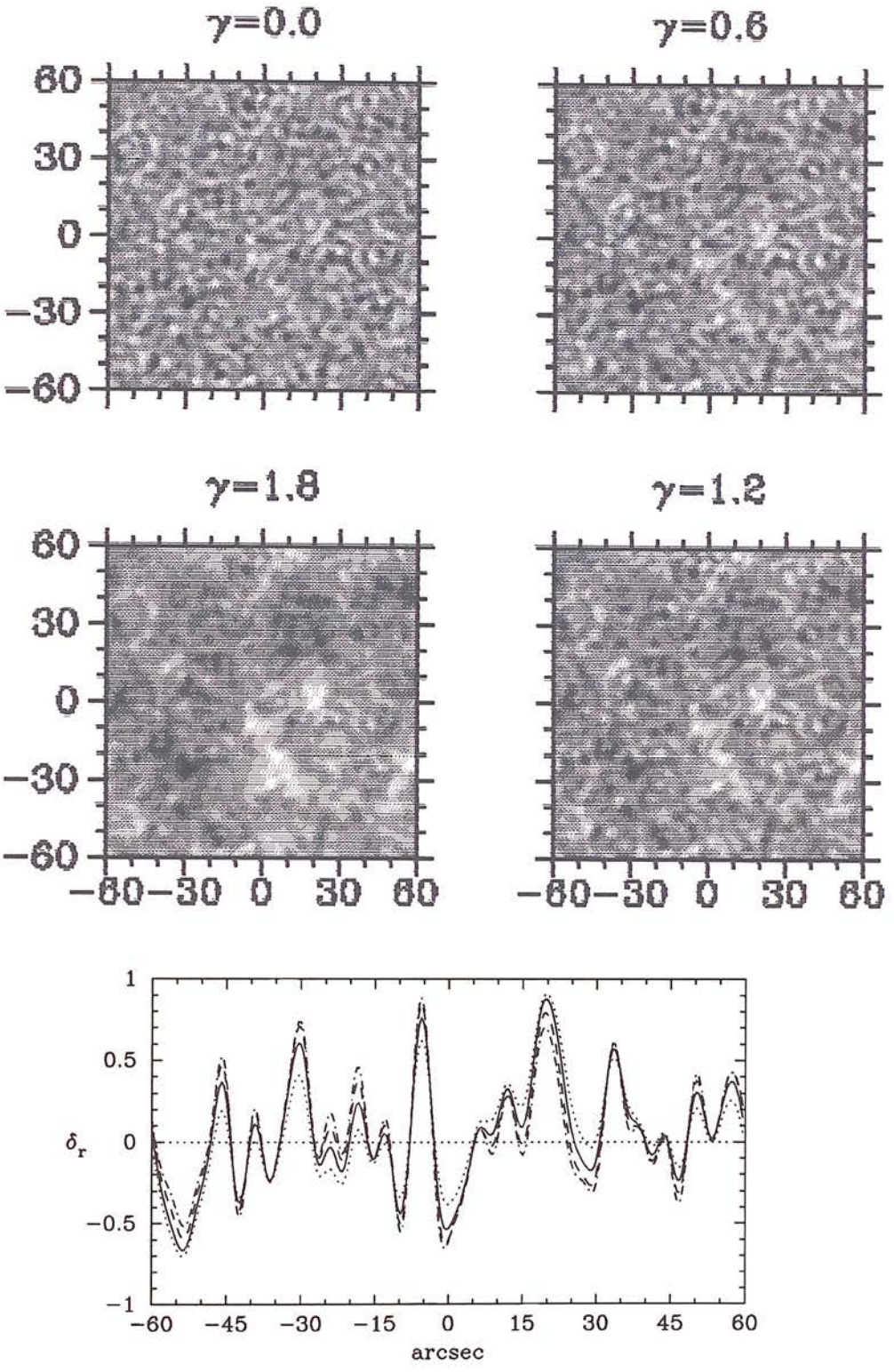

Figure 3.13: *Simulated fluctuations which are predominantly on the scale of 5″ are generated by a Gaussian power spectrum. These are four examples of sky fields that can be created with various power spectral indices. Clockwise from the top left they are: $\gamma = 0.0$, 0.6, 1.2 & 1.8. The bottom figure shows a cross section through the centre of the grid, parallel to the x-axis. From $\gamma = 0.0$ to 1.8 as above, the cross sections are the dash-dot line, the dashed line, the solid line, and the dotted line. A "decrement" of $\delta_r = -1$ corresponds to the pure CBR.*

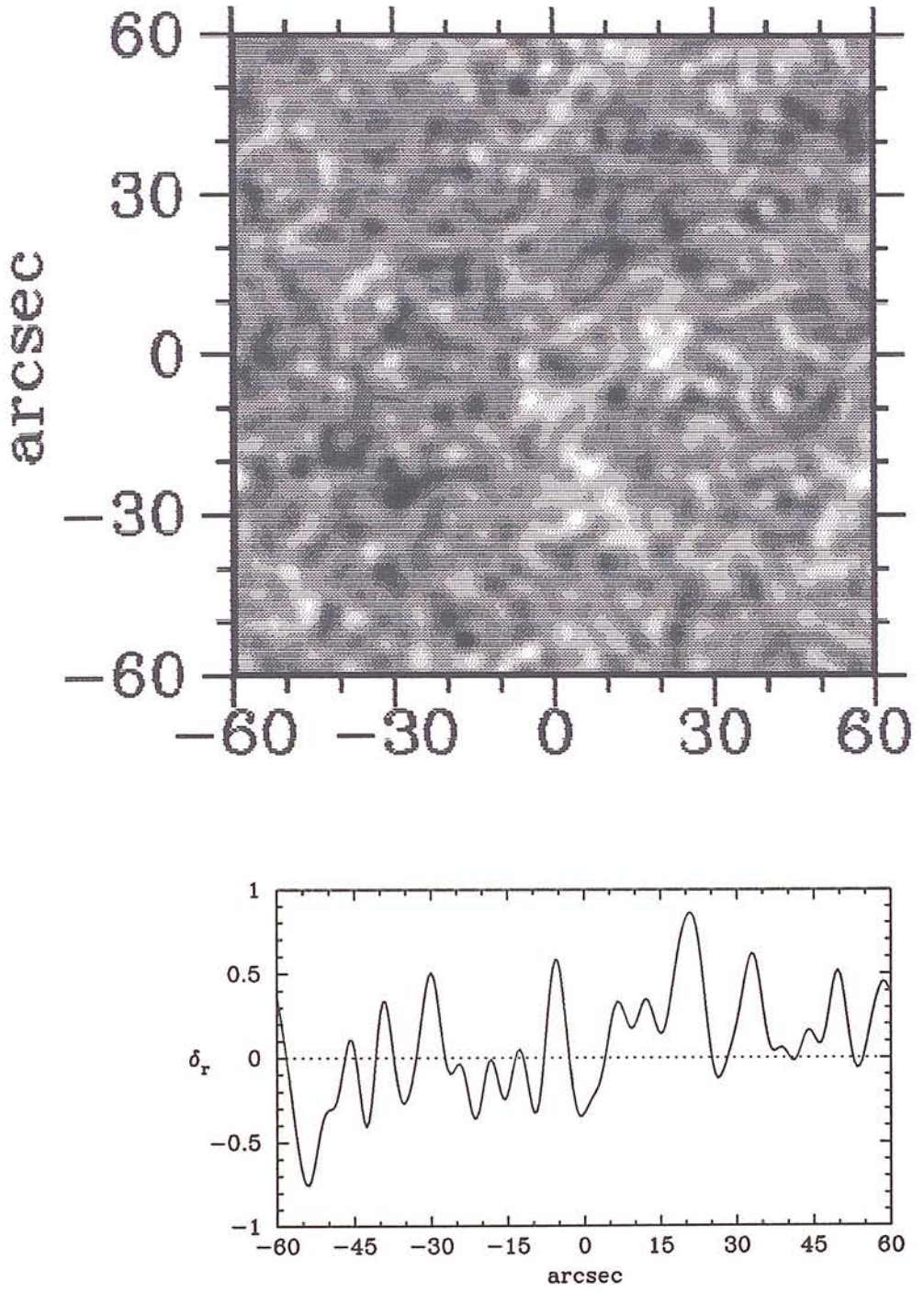

Figure 3.14: *This sky field with $\gamma = 1.2$ and $r_0 = 5''$ will be used as the source plane for the simulations in Section ~~2.4.~~ 3.6*

3.6 Simulations of Observations through Clusters

The calculations for the following simulations are all done within the framework of a critical ($\Omega = 1$) universe. A specific universe is chosen for the sake of presentation, however the results do not change qualitatively for various values of Ω. Finally, the population of dusty primeval galaxies are placed at a redshift of $z = 10$.

3.6.1 Case Study: Abell 370

Figure 3.16 is a picture of the observed submillimetre sky (Fig. 3.11) when viewed through the cluster Abell 370 and Fig. 3.17 is that of the sky in Fig. 3.14 with fluctuations primarily at the 5″ scale. This cluster was chosen to have an ellipsoidal mass distribution $\epsilon = -0.6$ which is based on GN's best model, and the line of sight velocity dispersion is $\sigma_0 = 1367\,\mathrm{km\,s^{-1}}$ [Henry & Lavery 1987]. This is a soft model with $\alpha = 0.6$ and the core radius of 10″ is also that used by GN.

For calculations of the S-Z effect, the electron brightness and number density are required. These are taken to be $T_e = 10^8\,\mathrm{K}$ and $n_0 = 1.0\times10^{-3}\,\mathrm{cm^{-3}}$.

The lensing contributions from individual galaxies in A370 have been ignored for the present so Fig. 3.16 shows the global lensing effect. Galaxies in the cluster will add or subtract curvature from the image only when the source–galaxy impact parameter is fairly small, *i.e.* within a small radius of the cluster galaxy. The lensing by individual cluster members as well as by the cluster as a whole are essential ingredients for a reproduction of the morphology of the observed luminous arcs. However, for experiments with telescope beams of 10″, lensing by galaxies will not be resolved in A370.

The image in Fig. 3.16 has not been convolved with a telescope beam.

There are features which appear in these simulations regardless of the given source plane. Where hot or cold spots lie near a caustic on the source plane, a highly elongated arc appears in the image plane. Caustics are points on the source plane for which the Jacobian of the mapping is nil. This is Eq. 3.10, the deprojection equation. Critical lines indicate the corresponding points on the image plane [Grossman & Narayan 1988]. A point source on a caustic will map onto infinitely many points in the image plane forming an elongated arc or ring on or across a critical line. In particular, a source

directly behind a circularly symmetric lens will appear as an Einstein ring. Figure 3.18 shows the caustic and critical lines for A370.

In repeated simulations, an extreme feature in the source plane (either a hot or a cold spot) is always close enough to a caustic to generate an image of which Figs. 3.16 and 3.17 are typical. Near the critical line, a long arc is produced. Usually apparent within the critical lines is an extended blob with a characteristic size about twice that of the original source. This is how a 10″ beam telescope can probe 5″ scale fluctuations. It is in this region that a 10″ beam experiment would have the most dramatic results. Figures 3.19 and 3.20 are plots of the integrated flux in the "best" 17.7″ FWHM beam, and in the central 60″. The CBR flux has been subtracted to give a zero dc-level from which the S-Z effect and the dusty PG effect are compared. As can be seen in these examples, the two effects are of the same order of magnitude, although the S-Z generally dominates in a wide beam experiment such as shown in Figs. 3.19b and 3.20b.

The fluxes calculated up to this point have been for the particular cases associated with the sky fields of Figs. 3.11 and 3.14, but these do not properly indicate the expected fluxes from the gravitational lens experiment. It is possible for sources to position themselves favourably such that the received flux after gravitational lensing is maximized. The existence of the optical luminous arcs is evidence that such chance alignments occur. However, in order to quantify the likelihood of a significant submillimetre flux, many simulations are carried out and the results are plotted in a histogram (Fig. 3.21a). The flux in the central 60″ FWHM beam is chosen as the indicator. Since the sky fields are generated with a Gaussian power spectrum, the Gaussian histogram of Fig. 3.21a is expected. Using the *rms* ($e^{-\frac{1}{2}}$) point, one concludes that in over 60% of these simulations, the gravitational lens effect interferes significantly with the S-Z effect, especially as they both peak at $\sim 850\,\mu$m; the natural wavelength at which to perform either experiment.

The expected flux amplification by gravitational lensing can be quantified in a similar way, using the $e^{-\frac{1}{2}}$ flux points of the image and source planes in a 60″ FWHM beam. For the case of A370, the ratio of expected fluxes with and without gravitational lensing is $\sim$2.5. Smaller beam experiments exploit the cluster's lensing effect to a much greater extent. In the case presented here, the flux in a 17.7″ beam on the position

chosen for Fig. ~~3.19~~ 3.18 is ten times greater with gravitational lensing, than without.

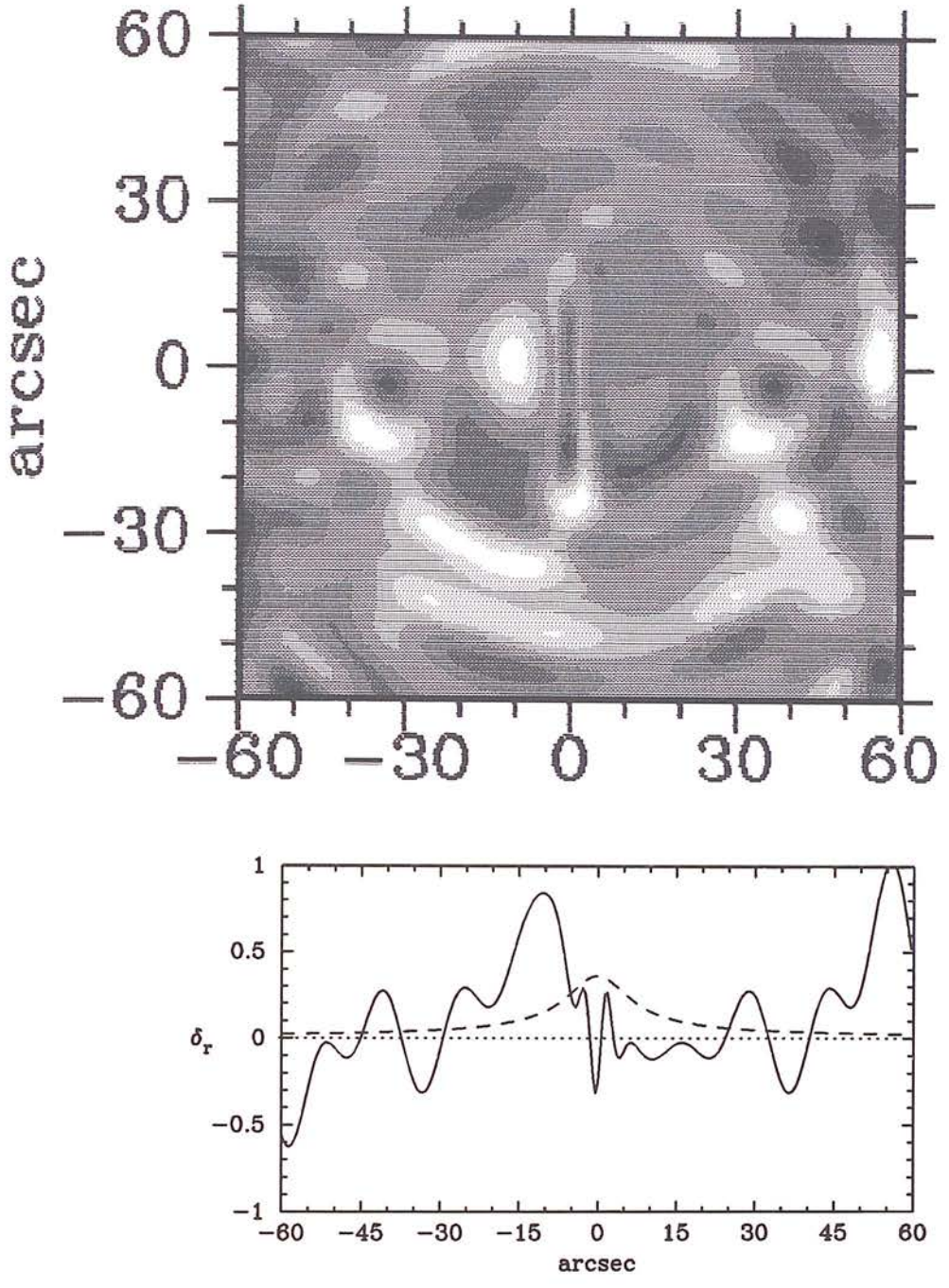

Figure 3.15: a) *Gravitational lensing by A370 of the background source plane of Fig. 3.11 shows some typically distinct features. These include an extended vertical line at the centre of the field, and elongated arcs within an elliptical annulus at ~30″ from the centre.* b) *The figure below shows a cross-section through the image plane at the centre and parallel to the x-axis. The dashed line is the spatial profile of the S-Z effect scaled here to correspond to the effect at* $\lambda = 855\,\mu$m

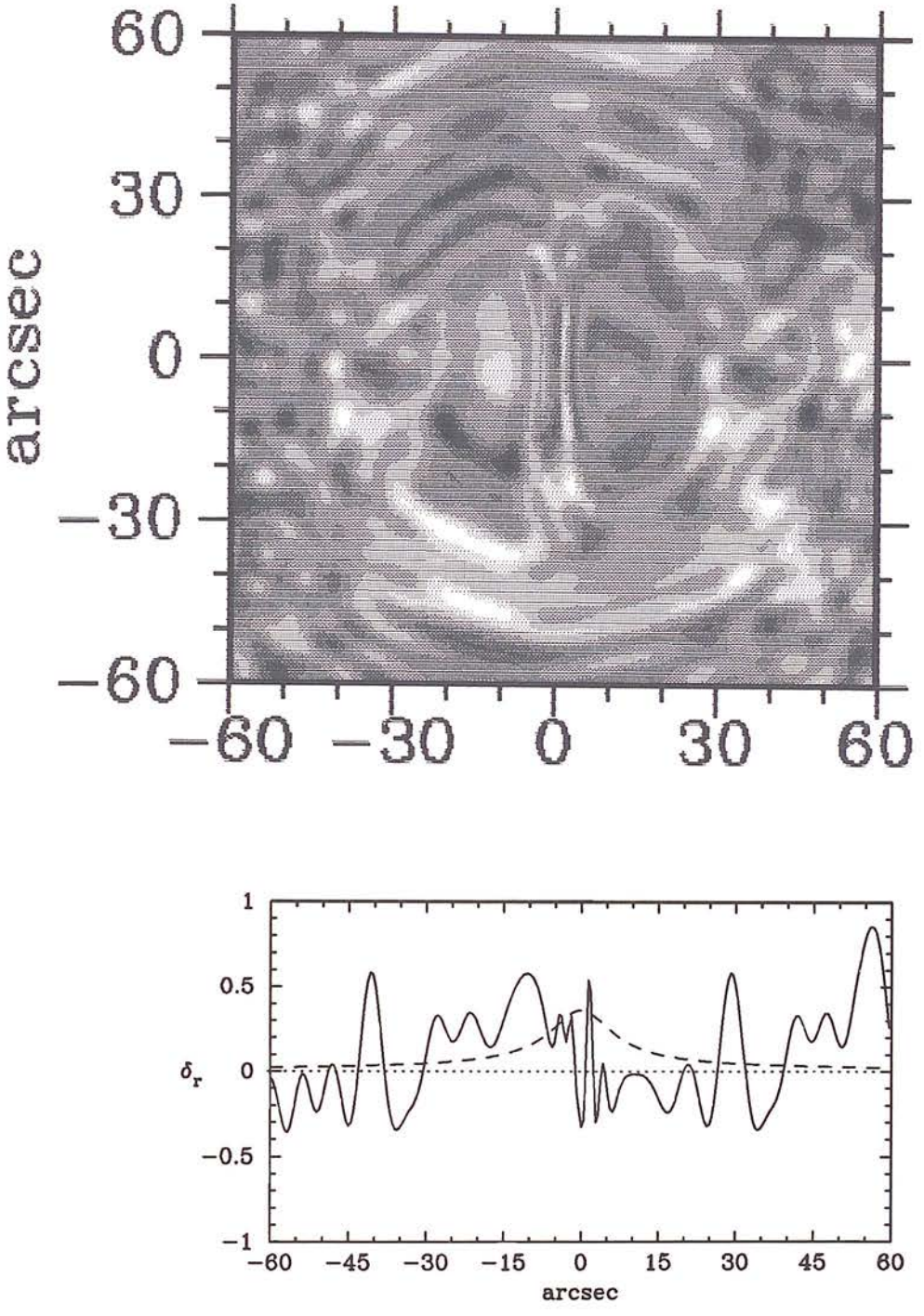

Figure 3.16: a) *Gravitational lensing by A370 of the background source plane of Fig. 3.14* and b) *the cross section as in Fig.* ~~3.16~~ 3.15

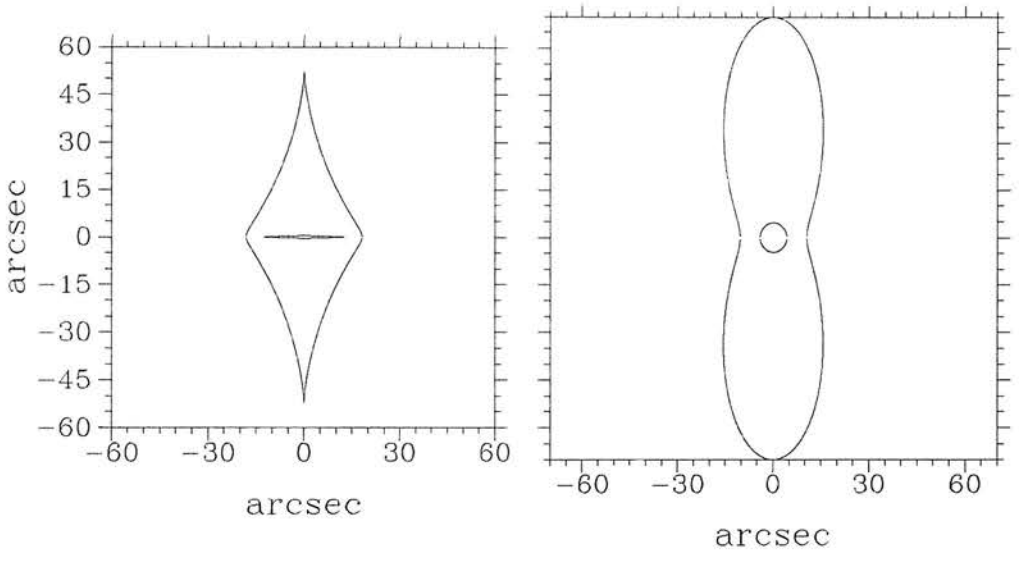

Figure 3.17: *When a source plane is placed at a redshift $z = 10$, the caustic lines for the cluster Abell 370 are those shown in the left panel. The critical lines are shown in the right panel.*

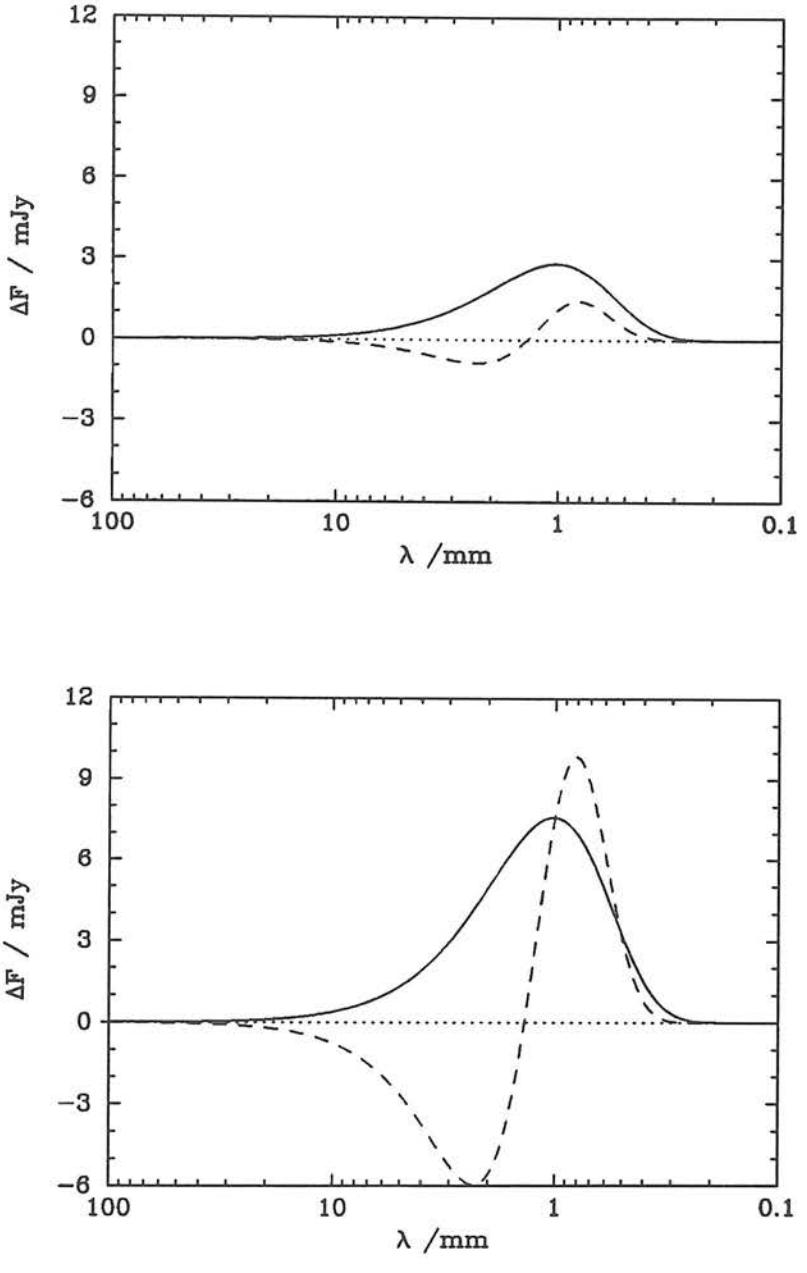

Figure 3.18: a) *The best flux in a 17.7″ FWHM beam in the field of Fig. 3.16 as a result of gravitational lensing of the submillimetre background is compared to the S-Z effect in the same beam.* b) *The lower panel shows the fluxes in the central 60″ FWHM beam of the same field.*

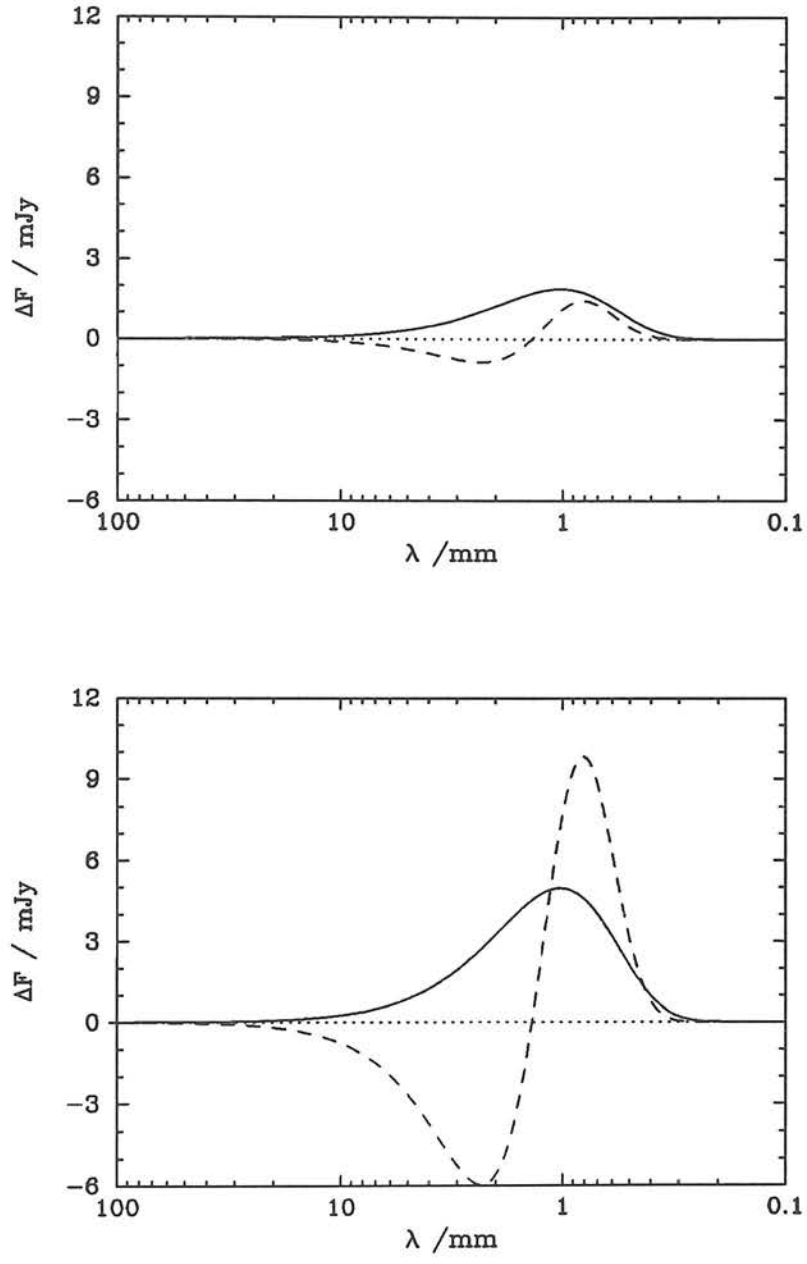

Figure 3.19: *As in Fig. ~~3.19~~ 3.18, the fluxes are shown for the image of the 5″ scale sky fluctuations.*

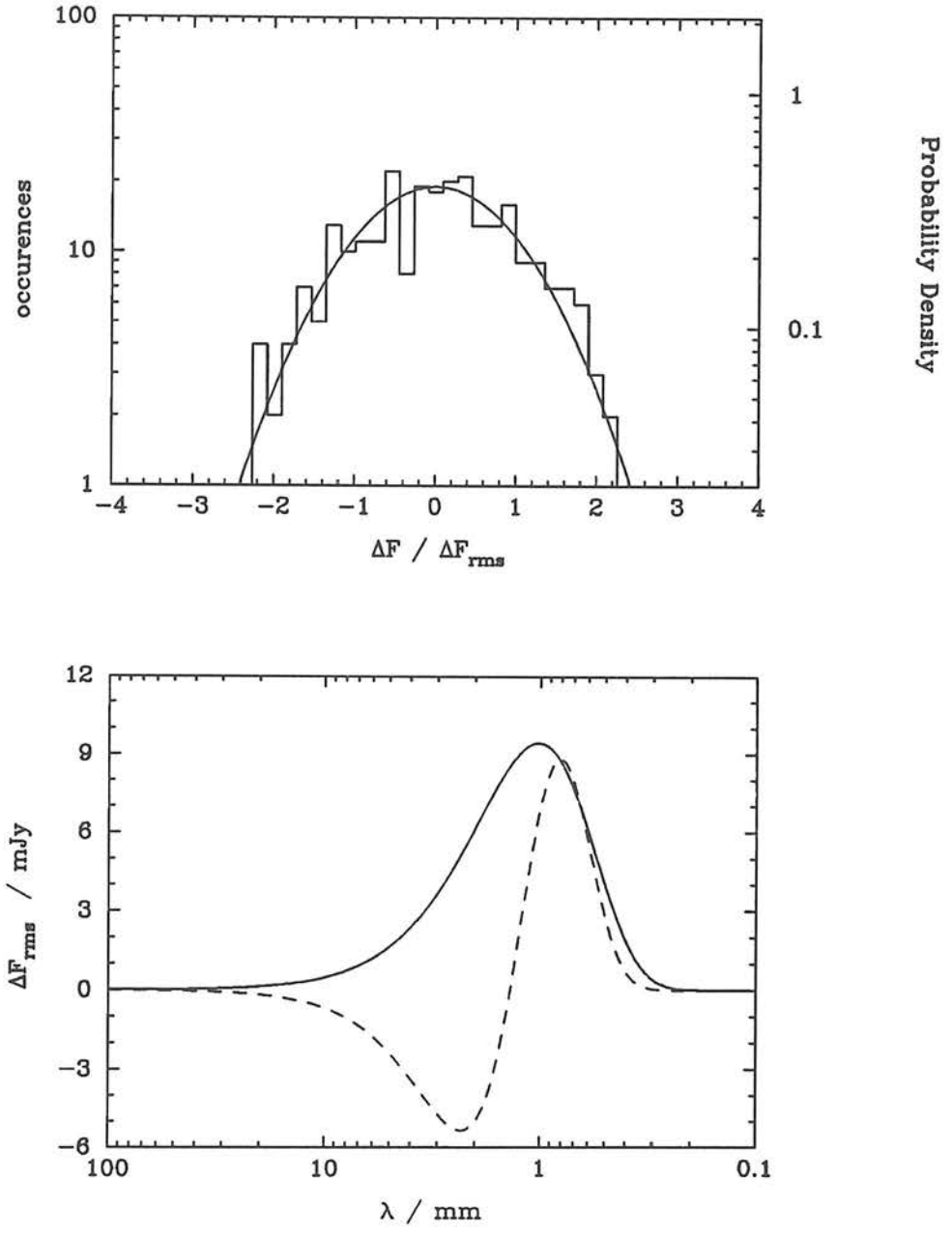

Figure 3.20: *Over 500 sky fields with $\gamma = 1.2$ and $r_0 = 10''$ were generated, and these were each used as the source plane. After gravitational lensing by A370, the flux in a beam of 60″ FWHM centred on the cluster was calculated.* **a)** *This is a histogram of the central fluxes from the repeated simulations.* **b)** *The wavelength dependence of the $e^{-\frac{1}{2}}$ point of the above histogram.*

3.6.2 Case Study: Cl 2244–02

Another cluster with notoriety as a gravitational lens is Cl2244−02 (herefter Cl2244). The main luminous arc found here is thought to be the image of a galaxy at redshift $z = 2.238$ [Soucail *et al.* 1989]. The cluster's redshift is $z = 0.328$. Once again a soft model ($\alpha = 0.6$) has been used, which indicates that the cluster is approximately isothermal at large distances from the centre. For the line of sight velocity dispersion, the value $\sigma_0 = 1000\,\mathrm{km\,s^{-1}}$ was used, and the cluster mass distribution is considered to be circular which is consistent with the shape of the giant arc. The core radius is $10''$.

The electron brightness temperature and number density are taken to be $T_e = 10^8$ K and $n_0 = 1.0\times10^{-3}\,\mathrm{cm^{-3}}$.

Figure 3.21 is a picture of the observed submillimetre sky of Fig. 3.11 when viewed through the cluster Cl2244, and Fig. 3.22 is that of the sky in Fig. 3.14 with fluctuations predominantly at the $5''$ scale. The caustic and critical lines for this cluster are shown in Fig. 3.23. The comparison of S-Z and lensing fluxes are displayed in Figs. 3.24 and 3.25. Figure 3.26 is the histogram of fluxes from repeated simulations for sky fields of $r_0 = 10''$. Cl2244 provides a $\sim 2\times$ amplification in the $60''$ beam experiment, and in the simulation presented here, the best flux in a $17.7''$ beam due to the submillimetre background is $\sim 3\times$ what it would be without gravitational lensing by Cl2244.

The simulations in this section can be used to support the analysis of the data presented in Chapter 3. The submillimetre observation of Cl2244 was done with a beam of FWHM $17.7''$, and it was pointed towards a position $\sim 11''$ from the cluster centre. In repeated simulations of the lensing effect on various background planes, the flux at a position $11''$ from the centre of Cl2244 was calculated. The *rms* (or $e^{-\frac{1}{2}}$ point for a Gaussian distribution) gives the variance for this smoothing angle ($q = 7.5''$ for FWHM $= 17.7''$):

$$\frac{\Delta^2}{\Delta_0^2} = 0.8.$$

Comparing this to Fig. 3.9, the conclusion results that this is equivalent to probing the sky with a beam of FWHM $\simeq 3''$ ($q \simeq 1.3''$). Alternatively, one can say that the flux is amplified by the amount $0.8/0.3 \simeq 2.5$ times.

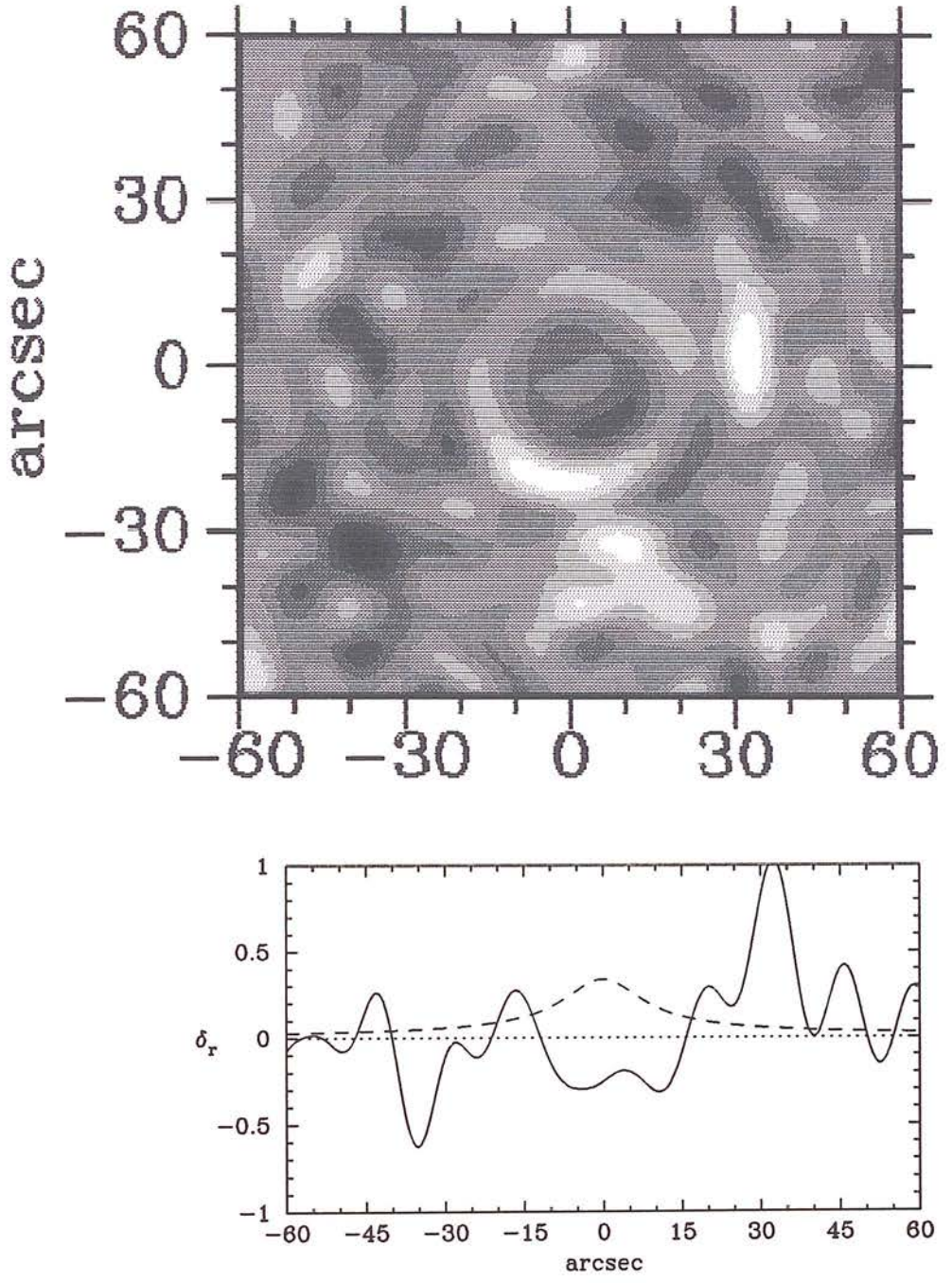

Figure 3.21: a) *Gravitational lensing by Cl2244 of the background source plane of Fig. 3.11 has a somewhat less dramatic effect than that of A370. However, the smearing of the source into generally larger structures is still evident.* b) *The figure below shows a cross-section through the image plane at the centre and parallel to the x-axis. The dashed line is the spatial profile of the S-Z effect scaled here to correspond to the effect at* $\lambda = 855\,\mu$m

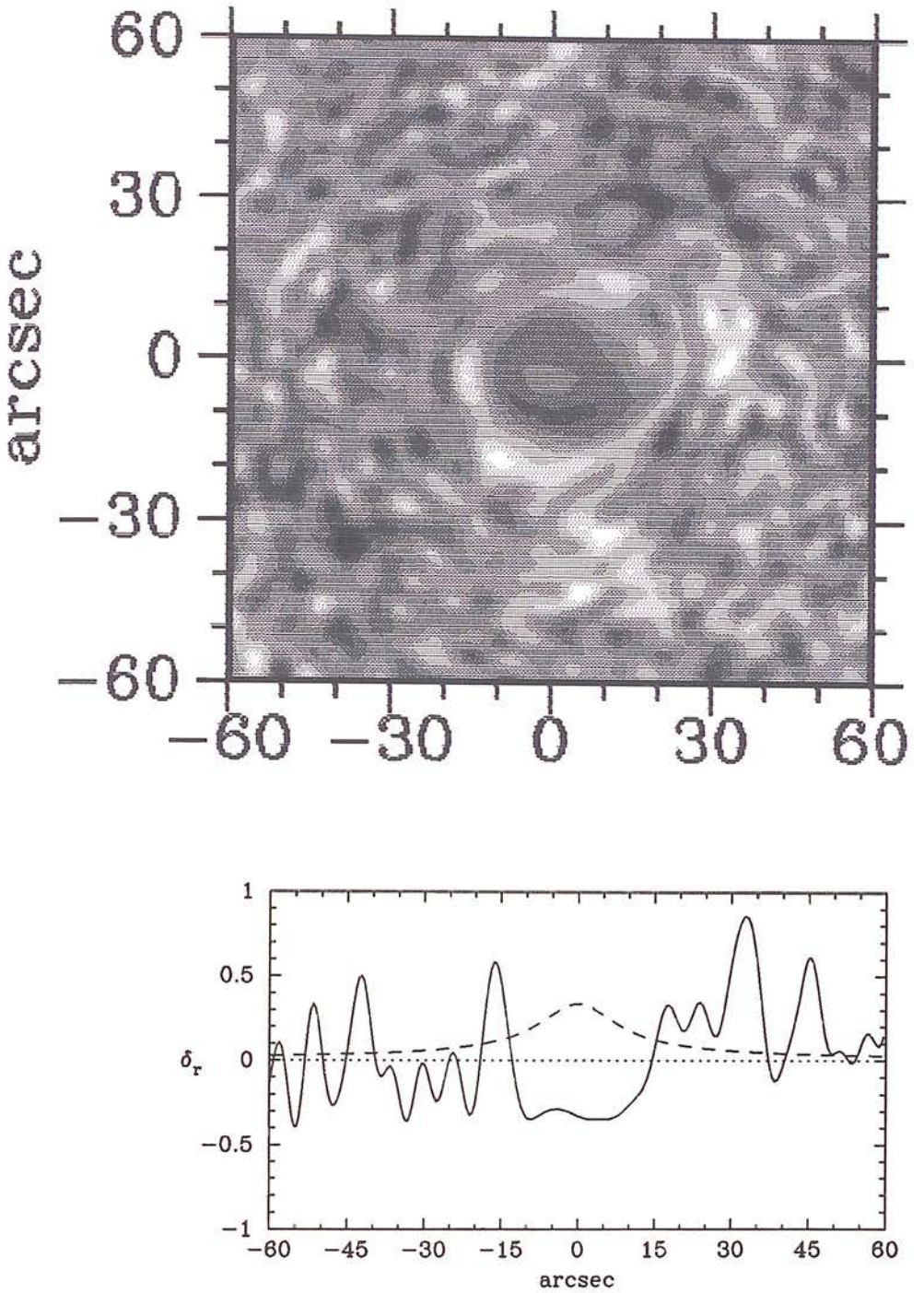

Figure 3.22: a) *Gravitational lensing by Cl2244 of the background source plane of Fig. 3.14 and* b) *the cross section as in Fig.* ~~3.22~~ 3.21

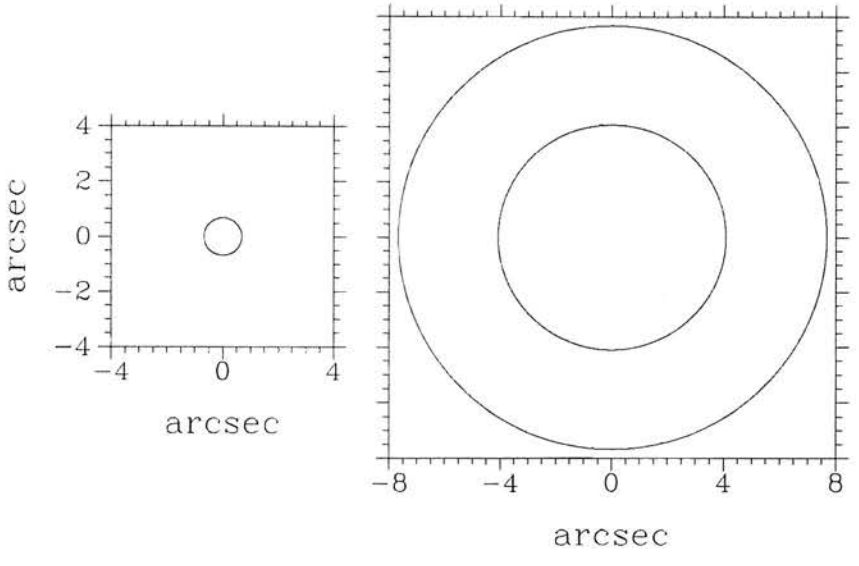

Figure 3.23: *When a source plane is placed at a redshift $z = 10$, the caustic lines for the cluster Cl 2244–02 are those shown in the left panel. The central point–caustic is mapped from the Einstein ring which is the outer critical line shown in the right hand panel. The inner critical line in the right panel maps to the circle–caustic in the left panel.*

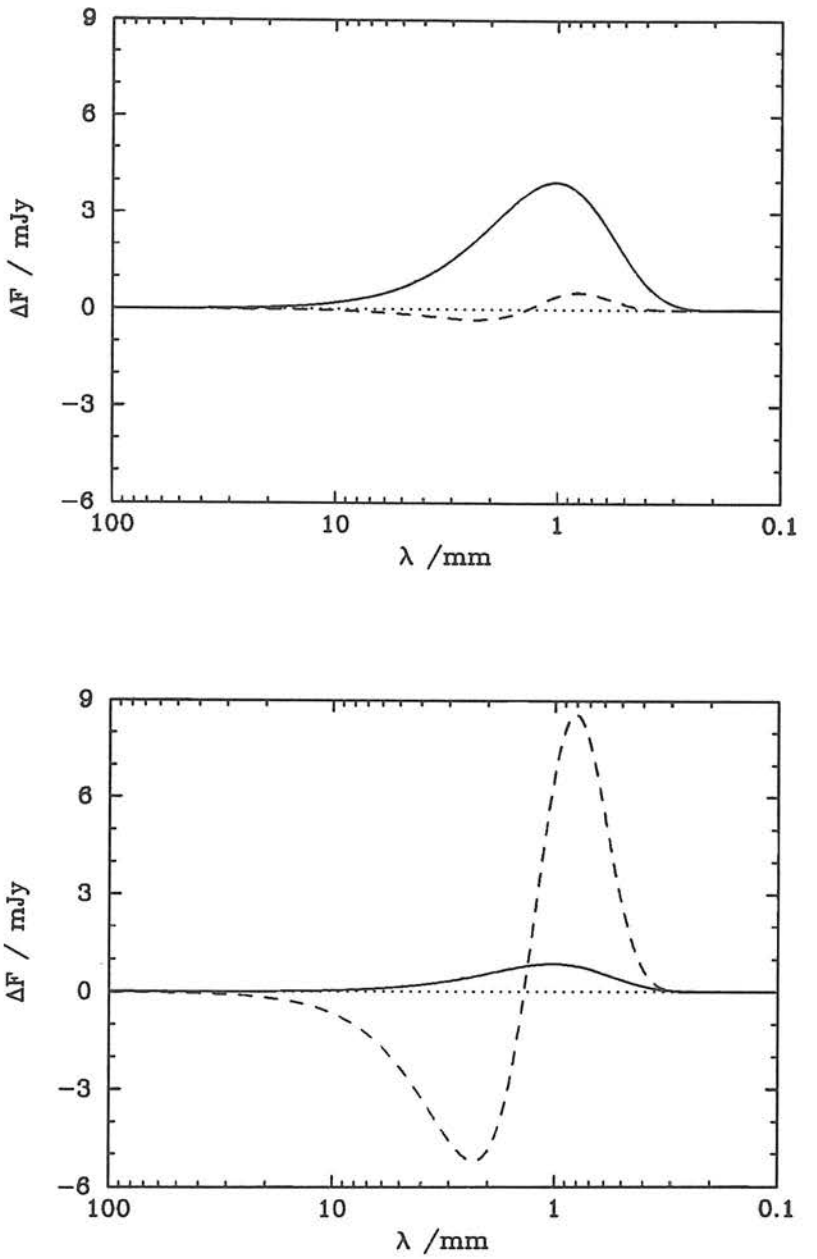

Figure 3.24: a) *The best flux in a 17.7″ FWHM beam in the field of Fig. 3.22 as a result of gravitational lensing of the submillimetre background is compared to the S-Z effect in the same beam.* b) *The lower panel shows the fluxes in the central 60″ FWHM beam of the same field.*

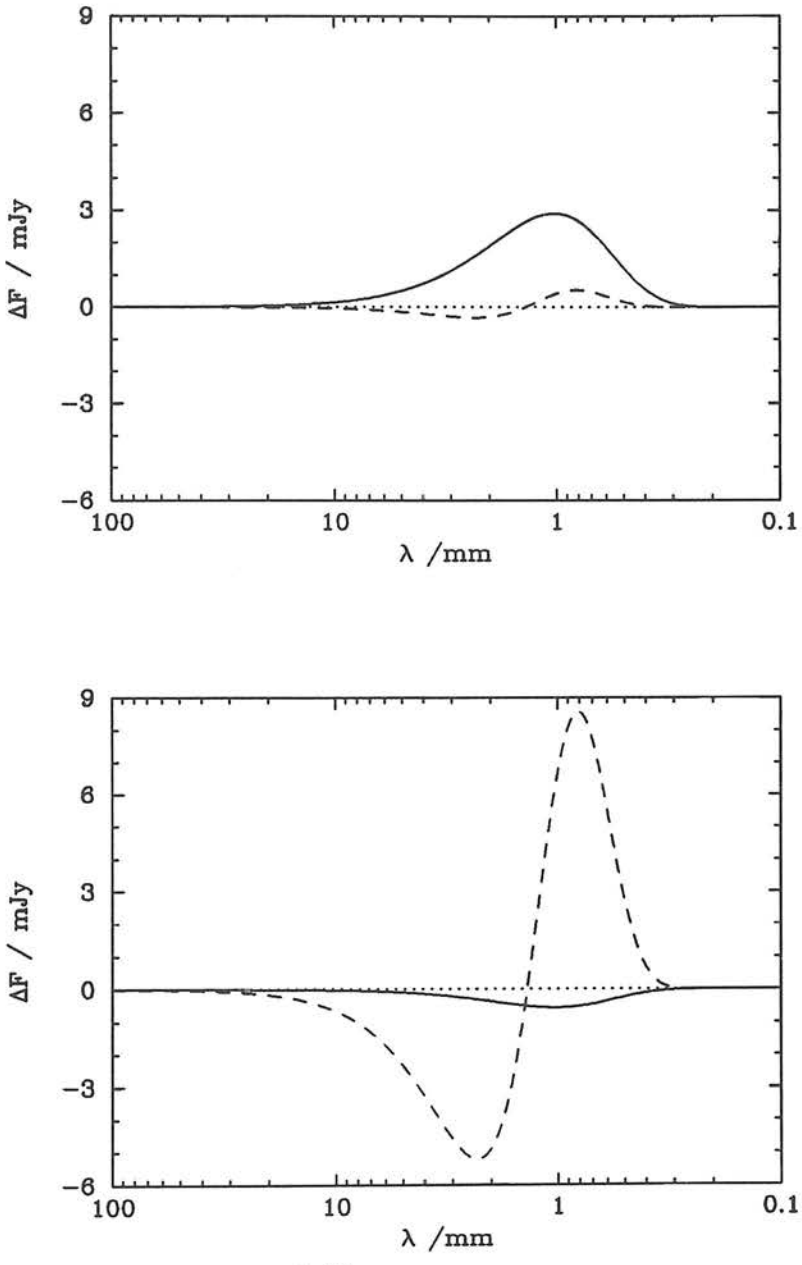

Figure 3.25: *As in Fig. ~~3.25~~ 3.24, the fluxes are shown for the image of the 5″ scale sky fluctuations.*

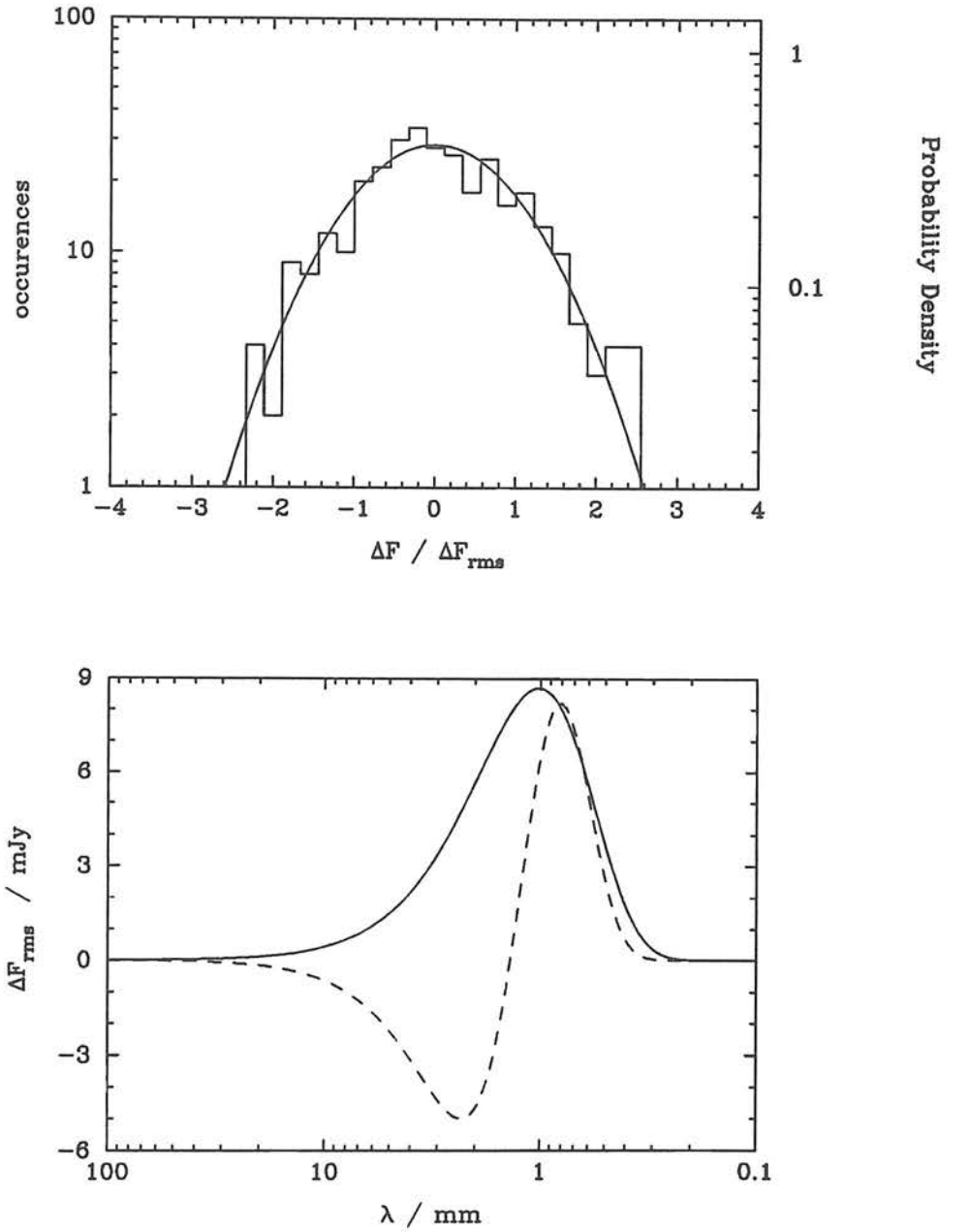

Figure 3.26: *Over 500 sky fields with $\gamma = 1.2$ and $r_0 = 10''$ were generated, and these were each used as the source plane. After gravitational lensing by Cl2244, the flux in a beam of 60″ FWHM centred on the cluster was calculated.* **a)** *This is a histogram of the central fluxes from the repeated simulations.* **b)** *The wavelength dependence of the $e^{-\frac{1}{2}}$ point of the above histogram.*

3.6.3 Case Study: 0016+16

Up to now, the analysis has concentrated on clusters which are established gravitational lenses, while underscoring the consequence of the gravitational lens effect with respect to the S-Z effect. In this section, the cluster acting as the lens is based on 0016+16 through which the microwave decrement has been tentatively measured [Birkinshaw *et al.* 1981, Andernach *et al.* 1983].

The cluster mass model is soft ($\alpha = 0.6$) and circular. It is isothermal with the electron brightness temperature $T_e = 10^8$ K being consistent with the lower limit obtained by White *et al.* [1981] of $T_e > 7.0\times10^7$. The cluster redshift is $z = 0.541$ [Koo 1981]. The central electron density is assumed to be $n_0 = 1.0\times10^{-3}\,\mathrm{cm}^{-3}$. The lensing effect is most sensitive to the velocity dispersion (indicative of the total mass of the lens), and the core radius. These were chosen to be $\sigma_v = 1300\,\mathrm{km\,s}^{-1}$ which is similar to that of A370, and $r_c = 45''$ as given by Koo [1981].

The possibility that the dark matter distribution does not follow the luminosity or velocity distribution is particularly interesting for the case of 0016+16. Dark matter can be traced non-linearly by the galaxy distribution, and this is still consistent with velocity dispersion data [Merritt 1987]. If, for example, the dark matter is highly concentrated at the cluster centre, then gravitational lens effects can come up to the same order of magnitude as the S-Z effect, even for a strong S-Z cluster such as 0016+16. However, since no luminous arcs have as yet been observed in 0016+16, the dark matter core radius will be taken as the optical one of $45''$.

Some authors present the possibility that the X-ray core radius is not equal to the optical core radius [*e.g.* Mushotzky 1984]. In the model, this could be used to alter the relative importance of the gravitational lens effect to the S-Z effect. However, a model with the X-ray core radius of $45''$ and the other parameters as stipulated is consistent with the Birkinshaw *et al.* result for the microwave decrement.

0016+16 is not a good lensing cluster because of its spread out mass, as characterized by its large core radius, and, in fact, there are no caustics for this cluster. There is still a lensing effect, however it is impossible to form an Einstein ring, or extended

arcs. The expected amplification of the submillimetre background due to lensing in the wide beam experiment is about two times. Figure ~~3.32~~ 3.31 shows the $e^{-\frac{1}{2}}$ flux point after the more than 500 simulations in the 60″ FWHM beam experiment. There is approximately twice the corresponding flux in the submillimetre sky without gravitational lensing by 0016+16. In the "best" 17.7″ FWHM beam, the amplification can be more than five times, as in the simulation presented here.

The main feature which makes 0016+16 a poor gravitational lens is the characteristic which makes it a good S-Z candidate: its large core radius. The result is that wide beam experiments are highly dominated by the S-Z effect. The submillimetre background due to dusty primeval galaxies can only interfere with the S-Z effect to a factor smaller by an order of magnitude, even with the aid of gravitational lensing. For smaller beam sizes such as the 17.7″ beam of UKT14, both the S-Z effect and the flux expected from the gravitationally lensed submillimetre background are of the same order of magnitude, when the position on the sky is advantageously chosen. Interestingly, the expected flux increment to the CBR towards the centre of 0016+16 at 855 μm in a 17.7″ beam is $\sim$10 mJy, which is within the capabilities of UKT14.

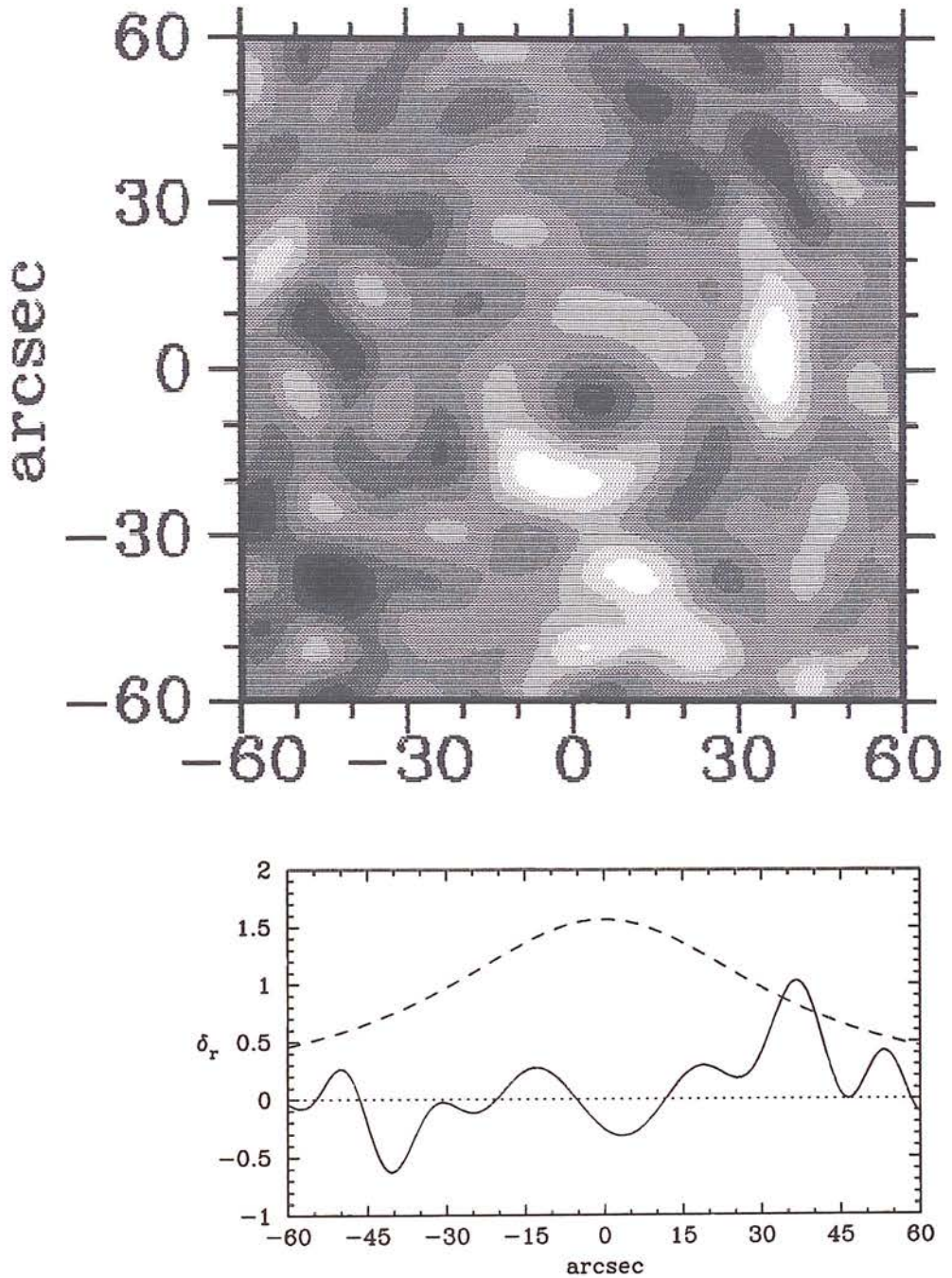

Figure 3.27: a) *Gravitational lensing by* 0016+16 *of the background source plane of Fig. 3.11 has the effect of smearing the sources into generally larger structures, despite the fact that it is not a good lensing cluster.* b) *The figure below shows a cross-section through the image plane at the centre and parallel to the x-axis. The dashed line is the spatial profile of the S-Z effect scaled here to correspond to the effect at* $\lambda = 855\,\mu$m

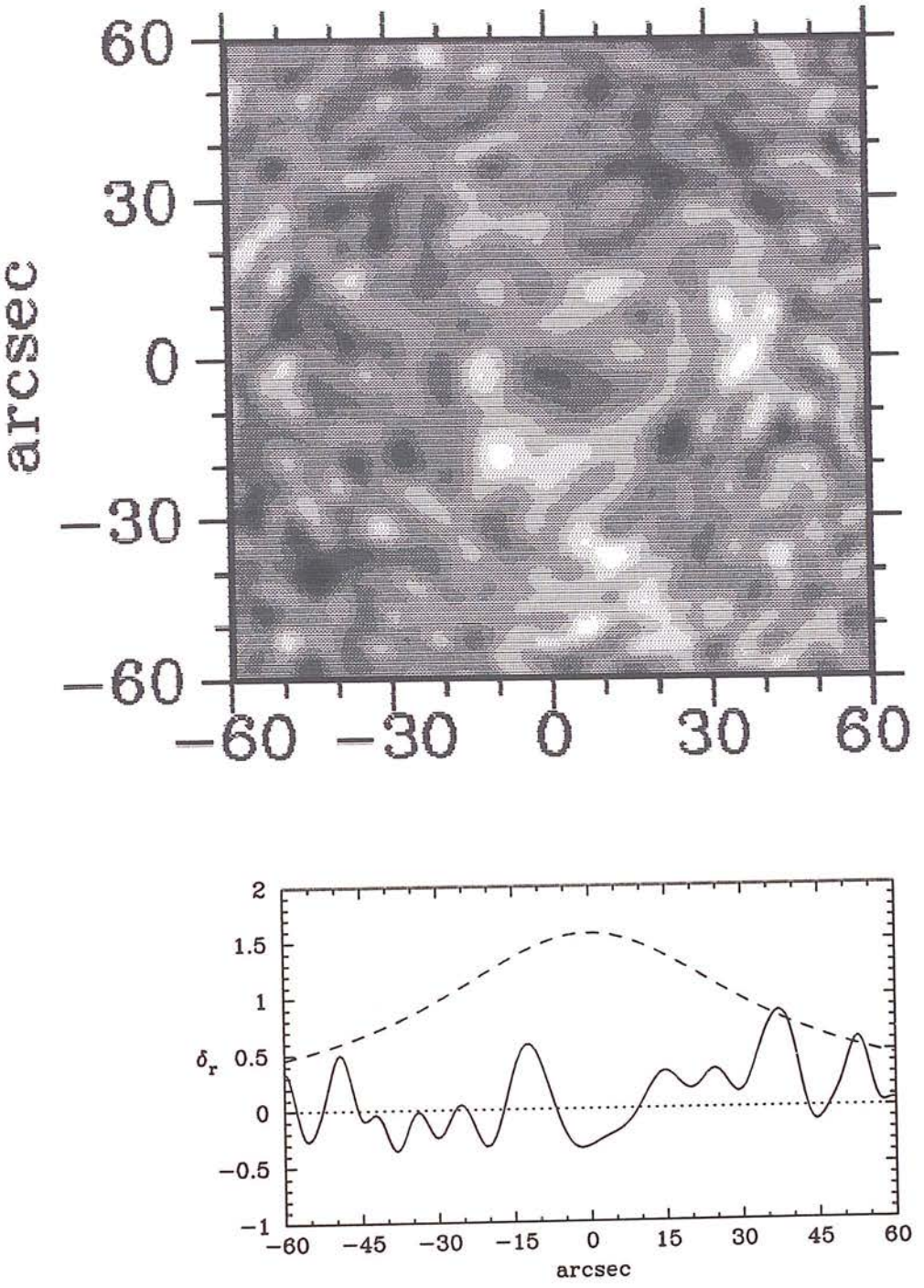

Figure 3.28: a) *Gravitational lensing by* 0016+16 *of the background source plane of Fig. 3.14 and* b) *the cross section as in Fig.* ~~3.28~~ 3.27

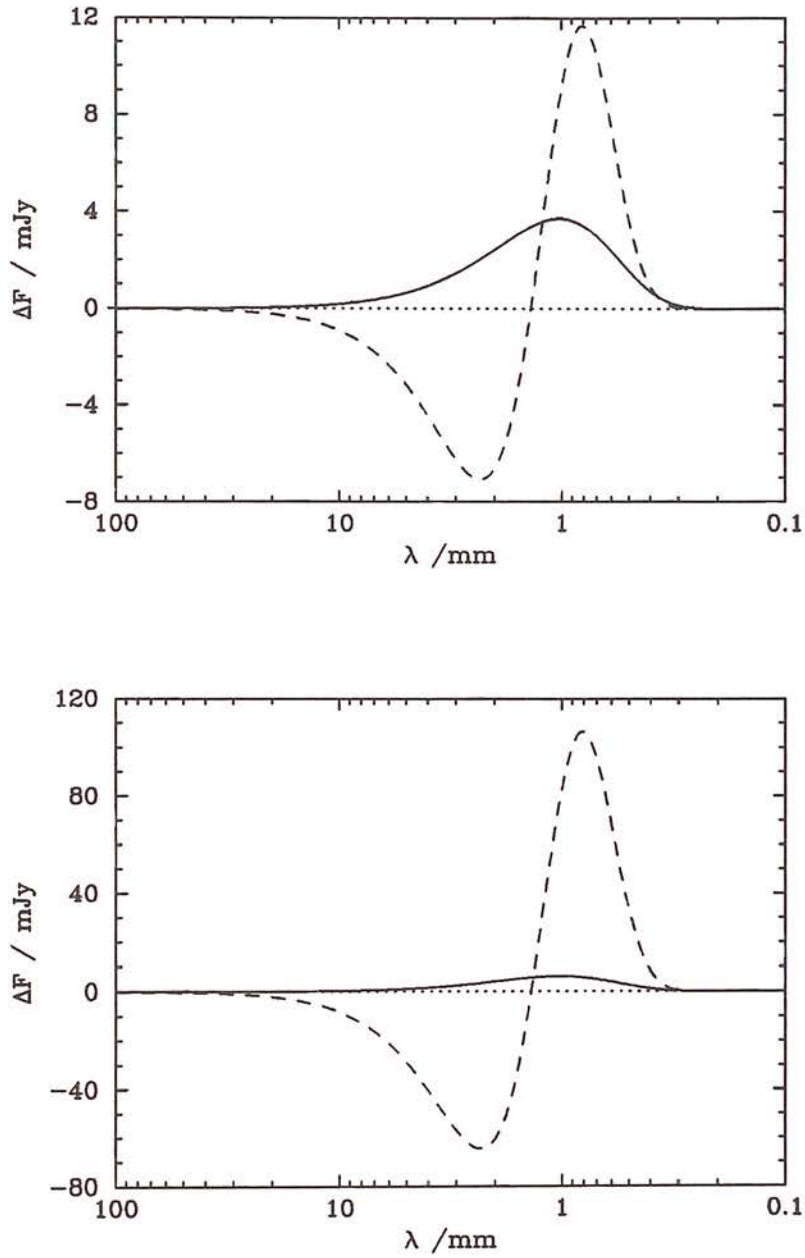

Figure 3.29: a) *The best flux in a 17.7″ FWHM beam in the field of Fig. 3.28 as a result of gravitational lensing of the submillimetre background is compared to the S-Z effect in the same beam.* b) *The lower panel shows the fluxes in the central 60″ FWHM beam of the same field.*

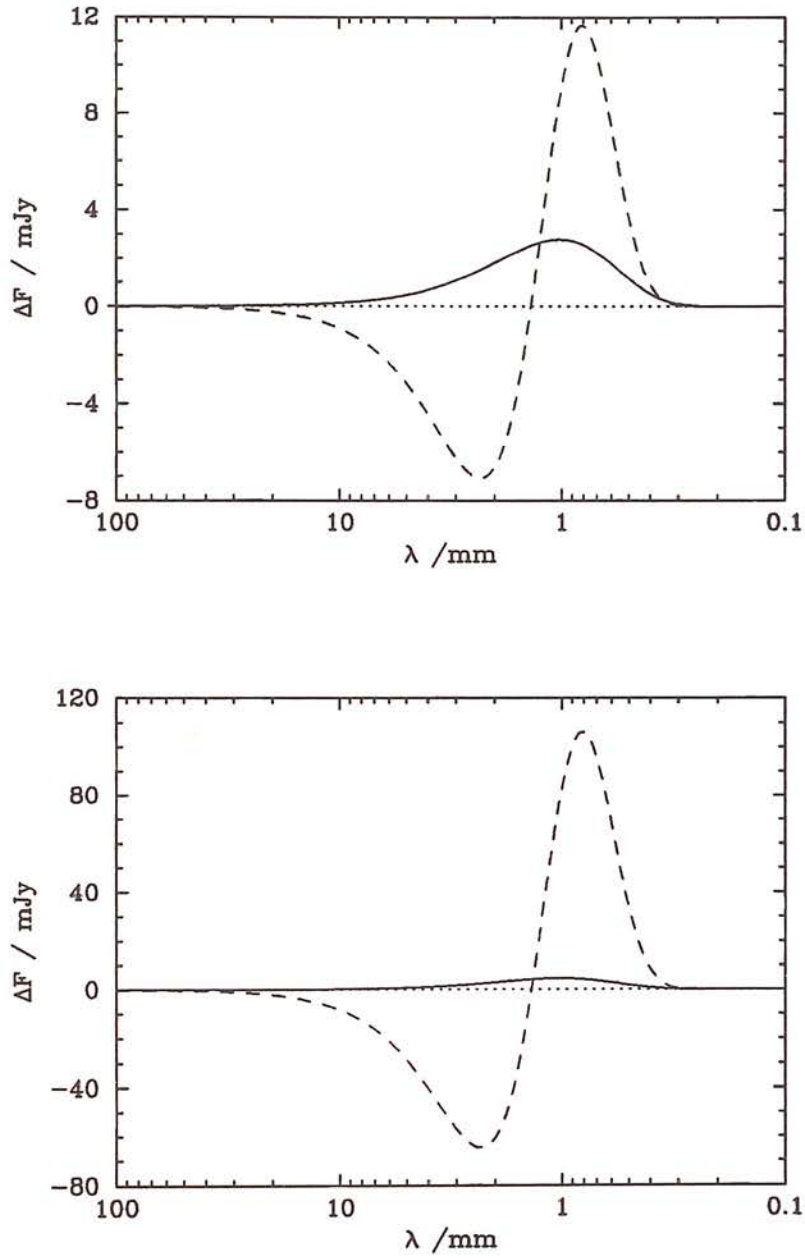

Figure 3.30: *As in Fig. ~~3.30~~ 3.29, the fluxes are shown for the image of the 5″ scale sky fluctuations.*

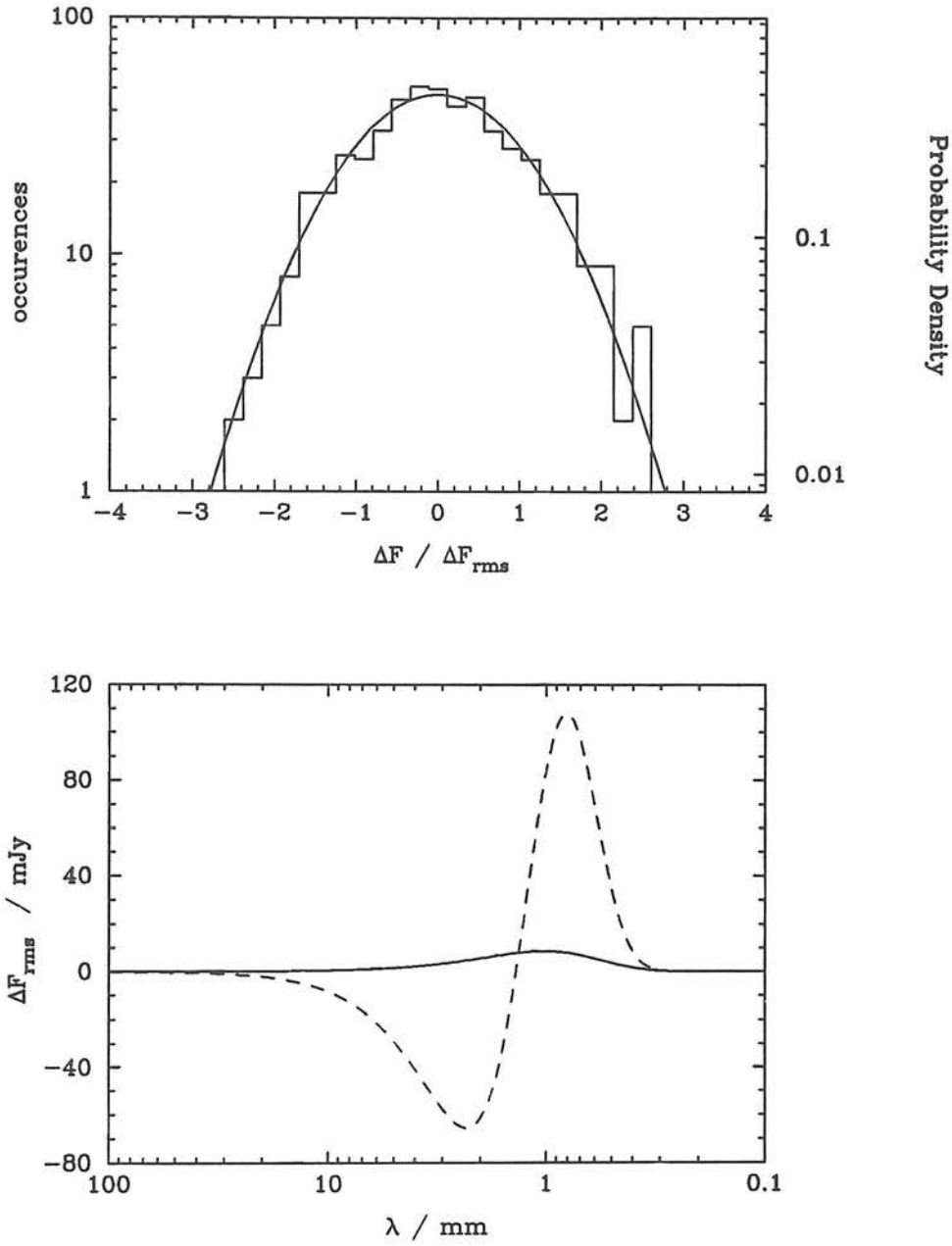

Figure 3.31: *Over 500 sky fields with $\gamma = 1.2$ and $r_0 = 10''$ were generated, and these were each used as the source plane. After gravitational lensing by 0016+16, the flux in a beam of 60″ FWHM centred on the cluster was calculated.* **a)** *This is a histogram of the central fluxes from the repeated simulations.* **b)** *The wavelength dependence of the $e^{-\frac{1}{2}}$ point of the above histogram.*

3.7 Discussion

This chapter investigated the potential of clusters of galaxies to be used as enhancers of small angular scale anisotropies in the cosmic submillimetre background through their effect as gravitational lenses. Gravitational lensing by clusters of galaxies has already dramatically shown its potential as a probe of cluster mass distribution through the optical observations of luminous arcs. The same image stretching would happen to the distant submillimetre sources which arise in many galaxy formation models.

The cluster mass model used was based on the mass potential approach of KB which qualitatively agrees with the model of GN who simulated the observations of the optical luminous arcs in Abell 370. Mass in the cluster is dominated by dark matter between the member galaxies so that for lensing effects on the scale of tens of arcseconds in Abell 370 or Cl 2244 the contributions from individual galaxies can be neglected. The two dimensional mass potential used here is non-singular, but at large distance from the cluster centre it behaves as an isothermal distribution.

The proposed sources for submillimetre gravitational lensing are a population of dusty galaxies at redshift $z = 10$. These early galaxies, possibly the first generation, would be enveloped by a dusty shell that arose from an initial burst of star formation. The result is an essentially blackbody source emitting at a temperature of $\sim$50K. In order to simulate the distribution of these sources throughout the sky, a Gaussian power spectrum was Fourier transformed, with the maximum amplitude given by a 5K blackbody. The entire microwave sky is then a combination of the uniform Cosmic Blackbody Radiation, and a distribution of 5K blackbodies forming a grey body. The filling factor of the grey body and the maximum allowable temperature of each source is strictly constrained by the recent CBR measurements made by the COBE satellite. However, this stipulation has been satisfied, and the resulting simulation of a submillimetre sky compares well with the detailed model of Bond *et al.* [1991].

With the advent of the Submillimetre Common User Bolometer Array on the James Clerk Maxwell Telescope, it will become feasible to search for non-unformities in the CBR at small angular scales, and at the Wien end of the blackbody spectrum. These

are experiments that are not within the capabilities of COBE due to its relatively wide field of view. However, difference experiments, such as that proposed here, are certainly possible from ground based telescope, and the simulations presented in this work will become testable.

One of the two interfering effects involved in a microwave increment experiment is the simple addition of a submillimetre excess. The CBR together with a patchy submillimetre background convolved with a large beam will be seen as a a single background flux that would undergo the S-Z effect. The cluster is then fed with a more energetic background that can be Compton scattered according to the S-Z effect. This will produce an over estimate of the magnitude of the S-Z effect (Fig. 3.8) even for clusters which are not good gravitational lenses.

Where gravitational lensing is important, the result can be even more dramatic, as in the simulations of A370 and Cl 2244. Here, lower energy photons are bumped into the Wien end of the CBR by the S-Z effect, and also, photons that would otherwise miss the observer, are redirected down the telescope by gravitational lensing. Figures 3.18, 3.19 for A370, and Figs. 3.24 and 3.25 for Cl 2244 compare the relative flux differences due to the S-Z and the primeval dusty galaxies. In a large beam experiment, of the order of 60″, the S-Z is the dominant contributor to the CBR distortion, but primeval dust can still comprise a large fraction of the received flux. A simple difference experiment would measure either an enhanced or diminished S-Z effect.

Even in an S-Z candidate cluster such as 0016+16, the gravitational lens effect is still important to within an order of magnitude of the S-Z effect. Figures. 3.29 and 3.30 show the measured fluxes from simulations in which the primordial dust is predominantly on 10″ and 5″ scales respectively. Added together, the two effects would lead to a spurious result if the single result was attributed only to the S-Z effect. An over/under estimate of the S-Z effect would lead to an over/under estimate of the Hubble constant.

One of the motivations for this Chapter arises from the possibility of doing the "Microwave Increment" or S-Z experiment with the new generation of highly sensitive submillimetre bolometer systems. A conclusion to be drawn from the simulations of A370, Cl 2244 and 0016+16 is that one must be careful at high frequencies since the CBR distortion may not be entirely due to the S-Z effect. Narrow beam experiments

towards clusters of galaxies will be most sensitive to the dusty primeval galaxy effect, but by mapping the clusters the smooth S-Z morphology can easily be decoupled from the bumpy nature of individual background submillimetre sources.

When S-Z experiments begin to be performed at the higher frequencies, it will be important to consider the contamination of the effect by dusty background sources enhanced by gravitational lensing. Within a year, SCUBA, the submillimetre continuum imaging receiver, will be operational on the James Clerk Maxwell Telescope. High resolution maps of S-Z candidate clusters will allow for the separation of S-Z contaminants such as emission from individual cluster members, and the effect of background source described in this chapter. The smooth S-Z spatial shape is easily differentiated from the bumpy morphology of individual sources, but a wide beam experiment will convolve all these effects together leading to a spurious result.

4 JCMT Observation of CL2244–02

The search for anisotropies in the CBR is on-going across the microwave spectrum, and at various angular scales. These include experiments, current and planned, at Antarctica [Peterson 1989], as well as rocket and balloon borne experiments [see Bond *et al.* 1991 for an overview]. The most famous is the COBE satellite already mentioned in the last chapter.

Continuing ground based investigations of the CBR in the face of such a high calibre instrument as COBE is motivated by the very small angular scales that can be probed by large ground based telescopes. Although the FIRAS instrument in COBE measured the temperature of the CBR to unprecedented accuracy, the ability of COBE, using the DIRBE instrument, to probe for anisotropy is limited to the relatively large angular scale of 7°. Cosmic submillimeter background anisotropy which would be due to dust emission has the greatest proportional amplitude at the smallest angular scales, with 10″ about the optimum hunting ground. Hence, observations from IRAM [*e.g.* Kreysa & Chini 1988, 1989] and the JCMT [Church 1990] are the best locations for submillimetre, small angular scale anisotropies. Ground based observations will not compete with COBE for constraining the spectral shape of the CBR, but since the search for spatial non-uniformities is a difference experiment, the instrumentation difficulties are much less formidable than in an absolute measurement of the CBR.

The Panel for the Allocation of Telescope Time awarded two eight hour shifts on the JCMT to make a submillimetre observation towards the galaxy cluster Abell 370 in order to detect sources magnified by the gravitational lensing effect described in the last chapter. The JCMT is operated by the Royal Observatory, Edinburgh on behalf of the UK SERC, the the Canadian NRC, and the NWO of the Netherlands. After a schedule change due to required engineering work on the JCMT, observations were moved from early June to 27-28 June, effectively putting A370 outside the observing

window of Mauna Kea at that time. As a result, the secondary target, Cl 2244 was chosen.

This Chapter presents the results from an experiment in which 850 μm observations were made towards the galaxy cluster Cl 2244−02 on the James Clerk Maxwell Telescope. Analysis of the data shows that the UKT14 bolometer system integrated the noise down at a rate somewhat slower than ideal. The noise level of the receiver was 3 mJy, but because of poor atmospheric transmission, this translates to 11.6 mJy for astronomical sources. The upper limit achieved is $\Delta T/T < 4.6\times10^{-3}$ (95% confidence). Moreover, this is the first measurement attempted at an angular scale $\lesssim 5''$ since gravitational lensing would spread a $3''$ source into a $18''$ beam, as shown in the last chapter. Alternatively, one can appeal to the amplification property of gravitational lensing and the result becomes $\Delta T/T < 1.8\times10^{-3}$ (95% confidence).

Chapter Organization

This Chapter begins in the first Section with a brief description of UKT14 which was the instrument that performed this experiment. In Section 4.2, the observing programme is outlined, and the data is presented in Section 4.3. Analysis of the data includes the receiver noise behaviour (Section 4.4) and the various upper limits that can be derived when the effect of gravitational lensing is taken into account.

4.1 The Instrument

The UKT14 bolometer system is a single element submillimetre continuum receiver which sits at the f/35 Nasmyth focus of the JCMT [Duncan *et al.* 1990]. Light is collected by a Winston Cone feedhorn and is funnelled down onto the composite germanium crystal which sits in a spherical integrating cavity cooled to 0.36 K.

The Winston cone is sometimes referred to as the "Ideal Collector", and it provides a very broad antenna profile, focussing many wave modes down to the bolometer. This topic is more closely examined in the following chapter. A bolometer system is equally sensitive to coherent and incoherent radiation, and the broad antenna profile of a Winston cone allows most of the radiation within the beam area to enter the bolometer, so UKT14 is an excellent detector of strong, thermal submillimetre emission. For fainter objects, the low sensitivity makes detection very difficult on the JCMT, but this will

be remedied in the near future when SCUBA replaces UKT14 as the continuum receiver with bolometer sensitivity approximately an order of magnitude better than UKT14.

A bolometer system will accept radiation from a very wide frequency range, and so the waveband is chosen by filters. For the present experiment, the 850 μm SCUBA test filter was employed. The centre frequency of 350 GHz and range of ± 25 GHz corresponds to a waveband between 798 μm and 920 μm, centred at 855 μm. This is a significantly smaller waveband than the 0.8 mm filter which is centred at 761 μm and spans from 603 μm to 1030 μm. The SCUBA test filter avoids a fairly substantial sky emission feature at $\sim$750 μm but as a result, less power from the source reaches the bolometer. When this filter is eventually used in SCUBA, its greater sensitivity will compensate for this power reduction. On UKT14 for the observation described here, the choice of filter was made based on the notion that reducing unquantifiable sky emission was essential in an experiment in which the sky emission would represent a very large majority proportion of the incoming power. The filter was produced at Queen Mary & Westfield College by P.A.R.Ade and his Experimental Physics group.

The aperture opening of UKT14 was set at its maximum of 65 mm which is the constraint imposed by the size of the lens. A large aperture results in a telescope beam with a wide FWHM. In conjunction with the SCUBA test filter, UKT14 has FWHM beam width of $17.7'' \pm 0.7''$ as determined during the observing run by measurements of the bright point sources Mars and Uranus. Since the experiment is one which is looking for extended patches of submillimetre emission, the wide beam was chosen as the best way to maximize flux from the source. The expectation is that the beam filling factor of the source will be very high, and a narrower filter would simply lead to a smaller flux in the same proportion to sky emission as in the wide beam experiment.

4.2 The Observing Programme

The entire two observing shifts were dedicated to continuous integration of flux from the point at RA and dec $22^h44^m29.33^s$ and $-2°21'29.0''$ (1950 epoch). This corresponds to the centre of the main luminous arc in Cl 2244, which, at 8.3″ from the centre of the nearest cD galaxy, is $\sim 11''$ from the centre of curvature of the arc: The point which is essentially coincident with the cluster gravitational centre. The 17.7″ beam of UKT14 covered the main arc, and also included part of the nearest cD galaxy, reach-

ing to within 3″ of the cluster centre. The motivation for this position were few-fold, beginning with the recent results from COBE. The constraints on a microwave excess above the CBR were originally estimated based on the Matsumoto *et al.* [1988] result which implied a flux of ~ 100 mJy per beam. This was re-evaluated down to ~ 5 mJy per beam (see Fig. 3.25), making the experiment an extremely difficult one. However, with excellent weather conditions, this was still just within the grasp of UKT14. The chosen position covers not only the observed luminous arc, but the position within which the Einstein ring from a distant ($z \gtrsim 3$) object would appear, as well as a portion of the cD galaxy. Thus, a positive detection could have been attributed to emission from either of the known optical sources, or from background submillimetre sources. Any of these possibilities would be an interesting result, and this choice of beam position maximizes the number of potential sources.

Overheads for various reasons amounted to some 60% of the observing time, and the on-source time amounted to only half the remainder because of sky chopping. Pointing checks were done approximately hourly on the nearby quasar 2223−052, and an average error for the JCMT those nights was 2.5″ with the worst pointing being 6″ off target in the middle of the first night. These pointing offsets are satisfactory for the 17.7″ beam experiment. The focus of UKT14 was adjusted three times during each night using Uranus on the first occasion, and Mars on the subsequent two. All these measurements were also used to obtain the optical depth of the Earth's atmosphere above Mauna Kea, which during two nights of stable but $\sim 50\%$ humid weather varied from $\tau = 1.1$ to $\tau = 1.2$ on the first night, and $\tau = 0.95$ to $\tau = 1.1$ on the second. The air mass through which the source position was observed ranged from 1.1 to 2.2 air masses (see Fig. 4.1). The SCUBA 850 μm test filter was found to have a conversion factor of 13.4 mJy/ μV.

The flux integrations on Cl 2244 were done in the 10/40 mode with a 100″ chop throw. This is a relatively short integration time of 5 seconds on the source position followed by 5 seconds on the reference sky position and it was chosen in order to minimize the effect of atmosphere emission fluctuations. The chop throw was always 100″ across the azimuth to a position at the same air mass, well away from the cluster. In this way, the flux from the sky position could be subtracted from that of the source position to

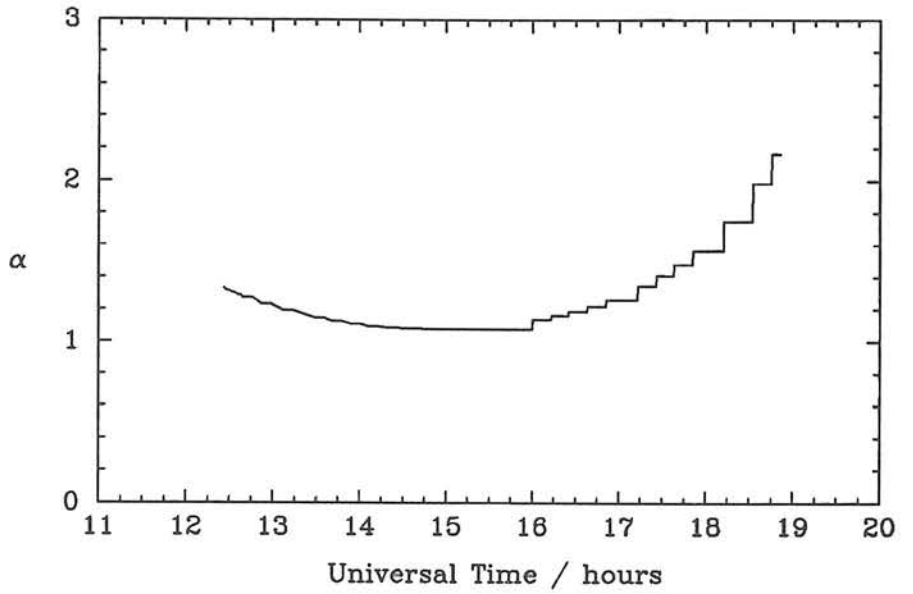

Figure 4.1: *The source transitting across the sky ended up at a position low on the horizon as shown by the high air mass at 19hr. This, along with the high optical depth, is responsible for the large scatter of the data points in the mornings of the observing run.*

give a relative flux (in units of μV) which was independent of weather and air mass throughout the observing programme. The JCMT controlling software for UKT14 took 40 of these 10 second integrations per "scan", after which the air mass was re-calculated and then a further 400 second observation was performed.

4.3 The Data

The individual 5 second integrations are represented by Fig. 4.2 in their raw form as voltage measurements. These indicate the flux differential between the source position and the sky position falling on the bolometer. Two points were rejected as being spurious and the mean signal level of 0.370 μV is 1.71 times the noise level of 0.216 μV.

Using the filter conversion of 13.4 mJy/ μV, the noise level corresponding to the standard error of 0.216 μV is 2.9 mJy. This, however, does not take into account the attenuation by the atmosphere. Nonetheless, the result does reveal the low level that one can strive for in a two-shift observing run with UKT14 on the JCMT.

Taking into account the optical depth at each integration, the same data could be used to get an absolute mean flux from the target in Cl 2244 of 20.4 mJy at 1.42 times

the noise level of 14.4 mJy. The smaller S/N ratio for the calibrated data is due to the much higher noise level as can be seen in Fig. 4.3.

The difficulty in properly accounting for the atmosphere through the optical depth and the air mass manifests itself as a greater scatter around the mean value of the flux integrations. Morning observations taken towards the end of the shift are particularly affected by this (see Fig. 4.3). However, the uncalibrated flux values in μV are much more consistent throughout the two observing shifts, as seen in Fig. 4.2. The distribution of the points is plotted in the histogram of Fig. 4.4. The distribution is nearly Gaussian indicating that the experiment measured mostly the random sky noise.

In order to recover the signal to noise attained by the uncalibrated data, one can remove the scatter in the data points, and thereby reduce the noise level, by weighting each measurement with the optical depth at that time. The error on each data point is then given by the standard error adjusted by the optical depth at that time *i.e.* $\pm\sigma \exp(\alpha_i \tau_i)$ where α_i and τ_i are the air mass and optical depth associated with the i^{th} data point. This, in effect, reproduces the data set plotted in Fig. 4.2. The best estimate of the measured signal is then

$$\Delta F_{\text{meas}} = \sum w_i \Delta F_i \Big/ \sum w_i, \quad w_i = e^{-\alpha_i \tau_i} / \sigma^2 \tag{4.1}$$

and the new standard error is also weighted as above

$$\sigma_{\text{inst}} = 1 \Big/ \sum w_i \, . \tag{4.2}$$

For the data set here, this results in the noise level of $\sigma_{\text{inst}} = 11.6$ mJy and the mean value is $\Delta F_{\text{meas}} = 19.8$ mJy at 1.71 times the noise level.

Comparing the 2.9 mJy standard error derived previously to the 11.6 mJy result gives a value for the average sky transmission over the two observing shifts:

$$\mathcal{T} = 2.9/11.6 = 25\%.$$

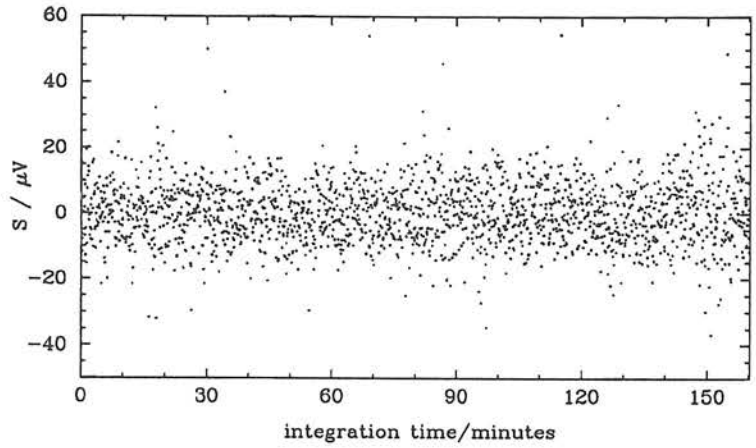

Figure 4.2: *The data consists of 1923 5 second integrations plotted here as raw points, uncalibrated to give a real flux signal. The mean signal level of* 0.370 μV *is* 1.71 *times the standard error.*

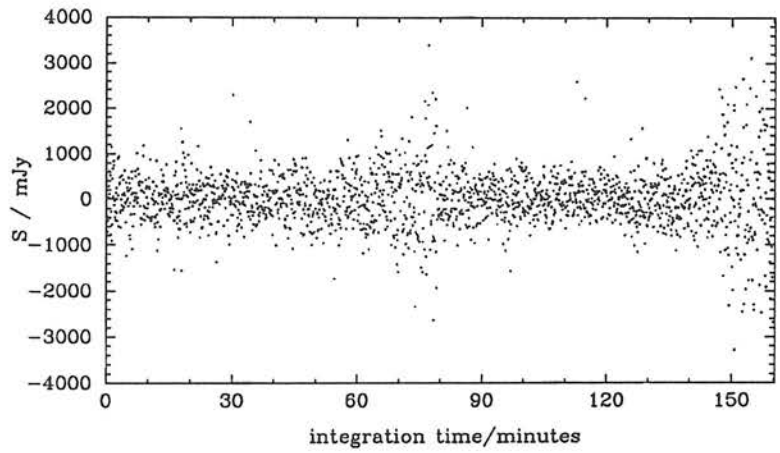

Figure 4.3: *The same data set as Fig. 4.2 is plotted here, this time as real flux measurement. As can be seen at* 75 *minutes, and* 150 *minutes, the ends of the observing nights show an increase the noise level. This effect is avoided by uncalibrated sky subtraction at equal air masses, as in Fig. 4.2. Here, the mean signal level of* 20.2 mJy *is* 1.44 *times the standard error.*

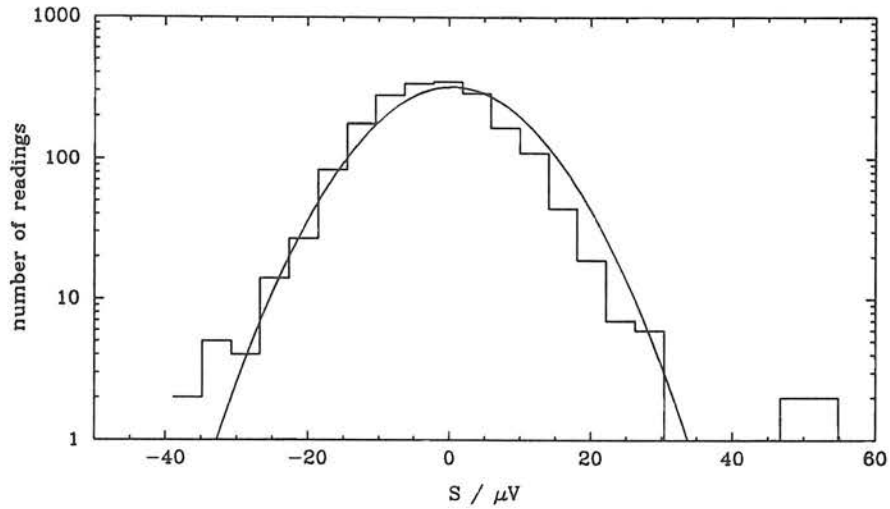

Figure 4.4: *The histogram of the points in Fig. 4.2 shows that it is a Gaussian distribution to a high degree. The solid curve is the best fit Gaussian distribution.*

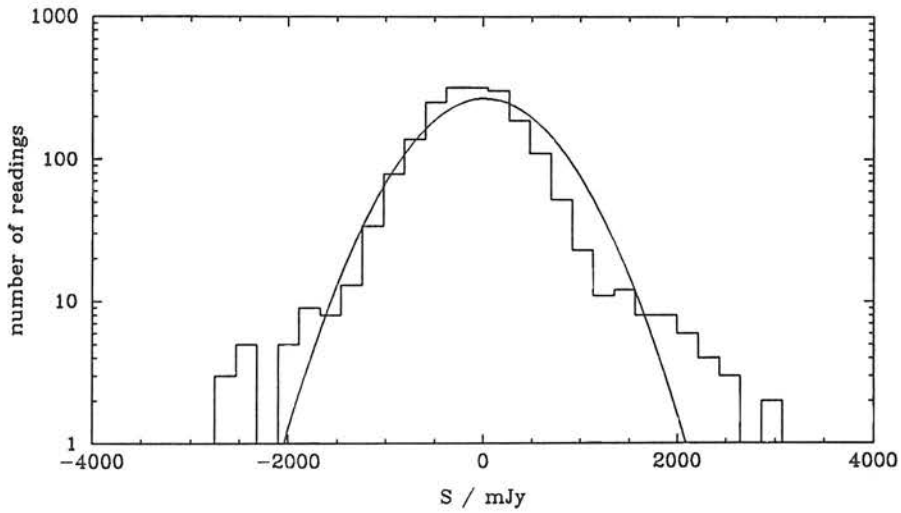

Figure 4.5: *The histogram of the points in Fig. 4.3 shows that it is much less like a Gaussian distribution than that of the uncalibrated points. The solid curve is the best fit Gaussian distribution.*

4.4 Noise Behaviour

This was an experiment which tested the limits of UKT14's deep photometry capabilities, and so a matter of some interest is the receiver's behaviour during such a long integration. The standard deviation Q is calculated in the usual manner as follows:

$$Q^2 = \frac{1}{N-1}\sum_{i=1}^{N}(x_i - \langle x\rangle)^2\,, \tag{4.3a}$$

where the mean signal is simply the average of all the integrations,

$$\langle x\rangle = \frac{1}{N}\sum_{i=1}^{N} x_i. \tag{4.3b}$$

This then is used to compute the standard error achieved through the total of 2 hours, 40 minutes, and 5 seconds of integration,

$$\sigma^2 = Q^2/N. \tag{4.3c}$$

There were $N = 1923$ data points which gave the 1.7σ 'detection' described above.

In order to plot how the standard deviation is decreasing with time, the data points are partitioned into j bins, each with N_j points, and the standard deviation is computed using the mean value of each of the j bins,

$$Q_j^2 = \frac{1}{j-1}\sum_{k=1}^{j}(\langle x\rangle_k - \langle x\rangle)^2\,. \tag{4.4a}$$

Q_j is now the standard deviation on j points which are the following,

$$\langle x\rangle_k = \frac{1}{N_j}\sum_{i=k\times N_j - N_j}^{k\times N_j} x_i. \tag{4.4b}$$

When $j = N$ then the standard deviation is the same as that computed in the normal way by Eqs.4.3. This is the first point plotted in Fig. 4.6. The second point is computed from $j = 961$ bins each with 2 points, corresponding to 10 seconds integration time. The number of bins is decreased until the last point of Fig. 4.6 which is the result of 2 bins of 961 points each, or 1 hour 20 minutes and 5 seconds integration time. The error bars on these points are derived from the standard result in Gaussian statistics that the variation on the variation is related to the σ level as follows:

$$q_j^2 = 2\sigma^2/(j-1), \tag{4.5}$$

where σ is that calculated in Eq. 4.3c. As can be seen, for short integration time, the receiver behaves ideally: Integrating down the noise in proportion to the square root of the time. After only a couple of minutes however, the noise drop gets slower, reducing in proportion to $t^{-0.40}$. This is presumably due to noise from the receiver itself, as opposed to sky noise.

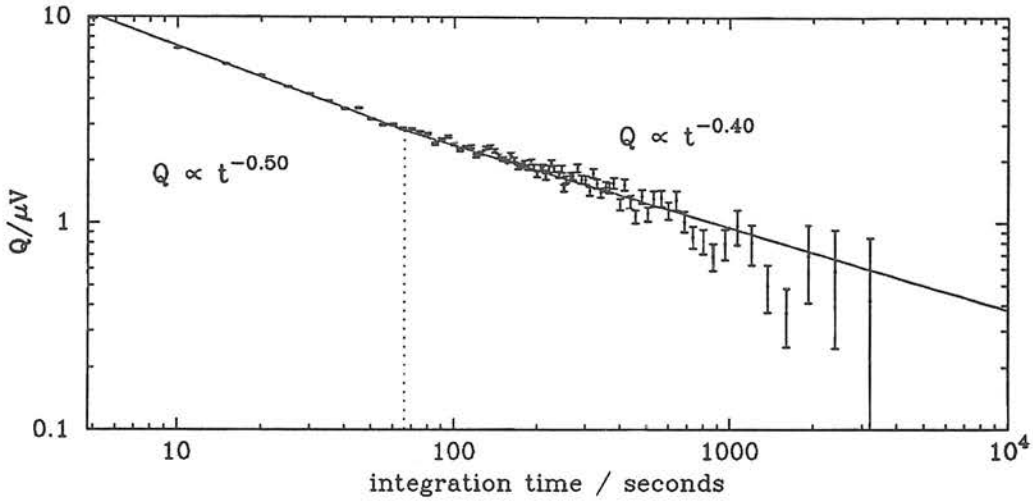

Figure 4.6: *During the first couple of minutes, the noise level on the UKT14 bolometer system integrated down at the ideal rate in proportion to the square root of the time. After this, the noise level dropped somewhat more slowly according to the dependence relation* $Q^2 \propto t^{-0.4}$.

4.5 Upper limits

The upper limit on CBR anisotropy towards Cl 2244 can be derived from the equivalent 95% confidence level of the 'detection'. If the noise level was sufficiently low, then the detection would be expressed as

$$\Delta F_{\rm true} = \Delta F_{\rm meas} \pm \sigma_{\rm inst}. \tag{4.6}$$

However, for an experiment which did not achieve enough signal-to-noise to confidently claim a detection, a 95% confidence upper limit can be derived as

$$\Delta F_{\rm true} < \Delta F_{\rm meas} + \sigma_{95\%}. \tag{4.7}$$

Given a Gaussian distribution of points about $x = 0$, the probability that a chosen point is in the range $-\infty$ to $+\Delta F$ is

$$P = \frac{1}{\sqrt{2\pi}\,\sigma_{\rm inst}} \int_{-\infty}^{+\Delta F} \exp\left(-\frac{x^2}{2\sigma_{\rm inst}^2}\right) dx. \tag{4.8}$$

This takes into account the possibility that the experiment could measure a decrement (*i.e.* negative fluctuation). The *rms*, or $e^{-\frac{1}{2}}$ point for a Gaussian distribution, is given by $\sigma_{\rm inst}$. Choosing $P = 95\%$ to give a 95% confidence upper limit, the resulting value for ΔF is

$$\Delta F = 1.645 \times \sigma_{\rm inst} \tag{4.9}$$

which defines the 95% level of $q_{95\%} = 1.645\sigma_{\rm inst}$ to be used in Eq. 4.7.

The upper limit on CBR anisotropy is derived from the 'detection' of $\Delta F_{\rm meas} = 1.71\sigma_{\rm inst}$ presented in the last Section. Thus, the upper limit on flux anisotropy at $\lambda = 850\,\mu$m is

$$\Delta F < 1.645 \times 1.71 \times 11.6\,{\rm mJy} = 33\,{\rm mJy}.$$

At 850 μm the flux from the CBR in the 17.7″ beam would be 1.1 Jy, so the relative flux anisotropy upper limit is

$$\Delta F/F < 33\,{\rm mJy}/1.1\,{\rm Jy} = 3.0{\times}10^{-2}.$$

The flux differential is simply related to the temperature differential through the Planck function so

$$\Delta T/T = x^{-1}(1 - e^{-x})\Delta F/F, \quad x = h\nu/kT = 6.19 \text{ for } \lambda = 850\,\mu{\rm m} \text{ and } T = 2.735\,{\rm K}.$$

Therefore, this experiment measured an upper limit on temperature anisotropy through the cluster Cl 2244 of $\Delta T/T < 4.6{\times}10^{-3}$ (95% confidence).

The motivation for pointing the observation towards a gravitational lens was to improve the flux level arriving at the telescope. Based on the work in the previous chapter, the upper limit on temperature anisotropy can be adjusted. As shown in Section 3.6.2, this experiment probed anisotropy on an angular scale $\lesssim 5''$. Hence the upper

limit on CBR anisotropy measured by this experiment was $\Delta T/T < 4.6{\times}10^{-3}$, 5″ scale (95% confidence). Alternatively, one can adjust the amplitude of the upper limit itself using the result in Section 3.6.2 that the equivalent amplification corresponding to the 17.7″ beam was $\sim$2.5×. This experiment claims an upper limit on CBR anisotropy towards Cl 2244 of $\Delta T/T < 1.8{\times}10^{-3}$, 18″ scale (95% confidence).

The anisotropy upper limit quoted above is for a single point on the sky, but in order to compare this experiment with the models of Bond *et al.* [1991] and the work of Church [1990], it should be translated to the equivalent *rms* fluctuation expected across the sky. This is done by assuming that a detected flux of magnitude $|\Delta F|$ at a given position on the sky is part of a Gaussian field of spatial fluctuations. Then one can define the probability that ΔF would be found at that position on the sky. Similar to Eq. 4.8, this is

$$P = \frac{1}{\sqrt{2\pi}\,\sigma} \int_{-\Delta F}^{+\Delta F} \exp\left(-\frac{x^2}{2\sigma^2}\right) dx \tag{4.10}$$

where now the *rms* σ has two components due to the spatial fluctuations ($\sigma_{\rm sky}$) and the receiver noise ($\sigma_{\rm inst}$) such that

$$\sigma = \sqrt{\sigma_{\rm sky}^2 + \sigma_{\rm inst}^2}. \tag{4.11}$$

By asserting that the probability of finding ΔF at that position is small (5%), Eq. 4.10 can be satisfactorily approximated by the mean value theorem providing a value for σ in terms of ΔF:

$$5\% = 2\,|\Delta F|/\sqrt{2\pi}\,\sigma. \tag{4.12}$$

The 95% confidence estimate for *rms* sky fluctuations is finally derived from Eq. 4.11 as

$$\sigma_{\rm sky}(95\%) = \sqrt{(15.96\,|\Delta F|)^2 - \sigma_{\rm inst}^2}. \tag{4.13}$$

The uncalibrated difference scheme measured a flux differential at the $1.71\sigma_{\rm inst}$ level, so the corresponding sky *rms* fluctuation level is $\sigma_{\rm sky} = 27.3\sigma_{\rm inst}$. This translates directly to a CBR *rms* temperature anisotropy of $\Delta T/T < 5.0{\times}10^{-2}$ 18″ angular scale (95% confidence). This is the most appropriate estimate to compare with the upper limit on

rms CBR fluctuations by Church which was 1.4×10^{-3} (95% confidence): just over an order of magnitude better.

The observations were pointed towards the optical luminous arc in Cl 2244, so it is worth investigating whether the result can be used to constrain the flux from that source, or from cluster members which may have been in the beam. In order to see if the limit is an interesting one, an extreme example of a very luminous galaxy will be considered. In particular, this will be the nearby galaxy M82 which has been extensively studied as a ~~sight~~ site of vigorous star formation [see *e.g.* Puxley 1988] with flux measurements across a wide spectrum [see Klein *et al.* 1988 for a summary].

The present experiment was measuring the 260 μm emission (850 μm redshifted by $z=2.238$). If the luminous arc is an object similar to M82 then an estimate of the flux at a given frequency is inferred from a simple power law spectral model *viz.*

$$F_\nu \propto \nu^n. \tag{4.14}$$

This method is satisfactory when one wishes to ascertain the flux at a frequency between two known values, separated by a modest energy gap. By simple interpolation between the known flux of 630 ± 24 Jy at 141 μm [Telesco & Harper 1980] and that of 30 ± 10 Jy at 400 μm [Jaffe *et al.* 1984] the spectral index is evaluated to be $n = 3.0$. The intrinsic 260 μm emission of M82 would then be 120 Jy.

It is now necessary to place M82 at the redshift of the arc. Luminosity drops off with the square of the luminosity distance which is related to the angular diameter distance (Eq. 2.6) by two factors of $1+z$:

$D_{\rm L} = (1+z)^2 D_{\rm a}$ [see Weinberg 1972, pg. 485].

Taking $H_0 = 80\,{\rm km\,s^{-1}\,Mpc^{-1}}$ for the sake of argument, and $\Omega_0 = 1$, the luminosity distance of the arc at redshift ($z=2.238$) is 10 900 Mpc. The distance adopted for M82 is 3.25 Mpc [Tammann & Sandage 1968]. Flux will drop off with the square of the luminosity distance so the estimated flux at $z=2.238$ is a factor $3.25^2/10900^2$ smaller than the 120 Jy. The estimated flux of an M82-like object at redshift $z=2.238$ is ~ 0.01 mJy.

The 95% confidence upper limit of 33 mJy does not rule out the possibility that the arc is as luminous as M82, nor even something an order of magnitude more luminous

such as Arp220 for example. It cannot, however, be anything with a luminosity several orders of magnitude greater than M82. Such objects exist. Very recently the most luminous object in the known universe has been detected at millimetre wavelengths by Rowan-Robinson *et al.* [1991]. This object at a redshift of $z \simeq 2$ should have a 850 μm flux of $\sim$40 mJy. Such a galaxy would have been detected at a high S/N ratio by this experiment.

A remaining possibility is emission from cluster members in the beam, such as the cD galaxy near the centre of curvature of the luminous arc. Once again, putting M82 at the cluster redshift of $z = 0.328$ means that the intrinsic flux at 640 μm is required. This time the spectral index in Eq. 4.14 is derived from interpolating between the 400 μm flux, and the 1 mm flux of 2.7 ± 0.7 Jy [Elias *et al.* 1978]. The spectral index is $n = 2.6$ and the assumed intrinsic flux at 640 μm is 8.8 Jy. At a redshift of $z = 0.328$, the observed 850 μm flux from M82 would be 0.05 mJy, so again, the cD galaxy can be a highly luminous object and still not have been detected by this experiment.

4.6 Discussion

An attempt was made to detect the CBR distortion due to dusty primeval galaxies by pointing the JCMT towards the cluster Cl 2244 and measuring the 850 μm flux in a 17.7″ beam. Gravitational lensing by the cluster would spread out the postulated $\sim$5″ scale anisotropy into $\sim$20″, effectively amplifying the flux from such a field of very high z sources.

Despite the rather humid weather, the use of a relatively short integration time to effectively eliminate the problem of sky emission fluctuations produced the upper limit on anisotropy of $\Delta T/T < 4.6 \times 10^{-3}$ (95% confidence). Moreover, the use of the cluster as a gravitational lens makes this the first measurement of CBR anisotropies on an angular scale $\lesssim$5″. Alternatively, the gravitational lens can be considered as an amplifier, so that the upper limit on the 18″ scale becomes $\Delta T/T < 1.8 \times 10^{-3}$ (95% confidence). The estimate on overall *rms* sky fluctuations is $\Delta T/T < 5.0 \times 10^{-2}$.

It was also investigated to see whether the flux from specific galaxies could be constrained by this experiment. The star forming galaxy M82 at the redshifts of either the luminous arc $z = 2.238$ or at that of the cluster itself $z = 0.328$ would have a 850 μm

flux lower than the 95% confidence lower limit set by this experiment of $\Delta F < 33\,\mathrm{mJy}$. Therefore the data does not rule out that the galaxy associated with the luminous arc is an extremely energetic submillimetre emitter. The discovery of such an object in a different location by Rowan-Robinson *et al.* leads to a possible future experiment of this type to determine the submillimetre luminosity of the "most luminous object in the known universe."

The noise level of UKT14 was found to drop to the low level of 3 mJy after the two observing shifts and with the noise reducing at a rate proportional to time as $t^{-0.4}$. In terms of flux actually falling on the receiver, UKT14 seems capable of achieving a 3 mJy noise level after a two shift observing run. If the sky transmission is high, then this sets an attainable goal for future UKT14 experiments of $\sim$5 mJy sensitivity level (detection of sources of 15 mJy) or better given good observing conditions.

After two observing shifts on the JCMT, the noise level was approximately a factor of five above the expected signal as predicted in the last Chapter. In order to improve the noise level by a factor of five, based on the result that noise integrated down approximately as $\sigma \propto t^{-0.4}$, the same experiment in identical weather conditions would require a further 100 hours or so. Excellent weather might enhance the receiver sensitivity by a factor of two or three, so that at the most optimistic, this experiment requires about 16 total integration hours. With overheads at $\sim$80% (considering integrations on sky positions as an overhead), one would have to ask for nine observing shifts.

It is hard to imagine how to improve this experiment, except by increasing the integration time. A minimum acceptable number of pointing checks and focus checks were performed. UKT14 worked continuously throughout the two nights without any time wasted by hardware nor software failure. Eventually, SCUBA will be able to achieve the flux levels required with reasonable observing times because it will be a more sensitive bolometer system, that is an internally calibrated array instrument so that one can do the sky subtraction on the array itself without nodding the telescope.

Part II

Feedhorn Design for SCUBA

5 Introduction to Part II

This Part looks at one of the topics at the other end of astronomy. The design of better instrumentation for observations is an activity essential to the progress of the science. Sometimes an instrument is designed with a particular experiment in mind, and quite often a more general purpose receiver is desired for a range of possibilities. The subject of this Part is some of the design considerations for a versatile submillimetre receiver which, among other tasks, will eventually perform the experiments described in the first Part of the thesis.

The experiment presented in the last chapter will be remarkably improved when the Submillimetre Common User Bolometer Array (SCUBA) is on the James Clerk Maxwell Telescope. Bolometers cooled to 0.1 K and the increased number of pixels combine to make SCUBA orders of magnitude more efficient and sensitive than the existing bolometer on JCMT. SCUBA also offers an added advantage to point source observations by employing single moded optics which improve aperture efficiency.

Previous submillimetre photometers, such as UKT14, have employed Winston cones as their radiation collectors. It is a fundamental differance in philosophy that SCUBA will have single moded feedhorns instead of the "Ideal Collector" described by Winston [1970] and Harper *et al.* [1976], but after some consideration it becomes clear that a Winston cone is not the device to use in the diffraction limit. Geometric ray-tracing reveals the great advantage of the Winston cone as a collector in which all incoming rays are eventually reflected down through the horn exit; however, in the diffraction limit a wave analysis is more appropriate. In this case the horn profile is determined by a finite number of wave modes (see Section 7.1), perhaps of the order of ten or more [Holland 1990] creating a very broad, non-Gaussian beam profile with wings beginning at a relatively high dB level. This immediately implies poor aperture efficiency since the horn field does not match well to the incoming Airy pattern (see Section 7.2.1).

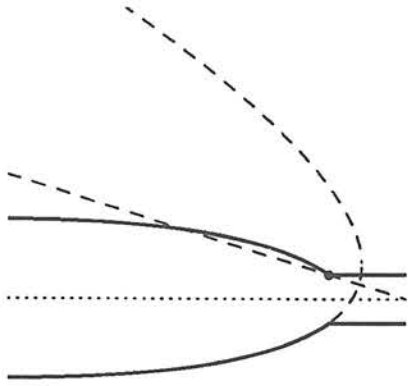

Figure 5.1: *The Winston Cone is a surface of revolution in which the generating curve is a parabola (dashed line). The parabola is rotated and revolved about an axis such that the focus (the black dot) defines the exit aperture. Thus, light entering the horn parallel to its axis reaches the exit after a single reflection.*

If aperture efficiency is not a priority, (*i.e.* point source detection is not the primary task) then the Winston cone might be appropriate if it is in the aperture plane of the telescope, where a more top-hat like profile is suitable. SCUBA is an imaging array and is therefore in the focal plane. This, along with the fact that aperture efficiency is a priority, leads inexorably to the decision that SCUBA should have single moded optics.

SCUBA will satisfy essentially all the desired criteria for submillimetre continuum observations available with present technology. The relatively large field of view, and the sky-noise limited detectors in an imaging array perhaps justifies SCUBA being called the "the definitive receiver" in submillimetre continuum astronomy. It will offer imaging capabilites in four wavebands, as well as single pixel photometry at two other frequencies: 273 GHz (1.1 mm) and 150 GHz (2.0 mm).

Feedhorns for incoherent detectors are generally designed to focus the maximum available power onto a bolometer which then absorbs it, regardless of phase. As already emphasized, the optimization of aperture efficiency and the reduction of unwanted background power entering the system requires the use of single moded optics. The conical horn has the problem of differing $\vec{E}$ and $\vec{H}$ plane profiles and somewhat non-Gaussian antenna beam profile. This is normally overcome by corrugating the feed resulting in a highly Gaussian field with suppressed sidelobes [Thomas 1978, and see *e.g.* Mahmoud 1983, Clarricoats & Olver 1984, Wylde 1984, Olver & Jun Xiang 1988, Narasimhan &

Govind 1988]. Unfortunately, manufacturing corrugated feeds for use in the submillimetre waveband is extremely difficult due to their small dimensions, and this is especially prohibitive when many horn antennas are required. Thus, although feedhorn design can become quite complex in order to satisfy stringent profile requirements, it is for the sake of manufacturing simplicity that the SCUBA horns will be conical.

This Part presents a theoretical analysis of a feedhorn system, including all the components: The horn, waveguide and the integrating cavity. The desirability of single mode optics is emphasized, and aperture efficiency, beam efficiency, ohmic losses, and wavemode scatter at the integrating cavity are all considered. The final SCUBA horn design was decided on the basis of the work presented here.

Organization of Part II

This Part is organized as follows: In Chapter 6, the first SCUBA design feature dealt with is the control of single moded wave propagation using waveguides, and also the possibility of having a single moded feedhorn without the use of a waveguide. The aperture efficiency and beam, or spillover efficiency, are discussed in Chapter 7, using Gaussian beam analysis, and in particular, the problem of having an overmoded system is addressed. Chapter 8 looks at the behaviour of the radiation as it passes into the integrating cavity, and models the absorption performance of the cavity-bolometer system, including the effect of high order modes which appear after scattering from the waveguide-cavity junction.

6 Single Mode Optics without a Waveguide

Submillimetre feedhorns are manufactured in a process involving the growth of some metal (usually copper) onto a mandrel. The mandrel can then be removed, as a plug, to leave the copper in the shape of the horn, but for very small designs, or complicated designs such as corrugations, it is necessary to etch out the mandrel, destroying it in the process. The latter situation is the one SCUBA finds itself in due to the relatively small horn dimensions. Hence, at least 128 mandrels must be fabricated.

Initial attempts by the ROE workshop to fabricate the horns met with limited success because of the transition from horn to waveguide, and also because of the very narrow waveguide diameter. The transition was slightly jagged, and the waveguide itself somewhat curved. Since a smooth transition is essential in order to prevent unwanted mode conversion, and axial symmetry is important likewise, the mandrels produced had to be rejected.

A simplification to the horn design was very welcome at this point, and doing away with the need for a waveguide would achieve the most dramatic difference to horn manufacture. Obviously, this can not be done if the single moded nature of the horn is compromised for the reasons already outlined. Nevertheless, the very narrow horn flare angle creates a device which is very close to a waveguide: high-mode attenuation begins within the horn, before radiation reaches the waveguide. As it turns out, this effect is sufficient to make the waveguide a redundant component in the 438 μm feedhorn if the high bandpass window is chosen (see Fig. 6.3). Thus, one has a totally novel approach to single moded optics achieved without the use of a waveguide.

In further developments, it was decided to contract out the manufacturing task to Thomas Keatings Inc. With a specialized high rpm CNC lathe, they will be capable of producing the feedhorns to the required specifications, including waveguides on the

smaller horns. This allows the 438 μm SCUBA horns to have waveguides and so a large bandpass option, beginning at 482 μm (619 GHz) instead of the shorter wavelength of 458 μm (655 GHz). The higher frequency horns can be made single moded without a waveguide, but the decision to go for a lower frequency window requires a larger horn exit diameter, and therefore rules out single moded optics without a waveguide.

Chapter Organization

In the following Section, the analysis is developed which describes how the cylindrical waveguide modes attenuate in a conical horn. Sections 6.2 and 6.3 relate this analysis to the particular cases of the high and low frequency observing windows on Mauna Kea, and the ones chosen for SCUBA.

6.1 Controlling the Single Mode Optics

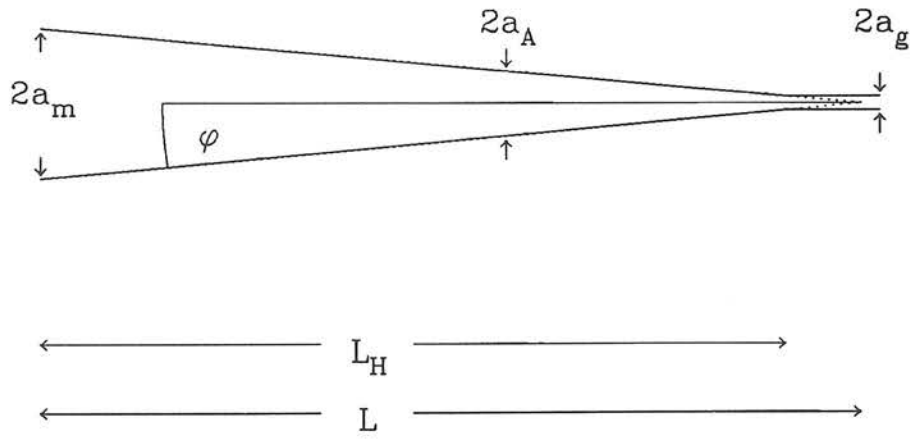

Figure 6.1: *The conical feedhorn system consists of a cone of axial length L followed by a cylindrical waveguide which feeds the radiation into an integrating cavity (not shown). The* TM_{01} *waveguide mode begins to be attenuated when the horn radius is* a_A *at a distance* $z_A - z_e$ *from the horn exit.*

Wave propagation in a cylindrical waveguide and in a conical horn with small

flare angle is considered to be cylindrically symmetric and has the form

$$\Psi(r,\theta,z) = \psi(r,\theta)e^{ikz} \tag{6.1}$$

where z is the coordinate along the horn axis, and k is the wave number in the guide (Eq. A.4e). λ is the free-space wavelength, and $\gamma_{\text{cutoff}} = 2.404$ for the TM_{01} waveguide mode, which is the second one to be excited (see Table 6.1).

Table 6.1: Beam Mode Cut-off

Mode	$\gamma_{\text{cut-off}}$
TE_{11}	1.84118
TM_{01}	2.40483
TE_{21}	3.05424
TE_{02}	3.831706
TM_{11}	3.83171

Finally, the dimensionless frequency in the guide is $\gamma = 2\pi a/\lambda$ where $a = a(z)$ is the guide (or horn) radius. For a conical horn

$$a(z) = z\tan\varphi \tag{6.2}$$

and φ is the semi-flare angle of the horn.

One can think of a conical horn as being made up of a large number of short cylinders of increasing radii. The propagation of the wave from the end of one cylinder to the beginning of the next is

$$\Psi(r,\theta,z) = \psi(r,\theta)e^{ik\Delta z} \tag{6.3}$$

and this can be generalized to an infinite number of short cylinders to get an expression for an arbitrarily contoured horn of small flare angle [see for example, Snyder & Love 1983].

$$\Psi(r,\theta,z) = \psi(r,\theta)e^{i\int k\,dz} \tag{6.4}$$

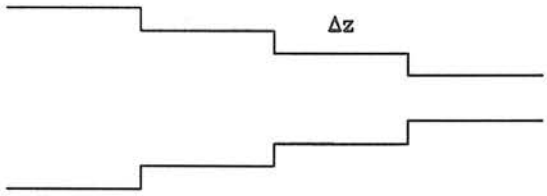

Figure 6.2: *Steps of cylinders can approximate a conical horn.*

When the horn radius is small enough, the axial term in Eq. 6.4 changes from periodic to exponential decay and the mode is attenuated. The 'Region of Attenuation' begins at the point $z = z_A$ at which point the radius $a_A = 2.404\lambda_{short}/2\pi$ is where the TM_{01} mode begins to attenuate for the shortest wavelength in the bandpass. The horn exit radius $a_e = 1.84118\lambda_{long}/2\pi$ is just big enough to allow TE_{11} propagation unattenuated for the longest wavelength in the bandpass.

The power coefficient is

$$P = \exp\left(-2\int_{z_A}^{z_e} |k|\, dz\right), \tag{6.5}$$

or in terms of the log

$$\begin{aligned}
\log P &= \log e \left(-2\int_{z_A}^{z_e} |k|\, dz\right), \\
&= \log e \left(-2\int_{z_A}^{z_e} \frac{2\pi}{\lambda_{short}} \left[\left(\frac{2.404\lambda_{short}}{2\pi z \tan\varphi}\right)^2 - 1\right]^{1/2} dz\right), \\
&= -\frac{2.088}{\tan\varphi}\left\{\ln\left[\left(\frac{a_A^2}{a_e^2} - 1\right)^{1/2} + \frac{a_A}{a_e}\right] - \left(1 - \frac{a_e^2}{a_A^2}\right)^{1/2}\right\}
\end{aligned} \tag{6.6}$$

6.2 CASE I: The 438 μm Horn

Figure 6.3 shows an atmosphere transmission model for Mauna Kea assuming 1 mm precipitable water vapour. The primary window is the one beginning at 619 GHz

(484 μm), and radiation as high as 700 GHz (428 μm) should propagate through the system. The former gives a horn exit radius of $a_e = 0.142$ mm, however, in order to allow for machining tolerance, a radius of 0.145 mm is specified. Note that there will be two moded propagation for some of the radiation in the window if the exit radius is larger than 0.164 mm ($\gamma > 2.404$ for $\nu = 700$ GHz and $a_e > 0.164$ mm). Equation 6.6 then gives

$$\log P_{438} = -0.0846/\tan\varphi \tag{6.7}$$

and if the demand is that power attenuates to 0.1%, then the horn flare angle must satisfy $\tan\varphi < 0.0846/3 = 0.0282$, or $\varphi < 1.62°$

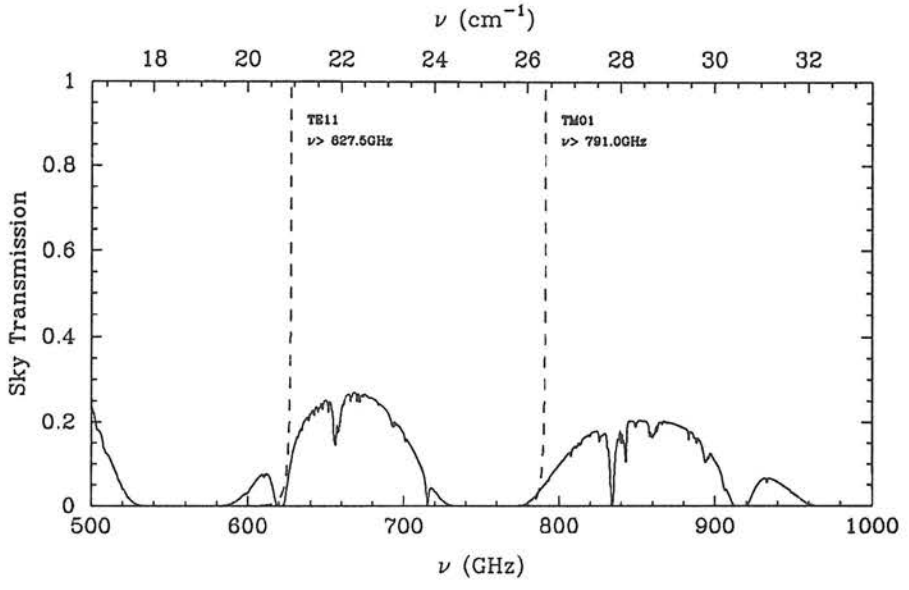

Figure 6.3: *The atmosphere above Mauna Kea assuming* 1 mm *precipitable water vapour has two distinct observing windows in the frequency range* 500 GHz $< \nu <$ 1000 GHz. *The cut-off profile of the* 438 μm *feedhorn system is plotted for the* TE_{11} *and the* TM_{01} *waveguide modes. The same horns used at* 850 GHz (353 μm) *will be two moded.*

The horn mouth radius is $a_m + \delta = F\lambda = 1.77$ mm, where $\delta = 50$ μm is the horn wall thickness, the beam F ratio is 4, and the central frequency is 660 GHz (455 μm). A horn of flare angle less than 1.62° is equivalent to a horn of length $L > 63$ mm. Space in the SCUBA cryostat constrains the horn length to less than 40 mm, and for convenience a length of 31 mm is chosen. The semi-flare angle is then $\varphi = 3.27°$. Hence, the system requires a 0.2 mm waveguide in order to attenuate TM_{01} power below 10^{-3}. For con-

venience, the waveguide length will be 1 mm which will certainly create a single moded device.

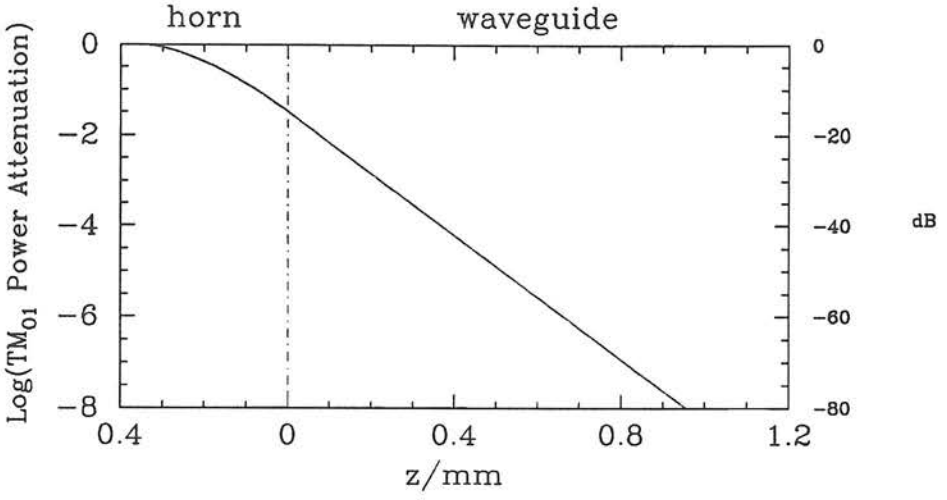

Figure 6.4: *The 438 μm horn with a length $L = 31$ mm has semi-flare angle $\varphi = 3.27°$. TM_{01} power attenuation begins at 0.34 mm from the horn exit and falls to nearly 10^{-2} by the time radiation reaches the horn exit. A waveguide of 0.2 mm length further reduces the power in the higher mode to 10^{-3}. The final design has a waveguide of 1 mm length which attenuates the TM_{01} power to virtually nil.*

With the highly sensitive bolometers in SCUBA, it is possible to have a very narrow band filter which will start after the 660 GHz sky emission feature. If the feedhorn is designed with only this window in mind, then the horn exit radius could be as small as 0.133 mm or 0.135 mm including machining tolerance. Equation 6.6 then gives $\log P_{438} = -0.154/\tan\varphi$ and if the demand is that power attenuates to 0.1%, then the horn flare angle must satisfy $\tan\varphi < 0.154/3 = 0.0514$ or $\varphi < 2.94°$. With the horn mouth radius of $a_m + \delta = F\lambda = 1.77$ mm, where the central frequency is 680 GHz (441 μm), a horn flare angle of $\varphi = 2.94°$ can be achieved with a horn of length $L = 33.3$ mm. Therefore, with a narrow band filter centred at 680 GHz (441 μm), the SCUBA horns could be single moded without using a waveguide. However, the desire to offer a wideband filter as an option necessitates having a waveguide.

6.3 CASE II: The 855 μm Horn

Figure 6.5 shows an atmosphere transmission model for Mauna Kea assuming

1 mm precipitable water vapour. The primary window is the one beginning at 331 GHz (904 μm), and radiation as high as 373 GHz (804 μm) should propagate through the system. The former gives a horn exit radius of $a_e = 0.265$ mm, however, in order to allow for machining tolerance, a radius of 0.268 mm is specified. Note that there will be two moded propagation for some of the radiation in the window if the exit radius is larger than 0.308 mm ($\gamma > 2.404$ for $\nu = 373$ GHz and $a_e > 0.308$ mm). Equation 6.6 then gives

$$\log P_{855} = -0.0983/\tan\varphi \tag{6.8}$$

If we demand that power attenuates to 0.1%, then we require

$$\tan\varphi < 0.0983/3 = 0.0328$$

$$\varphi < 1.88^\circ$$

This is equivalent to a horn of length

$$L > 102.4\,\text{mm} \tag{6.9}$$

which is far too long for the space available in SCUBA.

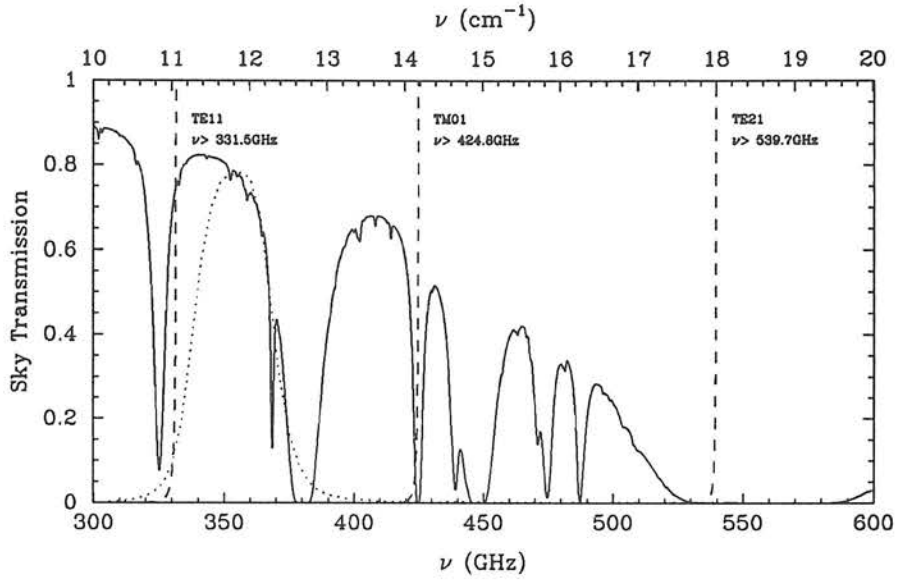

Figure 6.5: *The atmosphere above Mauna Kea assuming* 1 mm *precipitable water vapour has three distinct observing windows in the frequency range* 300 GHz $< \nu <$ 600 GHz. *The cut-off profile of the* 855 μm *feedhorn system is plotted for the* TE_{11}, TM_{01} *and the* TE_{21} *waveguide modes. The same horns used at* 408 GHz (735 μm) *will be also be single moded, and at* 478 GHz (628 μm) *they will be two moded.*

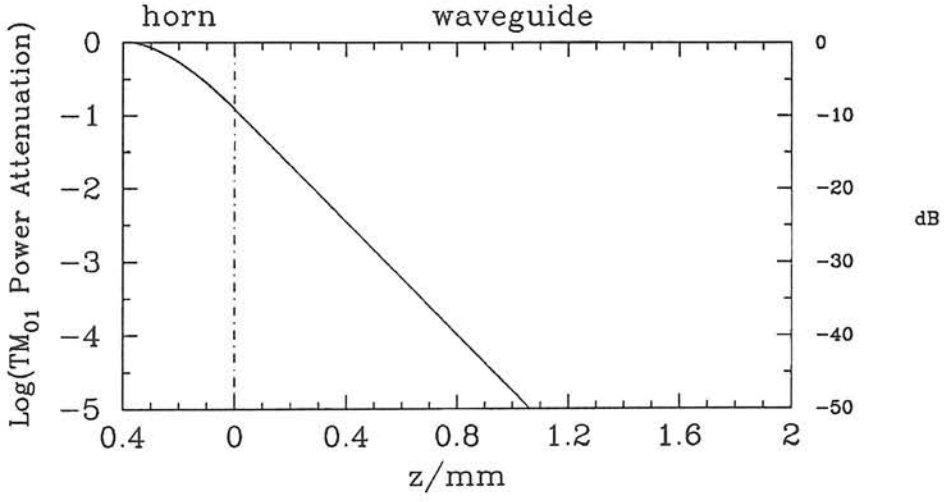

Figure 6.6: *The* 855 μm *horn with a length* $L = 31$ mm *has semi-flare angle* $\varphi = 6.18°$. TM_{01} *power attenuation begins at* 0.37 mm *from the horn exit and falls to* 10^{-1} *by the time radiation reaches the horn exit. A waveguide of* 0.5 mm *length further reduces the power in the higher mode to* 10^{-3}. *The final design has a waveguide of* 2 mm *length which attenuates the* TM_{01} *power to virtually nil.*

6.4 Discussion

Initially motivated by the desire to simplify the SCUBA horn design, the analysis presented in this Chapter was undertaken to properly understand mode attenuation in a horn-waveguide system. This became essential for choosing the appropriate length of waveguide, where needed. High mode attenuation occurs both in the horn itself and in the waveguide.

A scheme which arose out of this analysis was the possibility of creating a single moded device without the use of a waveguide. After selecting the frequency passbands based on the observing windows at Mauna Kea, the feedhorn exit radius, and the waveguide length could be determined in order to ensure single moded radiation at the primary observing windows. It was demonstrated how the 438 μm horn could be single moded without a waveguide if the high frequency, narrow bandpass was chosen. This was a major simplification to the horn design, and horn manufacture could have taken place here at the Royal Observatory, Edinburgh, with the existing equipment in the workshop. The cost of acquiring the horn components could then be greatly reduced.

When it was decided that the available man power would not be used for horn production, the task was contracted out to a specialist company. The simplification to horn design was no longer necessary since the high RPM, CNC lathe could cope with the tiny waveguides. The addition of a waveguide to the 438 μm (684 GHz) feedhorn allows the horn exit diameter to be larger, and this in turns provides for the option of a wide bandpass filter beginning at 478 μm (627 GHz). Low frequency radiation that would have been cut off by the narrow exit diameter is instead allowed to pass on into the integrating cavity in the final feedhorn design.

SCUBA will be a highly efficient receiver, not only at its original design frequencies, but also at the additional higher frequencies. In particular, Fig. 6.5 shows how the feedhorn system is single moded not only at the primary observing window (855 μm, 351 GHz), but also at the secondary window (735 μm, 408 GHz). The horn dimensions are not optimized for efficiency at the higher frequency, but the fact that they are still single moded will greatly detract from unwanted background loading during point source observations.

7 Analysis of a Conical Horn fed by an Oversized Waveguide

This chapter is a somewhat expanded version of the paper which appeared in *International Journal of Infrared and Millimeter Waves*, under the same title, last year (**vol. 11,** pp. 791-808, July 1990). Section 7.3, describing the dependence of efficiency on horn length, and discussing ohmic losses is not included in the published version. Furthermore, the horn dimensions used here are different. This is due, in part, to the conclusion of Section 7.3 which showed that the original horn length of 40 mm was longer than necessary. Finalizing the choice of observing windows in the past few months has also affected the horn dimensions.

SCUBA was originally intended to be a two-channel imaging array for simultaneous observations at 350 GHz (855 μm) and 685 GHz (438 μm) with 37 pixels at the lower frequency, and 91 at the higher. The astronomical community soon expressed disappointment that the receiver would not also take advantage of three other observing windows that Mauna Kea can offer: 481 GHz (623 μm), 428 GHz (700 μm) and 857 GHz (350 μm) [Wynn-Williams 1988]. Two options were proposed to give SCUBA this added flexibility. The possibility of including two additional arrays (four altogether) was quickly rejected as this would require complicated optics in order to split the beam into four paths. Instead, SCUBA now has a filter drum which will allow the astronomer to choose the waveband at which she will observe [Cunningham & Gear 1990].

The analysis on overmoded optics was motivated by the additional frequencies that SCUBA now offers. Each array of bolometers is designed to have optimum efficiency at the original frequencies of 350 GHz (855 μm) and 685 GHz (438 μm) respectively. The added channels will operate at a non-optimum design, on the first two arrays. The fact that the waveguide feeding the radiation into the integrating cavity is too big for the

highest frequencies means that modes higher than the fundamental TE_{11} will propagate through the system.

The use of oversized components was first looked at some time ago, and there has been a revival of interest recently. Nearly thirty years ago Taub *et al.* [1963] established the viability of using oversized waveguides. In that work an oversized circular waveguide was shown to propagate a TE_{11} beam mode without significant attenuation over a long distance. Note that although the guide was oversized, it was not overmoded. More recently, Crenn [1982,1985], and Belland & Crenn [1989] have considered the problem of an oversized and overmoded circular waveguide, in which a Gaussian beam is propagated through the guide. Theirs is an analysis near the geometrical limit, which they term the "slightly diffracted" beam. The renewed interest in the oversized waveguide has so far been restricted to the case of the very much oversized waveguide.

This chapter is devoted to the investigation of the problem of a *slightly* oversized waveguide. In analogy to Belland & Crenn's approach, this might be described as the "very diffracted" beam. Murphy & Padman [1991] have calculated radiation profiles for "few moded horns" (from tens of modes up to the geometric limit) by finding the far field radiation pattern using the Fraunhofer diffraction integral of the basic modes. This is essentially the method of Ludwig [1966] with the waveguide modes as the "source functions" (see Section 7.1). The approach to overmodedness taken in that paper is similar to this thesis except where they use the Fraunhofer diffraction integral to generate the farfield beam profile. Here, this is done by Laguerre-Gauss beam expansion [Kogelnik & Li 1966]. Additionally, the present work calculates aperture and beam efficiencies.

Chapter Organization

Section 7.1 addresses the problem of synthesizing the field profile of the horn using cylindrical waveguide modes for the source functions and Gaussian beam analysis to find the far-field profile. This is followed in Section 7.2 with a discussion of horn efficiencies. The aperture efficiency is calculated using Gaussian beam expansion to match the horn profile derived in Section 7.1 to the Airy profile of the image of a point source. Gaussian beams are also used to compute the spillover efficiency. The dependence of efficiencies on horn length is the subject of Section 7.3 which also investigates the possibility of ohmic losses in these long feedhorn devices. Finally, Section 7.4 discusses signal measurement,

using a typical astronomical source as an example.

7.1 Profile Synthesis

The far-field horn profile is determined using the method described by Ludwig [1966] in conjunction with Gaussian beam analysis [Kogelnik & Li 1966]. The usual TE_{nm} amd TM_{nm} cylindrical waveguide modes are considered the "source functions" which are then components of the far field profile. Laguerre-Gaussian beam mode analysis is very useful for determining beam truncation and beam profile throughout an optical train. For these reasons, L-G beams are employed in this analysis instead of simply Fourier transforming the horn field to get the far-field profile through a telescope.

The exact field distribution within the guide is a linear combination of the TE_{nm} and TM_{nm} fields. For a conical horn of small flare angle, the field at the horn mouth can be taken as the waveguide field propagated as a spherical wave from the horn exit to the horn mouth. This gives the usual conical horn approximation of

$$\begin{aligned} \vec{E}_{\text{horn}} &= \vec{E}_{\text{guide}} \exp(i\pi r^2/\lambda L) \\ &= \sum_n^\infty \sum_m^\infty A_{nm} \vec{E}_{nm}^{\text{TE}} \exp(ikr^2/2L) \; + \; \sum_n^\infty \sum_m^\infty B_{nm} \vec{E}_{nm}^{\text{TM}} \exp(i\pi r^2/\lambda L) \end{aligned} \tag{7.1}$$

where L is the axial length of the horn (see Figure 6.1). The $\vec{E}_{nm}$ are referred to as the "source" functions for generating the antenna beam profile [Ludwig 1966]. The A_{nm} and B_{nm} are the Fourier coefficients of the field distribution in terms of the cylindrical waveguide modes, *viz.*

$$A_{nm} = \left\langle \vec{\mathcal{F}}_s \left| \vec{E}_{nm}^{\text{TE}} \exp\left(-i\frac{\pi r^2}{\lambda L}\right) \right]_{\text{farfield}} \right\rangle \tag{7.2a}$$

$$B_{nm} = \left\langle \vec{\mathcal{F}}_s \left| \vec{E}_{nm}^{\text{TM}} \exp\left(i\frac{\pi r^2}{\lambda L}\right) \right]_{\text{farfield}} \right\rangle \tag{7.2b}$$

$\vec{\mathcal{F}}_s$ is the field of the emitting source in the far-field of the telescope. The far-field profile of Eq. 7.1 are determined by L-G beam expansion

$$\begin{aligned} \Psi_{nm} = \tfrac{1}{\sqrt{\pi}W} \left(\tfrac{2r^2}{W^2}\right)^{n/2} L_{nm}\left(\tfrac{2r^2}{W^2}\right) \\ \exp\left(-\tfrac{r^2}{W^2} + i\tfrac{\pi r^2}{\lambda R} + i\Phi + in\theta + \tfrac{2\pi iz}{\lambda}\right) \end{aligned} \tag{7.3a}$$

where the Laguerre polynomials are given by the generating function

$$L_{nm}(x) = \frac{d^n}{dx^n} L_{0\,m+n}, \quad L_{0m} = e^x \frac{d^m}{dx^m}\left(e^{-x}x^m\right), \tag{7.3b}$$

which is the well known Rodrigues' formula.

$$W = W_0\sqrt{1 + \left(\lambda z/\pi W_0^2\right)^2}, \tag{7.3c}$$

and

$$R = z\left[1 + \left(\pi W_0^2/\lambda z\right)^2\right]. \tag{7.3d}$$

W_0 is the beam waist radius which occurs at the focus of the L-G beam ($z = 0$), and Φ is the phase slippage, in addition to that of a spherical wave, relative to the fundamental L-G mode,

$$\Phi = (2m + n)\mathrm{Tan}^{-1}\left(z\lambda/\pi W_0^2\right). \tag{7.3e}$$

The functions are normalized such that the power in a L-G beam mode is unity. That is,

$$1 = \int_0^\infty \int_0^{2\pi} r d\theta\, dr\, 2\Psi_{nm} \cdot \Psi^*_{nm}$$

The best fit L-G beam occurs when $R = L$, and choosing $W = 0.768a$ maximizes the power in the fundamental L-G mode [Murphy 1988]. This is a convenient choice because it means that fewer L-G modes are required to accurately describe the waveguide modes. The Bessel functions of the horn fields are now expressed as the summation of the L-G functions:

$$J_{n-1}\left(\gamma_{nm}\frac{r}{a}\right)\, e^{i(n-1)\theta + i\frac{\pi r^2}{\lambda L}} = \sum_{p=0}^{\infty}\sum_{q=0}^{\infty} C_{pq}\Psi_{pq},$$

from which it follows that

$$C_{pq} = \frac{1}{\sqrt{\pi W P_{nm}\pi a^2}} \int_0^\infty \int_0^{2\pi} r\, d\theta\, dr\, \left(\tfrac{2r^2}{W^2}\right)^{n/2} L_{pq}\left(\tfrac{2r^2}{W^2}\right)\, J_{n-1}\left(\gamma_{nm}\tfrac{r}{a}\right) \tag{7.4}$$

$$\times \quad \exp\left(-\tfrac{r^2}{W^2} - i\tfrac{\pi r^2}{\lambda R} + i\tfrac{\pi r^2}{\lambda L} + i(n-1)\theta - ip\theta\right)$$

The phase slippage (Eq. 7.3e) is contained within the C_{pq}. Clearly, from Eq. 7.4 the C_{pq} are trivial unless $p = n - 1$. Similarly, the coefficients of the $n+1$ terms in the horn field (Eq. 7.1) are determined.

The present analysis considers a feed to be "slightly" overmoded if a few of the cylindrical waveguide modes propagate unattenuated through the waveguide. For example, the feeding waveguide has radius a_g, which, at a given frequency of radiation, supports the first three modes: the TE_{11}, the TM_{01}, and the TE_{21}. That is, the dimensionless frequency of radiation, $\gamma = a_g\omega/c$, is within the range $3.054 < \gamma < 3.832$ (at which point the TE_{02} and TM_{11} modes propagate. See Table 6.1). Table 7.1 lists the first 21 L-G coefficients ($C_{n-1\,m}$, $C_{n+1\,m}$) for each the TE_{11}, TM_{01}, and the TE_{21} waveguide modes. The total power in the first m modes up to 21 is also listed. Note that after 21 L-G modes 98.4% of the TE_{11} power is included; over 100 modes would have to be summed before 99.5% of the power would be included [Murphy 1988] (see Figure 7.1). The aperture and spillover efficiencies listed in Table 7.1 will be discussed in the next section.

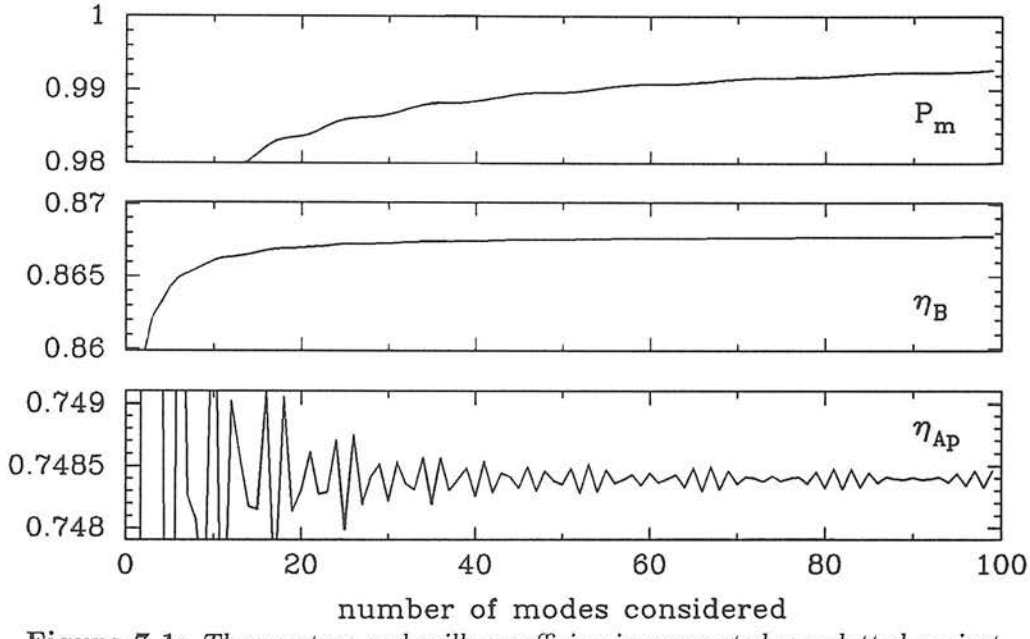

Figure 7.1: *The aperture and spillover efficiencies computed are plotted against the number of L-G modes included in the sum (Eq. 7.10 and Eq. 7.11). P_m is the amount of power included in the first m L-G modes. Twenty modes is enough to get a reasonable estimate of efficiency. This example is for the case of the infinite length horn ($\varphi = 0$) in the focal plane of the telescope.*

Table 7.1: Laguerre-Gauss Coefficients and Efficiencies

	TE_{11}						
m	C_{0m}	P_{0m}	η_{Ap}	η_B	C_{2m}	P_{2m}	η_B
0	0.93092	0.86662	0.70004	0.83743	0.22095	0.048819	0.032147
1	−0.00016319	0.86662	0.70001	0.83743	0.095791	0.057995	0.035396
2	−0.15625	0.89104	0.76961	0.84700	−0.016674	0.058273	0.035482
3	−0.078191	0.89715	0.75091	0.84886	−0.065197	0.062524	0.036768
4	0.014460	0.89736	0.75120	0.84892	−0.060891	0.066232	0.037704
5	0.058322	0.90076	0.74124	0.84982	−0.030233	0.067146	0.037902
6	0.055583	0.90385	0.75233	0.85051	0.0039529	0.067161	0.037905
7	0.027983	0.90463	0.74827	0.85068	0.028146	0.067954	0.038072
8	−0.0037052	0.90465	0.74807	0.85068	0.037652	0.069371	0.038353
9	−0.026542	0.90535	0.74721	0.85082	0.033882	0.070519	0.038558
10	−0.035721	0.90663	0.75055	0.85106	0.021389	0.070977	0.038634
11	−0.032304	0.90767	0.74666	0.85123	0.0054864	0.071007	0.038639
12	−0.020475	0.90809	0.74902	0.85130	−0.0092722	0.071093	0.038653
13	−0.0052673	0.90812	0.74857	0.85131	−0.019839	0.071487	0.038716
14	0.0089384	0.90820	0.74817	0.85132	−0.024824	0.072103	0.038810
15	0.019169	0.90857	0.74815	0.85138	−0.024270	0.072692	0.038895
16	0.024037	0.90914	0.74912	0.85146	−0.019241	0.073062	0.038946
17	0.023545	0.90970	0.74752	0.85154	−0.011361	0.073191	0.038963
18	0.018698	0.91005	0.74905	0.85158	−0.0023972	0.073197	0.038963
19	0.011056	0.91017	0.74814	0.85160	0.0060517	0.073233	0.038968
20	0.0023343	0.91017	0.74831	0.85160	0.012764	0.073396	0.038989

	TM_{01}			TE_{21}					
m	C_{1m}	P_{1m}	η_B	C_{1m}	P_{1m}	η_B	C_{3m}	P_{3m}	η_B
0	0.63775	0.40672	0.34657	0.86247	0.74385	0.63384	0.22916	0.52516	0.023088
1	0.12246	0.42172	0.35241	0.25556	0.80916	0.65926	0.17675	0.83756	0.034557
2	−0.11974	0.43605	0.35800	−0.073050	0.81449	0.66134	0.068877	0.88501	0.035785
3	−0.13845	0.45522	0.36371	−0.14359	0.83511	0.66748	−0.021223	0.88951	0.035898
4	−0.063283	0.45923	0.36471	−0.089137	0.84306	0.66948	−0.067628	0.93524	0.037047
5	0.017204	0.45952	0.36479	−0.0091024	0.84314	0.66950	−0.072405	0.98767	0.038223
6	0.063867	0.46360	0.36576	0.046965	0.84535	0.67002	−0.049955	0.10126	0.038708
7	0.071188	0.46867	0.36682	0.066016	0.84971	0.67093	−0.016718	0.10154	0.038760
8	0.050364	0.47121	0.36729	0.054843	0.85271	0.67150	0.014242	0.10174	0.038797
9	0.017211	0.47150	0.36735	0.027390	0.85346	0.67164	0.035146	0.10298	0.039022
10	−0.014682	0.47172	0.36739	−0.0028839	0.85347	0.67164	0.043279	0.10485	0.039346
11	−0.036741	0.47307	0.36763	−0.026549	0.85418	0.67176	0.039731	0.10643	0.039597
12	−0.045636	0.47515	0.36798	−0.039021	0.85570	0.67202	0.027843	0.10721	0.039713
13	−0.042167	0.47693	0.36825	−0.039846	0.85729	0.67226	0.011794	0.10735	0.039733
14	−0.029681	0.47781	0.36838	−0.031357	0.85827	0.67241	−0.0044648	0.10737	0.039736
15	−0.012565	0.47797	0.36840	−0.017265	0.85857	0.67245	−0.017868	0.10769	0.039782
16	0.0049342	0.47799	0.36841	−0.0014862	0.85857	0.67245	−0.026531	0.10839	0.039881
17	0.019464	0.47837	0.36846	0.012659	0.85873	0.67247	−0.029759	0.10927	0.040002
18	0.028922	0.47921	0.36858	0.022881	0.85925	0.67255	−0.027860	0.11005	0.040102
19	0.032490	0.48026	0.36872	0.028046	0.86004	0.67265	−0.021869	0.11053	0.040161
20	0.030457	0.48119	0.36883	0.028071	0.86083	0.67275	−0.013229	0.11070	0.040182

The C_{nm} are the coefficients of the cylindrical beam modes to the Laguerre-Gauss beam modes Ψ_{nm}. P_{nm} is the total power in the first m Gaussian modes. η_{Ap} is the aperture efficiency when the first m Gaussian modes are considered; and η_B is the beam (or spillover) efficiency when the first m Gaussian modes are considered. The total spillover of the TE_{11} mode when looking at an extended thermal source is the sum of columns 5 and 8, $\eta_B = 0.891$. The spillover efficiency of the TM_{01} mode is $\eta_B = 0.738$, and for the TE_{21} mode it is the sum of columns 7 and 10 of the lower table, $\eta_B = 0.713$. These efficiencies are for the case of an infinite length (flare angle of 0) horn: see also Figure 7.1.

7.2 Efficiencies

7.2.1 Aperture Efficiency

The aperture efficiency is the ability of the antenna to couple to a point source on the sky. A point source at infinity produces a plane wave at the telescope aperture and its field profile therefore has no azimuthal (θ) dependence. Hence, only a feedhorn profile also having such a 'symmetric' profile can couple to the point source. Of the first three cylindrical wave modes (Table 6.1), only the TE_{11} can contribute to the aperture efficiency. The point source field is diffracted into the Airy pattern at the focal plane,

$$\vec{E}_s = \frac{J_1(gr)}{gr}\hat{\mathbf{x}}\,, \tag{7.5}$$

where J_1 is the Bessel function of first order, $g = \pi/F\lambda$, and F is the f/D ratio of the telescope (here it is assumed to be a Gaussian Beam Telescope, wherein all lenses or mirrors are separated by the sum of their focal lengths [Goldsmith 1982, Padman *et al.* 1987]). An ideal aperture efficiency can be calculated by coupling the point source field directly to the horn field. This results in the maximum possible aperture efficiency which would be attained with perfect optics. The Fourier coefficients of Eq. 7.2 are then

$$A_{11} = \frac{1}{\pi a^2 P_{11}^{\mathrm{TE}}} \int_0^a \int_0^{2\pi} r\, d\theta\, dr\, \frac{J_1(gr)}{gr} J_0\left(1.841\frac{r}{a}\right) \tag{7.6}$$

The other coefficients of the first few waveguide modes are nought because only the TE_{1m} and TM_{1m} modes have a linearly polarized component to couple to the Airy profile, which is essentially a plane wave. For an infinitely long horn (*i.e.* no phase correction at the horn mouth) Eq. 7.6 is maximized at $a = F\lambda$ for a coupling of $A_{11} = 0.865$ which gives the maximum possible aperture efficiency of $\eta_{\mathrm{Ap}} = 0.748$ when the horn is placed at the image of the focal plane (compare this to $\eta_{\mathrm{Ap}} = 0.837$ when the horn is in the aperture plane [King 1950, Murphy 1988]).

For a practical horn, the focal plane does not occur at the horn mouth but at some distance within the horn, so Eq. 7.5 is first expressed as a sum of L-G beams at the waist ($z = 0$). The coefficients of the Airy profile in terms of the L-G beams can be calculated directly by taking the inner product of the Airy and L-G modes, but it

is simpler to exploit the fact that L-G modes are unchanged by Fourier transformation except for a multiplicative term $(-1)^m$ [Padman *et al.* 1987] where m is the degree of the L-G mode, and note also that the beam waist radius at the aperture plane is related to that of the focal plane by

$$W_{\rm Ap} = \lambda f/\pi W_{\rm F}. \tag{7.7}$$

f is the focal length of the lens or mirror in the Gaussian Beam Telescope [Padman *et al.* 1987]. The integrals

$$\alpha_m = \frac{(-1)^m}{\pi(F\lambda/\pi)^2}\int_0^{2\pi}\int_0^{F\lambda/\pi} r d\theta dr\, \Psi_{0m} \tag{7.8}$$

with the substitution of Eq. 7.7 in Eq. 7.3 are more easily evaluated than the focal plane integrals which extend from 0 to infinity in r. Once the α_m have been determined, this L-G beam must be propagated up to the horn mouth which is simply done by modifiying the α_m by the phase slippage that occurs because the horn phase centre of radius occurs within the horn instead of at the horn mouth. Equations 7.3c and d can be inverted:

$$W_0 = W\left[1+\left(\pi W^2/\lambda L\right)^2\right]^{-\frac{1}{2}}, \tag{7.9a}$$

$$z = R\left[1+\left(\lambda L/\pi W^2\right)^2\right]. \tag{7.9b}$$

Employing the orthogonality of the L-G beams, the coupling coefficients of Eq. 7.2 are then

$$A_{11} = \sum_{m=0}^{M} \alpha_m C_{0m}, \tag{7.10}$$

and the aperture efficiency is $\eta_A = A_{11}^2$. Table 7.1 lists the aperture efficiency for the case of the infinite length horn, and Column 2 of Table 7.2 lists the α_m. Enough L-G modes must be included in the sum (M in Eq. 7.10) to get an accurate calculation of the aperture efficiency. After about 20 modes the result changes only in the fourth decimal place (the value after 100 modes is $\eta_A = 0.7483$, see Figure 7.1.)

An example is given here which corresponds to the 855 μm feedhorn of SCUBA which has an axial length of 31 mm. In this case the telescope beam is f/4 (after re-imaging the f/12 beam of the JCMT). The horn mouth radius $a_m = 0.985F\lambda$ at $\lambda =$

852 μm is less than the optimum $a_m = F\lambda$ to allow for the horn wall thickness of $\sim$50 μm and to ensure that the horn centres are $2F\lambda$ apart (the Nyquist sampling rate is $F\lambda/2$ so the horns are an integer number of "Nyquist" units apart). The feed is single moded at 852 μm and has L-G beam width at the horn mouth of $W = 0.768a = 2.58$ mm; the waist is $W_0 = 0.602a = 2.02$ mm which occurs at $z = 3.55a = 11.9$ mm behind the horn mouth; the phase slippage is $\Phi = 0.669(2m + n)$radians. This gives an aperture efficiency of $\eta_A = 0.677$.

When the same feed is used at the window centred at $\lambda = 740$ mm then the horn mouth radius is $a_m = 1.14F\lambda$; the beam width at the horn mouth is the same $W = 0.768a = 2.51$ mm; but the waist is now $W_0 = 0.568a = 1.91$ mm at $z = 4.19a = 14.1$ mm behind the horn mouth, and the phase slippage is $\Phi = 0.739(2m + n)$radians. The aperture efficiency in this case is $\eta_A = 0.664$. This system can still be considered single moded because the rather long waveguide of 2 mm attenuates the TM_{01} mode down to about 10^{-2} in power.

At the higher frequency of 481 GHz (623 μm) the same feed gives an aperture efficiency of 0.633, but both the TE_{11} and the TM_{01} waveguide modes will propagate. There are two sources of loss in a non-optimized system. The aperture efficiency is reduced because the horn mouth is too large, and if it is overmoded, then the background loading is increased significantly which degrades the signal-to-noise of the device. This second effect is discussed in section 7.5.

7.2.2 Spillover

The beam efficiency in a Cassegrain telescope is defined as the fraction of power in the antenna beam which intercepts the image of an extended source through the telescope aperture. A source is considered to be extended if its angular extent exceeds the beam size of the telescope. The fraction of power which does not see the source on the sky "spills over" the telescope secondary mirror and looks at the entire sky surrounding the telescope beam. For this reason, the beam efficiency as defined here is often termed "spill over efficiency" in radio astronomy [Christiansen & Högbom 1985]:

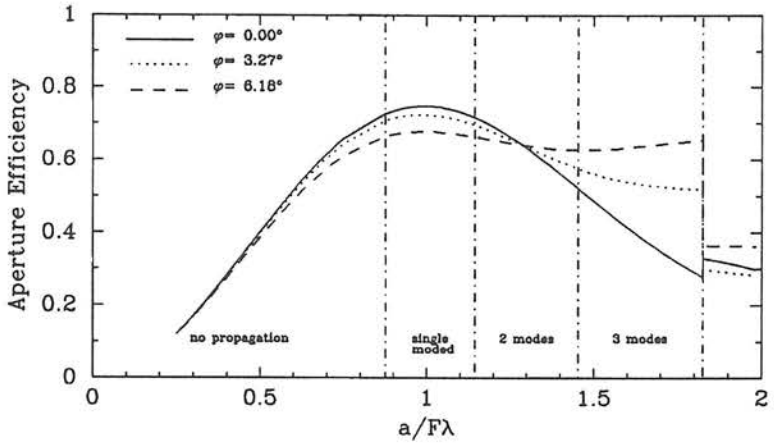

Figure 7.2: *The aperture efficiencies of three conical horns in the telescope focal plane are compared. Each is assumed to be fed by a single moded waveguide when the horn has maximum aperture efficiency ($a_m = F\lambda$ when $\gamma = a_g\omega/c = 1.9$ in all three cases). The three horns are the infinite horn ($\varphi = 0°$), and the two SCUBA horns discussed in the text ($\varphi = 3.27°$ and $\varphi = 6.18°$).*

$$\eta_B = \sum_{m=0}^{M} \frac{C_{n-1m}^2}{\pi b^2} \int_0^b \int_0^{2\pi} r\, d\theta\, dr\, |\Psi_{n-1m}|^2 + \sum_{m=0}^{M} \frac{C_{n+1m}^2}{\pi b^2} \int_0^b \int_0^{2\pi} r\, d\theta\, dr\, |\Psi_{n+1m}|^2 . \tag{7.11}$$

where b is the radius of the image of the secondary mirror (the aperture plane).

The C_{nm} are the coefficients of the L-G functions, and M is the total number of L-G modes which are considered in the sum to approximate the field profile through the optical train, and n is the order of the cylindrical beam mode (Eqs. A.4a to d) supported in the feed. The final four columns of Table 7.2 list the beam efficiencies associated with each L-G mode (*i.e.* the integrals of Eq. 7.11) for the case of the infinite length horn. Finally, performing the summation of Eq. 7.11, the beam efficiency for each mode is calculated (see columns 5 and 8 of Table 7.1a, and columns 4, 7, and 10 of Table 7.1b). The overall spillover efficiency of the feedhorn depends on the number of waveguide modes propagating through the system, and on the nature of the signal to be measured (see Section 7.4). For the SCUBA feedhorn system, the spillover efficiency

Table 7.2: Laguerre-Gauss – Airy Coupling, and Beam Efficiencies

m	Ψ_{0m} – *Airy*	η_B			
	α_m	Ψ_{0m}	Ψ_{1m}	Ψ_{2m}	Ψ_{3m}
0	0.89877	0.96632	0.85212	0.65849	0.43964
1	0.10264	0.57907	0.38919	0.35410	0.36713
2	−0.25987	0.39179	0.39002	0.30666	0.25879
3	0.13714	0.30459	0.29772	0.30263	0.25049
4	0.011770	0.30402	0.25116	0.25245	0.25131
5	−0.098824	0.26439	0.25087	0.21651	0.22416
6	0.11543	0.22300	0.23780	0.21162	0.19471
7	−0.083778	0.21133	0.20904	0.21097	0.18323
8	0.031666	0.21124	0.18835	0.19796	0.18390
9	0.018706	0.20181	0.18319	0.17886	0.18231
10	−0.054093	0.18375	0.18323	0.16562	0.17267
11	0.069610	0.16851	0.17799	0.16169	0.15928
12	−0.066508	0.16219	0.16647	0.16194	0.14903
13	0.049638	0.16173	0.15438	0.15989	0.14487
14	−0.025242	0.16062	0.14690	0.15322	0.14476
15	−0.00065582	0.15523	0.14469	0.14410	0.14464
16	0.023238	0.14661	0.14472	0.13626	0.14171
17	−0.039341	0.13823	0.14341	0.13195	0.13585
18	0.047505	0.13289	0.13916	0.13087	0.12898
19	−0.047750	0.13100	0.13279	0.13097	0.12338
20	0.041211	0.13090	0.12643	0.13006	0.12030

The first 21 L-G coefficients of the Airy field pattern are listed for the case of the infinite length horn. (The waist, $W_0 = 0.768a = 0.768F\lambda$, occurs at the horn mouth.) The spillover efficiencies in columns 3 to 6 are those associated with each L-G beam with $W = 0.768a$

when it is single moded ($\lambda = 852\,\mu$m,$\nu = 352$ GHz) is $\eta_B = 0.742$. The spillover in the higher frequency window (423 GHz, 740 μm) is 0.789. The spillover associated with each waveguide mode in the overmoded feed (481 GHz, 623 μm) is 0.832 and 0.607 for the TE_{11} and TM_{01} respectively.

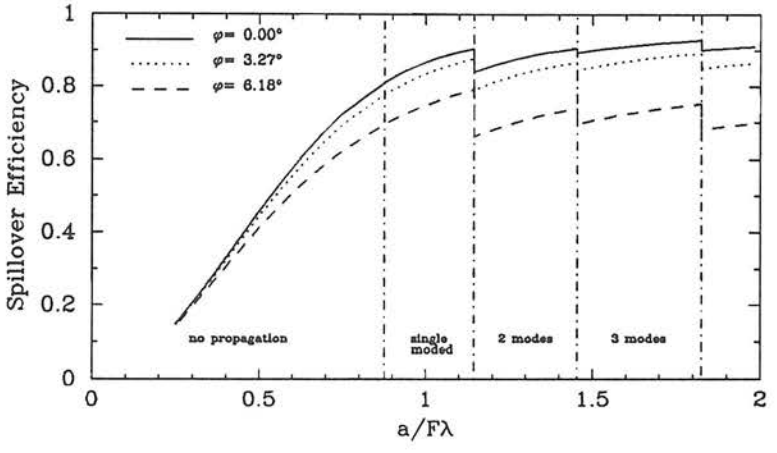

Figure 7.3: *The spillover efficiencies of three conical horns in the telescope focal plane are compared. Each is assumed to be fed by a single moded waveguide when the horn has maximum aperture efficiency ($a_m = F\lambda$ when $\gamma = a_g\omega/c = 1.9$ in all three cases). The three horns are the infinite horn ($\varphi = 0°$), and the two SCUBA horns discussed in the text ($\varphi = 3.27°$ and $\varphi = 6.18°$).*

7.3 Choosing the Horn Length

The length of the feedhorn is limited by space available in the SCUBA cryostat (40 mm), but the criterion of high aperture efficiency demands a long horn. Also, ohmic losses should be considered in a feed system with such long components since this could become a constraining factor. This Section addresses these two considerations for horn length showing in Section 7.3.1 that greater than ~30 mm length, aperture efficiency doesn't improve significantly, and in Section 7.3.2 ohmic losses are shown to be most important in the waveguide itself, with the overall power loss being negligible.

7.3.1 Efficiency Dependence on Horn Length

The analysis so far has assumed the horns are of length $L = 31$ mm. Originally the SCUBA project proposed 40 mm length horns in order to have high aperture efficiencies [Gear *et al.* 1986 "The Blue Book"]. As it turns out, a minimum permitted aperture efficiency of 65% allows the horns to be shorter than 40mm.

The following figures show the dependence of aperture efficiency and spillover efficiency on horn length for the 855 μm horn which has mouth radius $a_m = 3.35$ mm (less than the optimum $a_m = F\lambda$ because of the finite horn wall thickness), and the same horn at 700 μm and 600 μm. If a minimum standard of $\eta_{\rm Ap} = 0.65$ at 855 μm is set then a horn length $L = 23.4$ mm is required. For $\eta_{\rm Ap} = 0.70$, we need $L = 32.0$ mm. The corresponding spillover efficiencies are $\eta_{\rm B} = 0.69$ and$\eta_{\rm B} = 0.77$ respectively.

The horn length is related to the semi-flare angle φ by

$$L_{855} = \frac{a_m - a_e}{\tan\varphi} = \frac{3.08}{\tan\varphi} \text{ mm.}$$

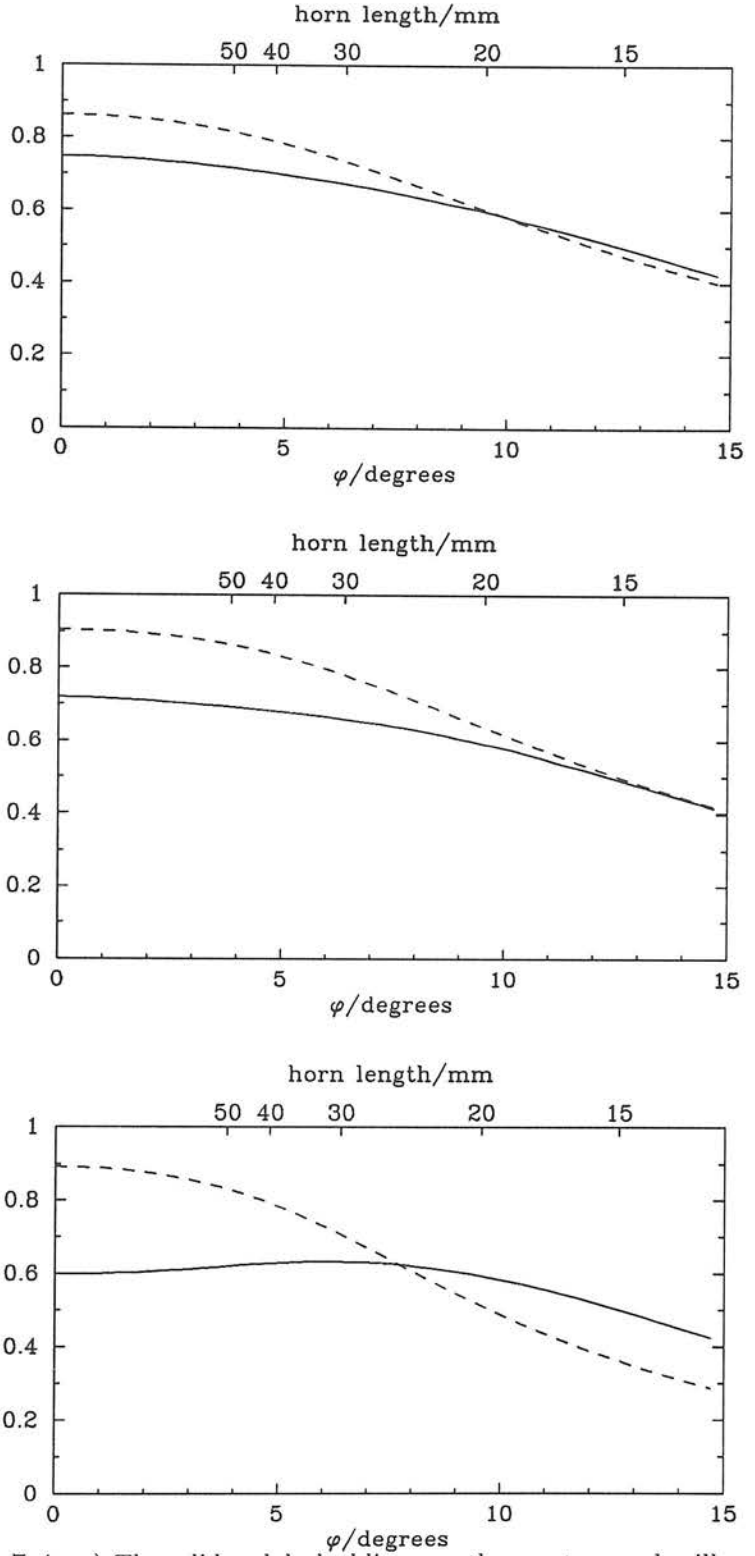

Figure 7.4: a) *The solid and dashed lines are the aperture and spillover efficiency of the* 855 μm *feedhorn.* b) *As in* (a) *but when the horn feeds* 700 μm *radiation.* c) *When the same system feeds* 600 μm *radiation, then both the* TE_{11} *and the* TM_{01} *waveguide modes propagate unattenuated. The advantage of a* 40 mm *length horn over a* 30 mm *one in all three cases is very small.*

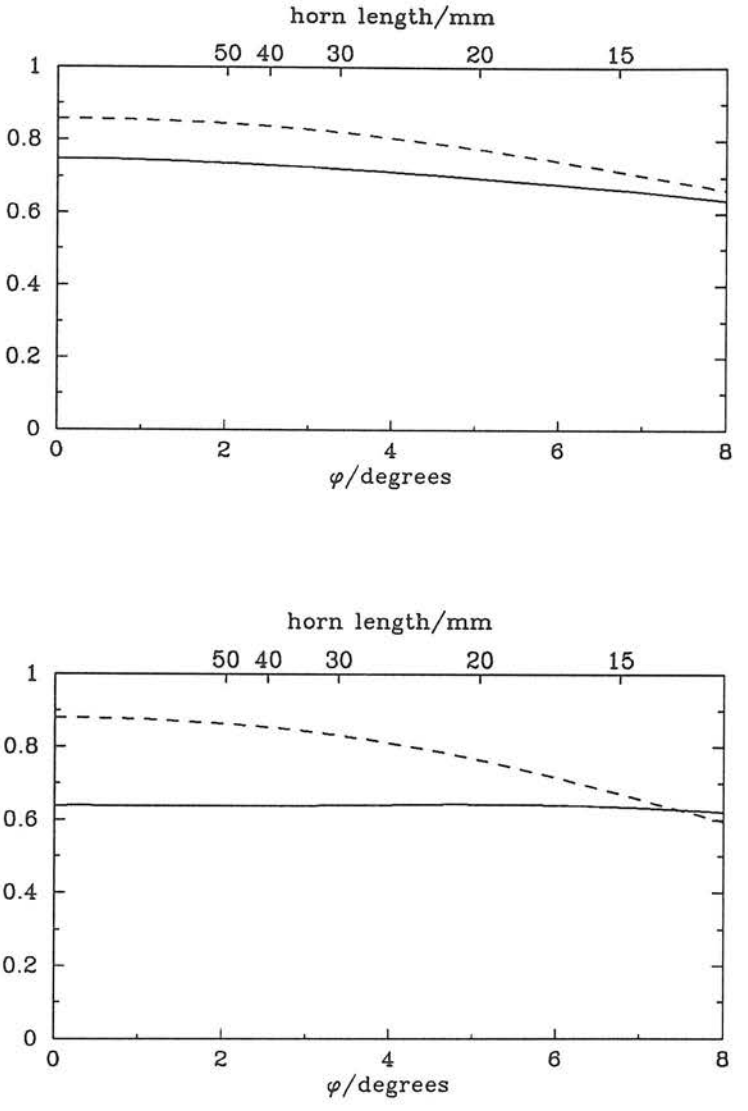

Figure 7.5: a) *The solid and dashed lines are the aperture and spillover efficiency of the* 438 μm *feedhorn.* b) *As in* (a) *but when the horn feeds* 350 μm *radiation. In this case both the* TE_{11} *and the* TM_{01} *waveguide modes propagate unattenuated. The advantage of a* 40 mm *length horn over a* 30 mm *one is very small.*

7.3.2 Ohmic Losses

The philosophy of having high aperture efficiency radiators has the consequence that the horns must be very long and are possibly prone to ohmic loss. When waveguides/horns are bounded by material with a finite conductivity, the fields in the walls are not zero at the boundary, but they drop off to zero exponentially within the wall. Non-zero fields in the walls imply power flow normal to the guide/horn axis and the amount of power lost to this ohmic loss increases exponentially with the length of the device. Another way to understand ohmic loss is within the particle model of light; the radiation is not perfectly 'reflected' by the horn walls.

In order to calculate the amount of power dissipated into the horn walls, Maxwell's equations need to be solved, this time including the electrical conductivity term and the fact that the boundary conditions are non-trivial. This becomes rather complex, but for walls that have finite, but very large conductivity it is possible to get a satisfactory approximation by 'perturbing' the ideal case, following the method described in Jackson [1975] chapter 8.

At the surface between two media the well known boundary conditions impose the restriction that the normal component of the magnetic field, and the tangential component of the electric field are continuous across the boundary. Fields within a perfect conductor are identically zero and solving Maxwell's equations within a circular waveguide (for example) yields the familiar Bessel function radial dependence, with the dimensionless cut off frequency of 1.84118 for the TE_{11} mode. If this is used as the starting point for the case of finite conductivity, the boundary conditions on the magnetic field are now

$$\hat{\mathrm{n}} \cdot \left(\vec{H} - \vec{H}_{\mathrm{c}} \right) = 0,$$

where $\vec{H}_{\mathrm{c}}$ is the magnetic field within the conductor which is non-zero, and $\hat{\mathrm{n}}$ is the normal to the boundary. The first approximation assumes that the tangential electric field on the surface *is* zero while the normal magnetic field is not. The displacement current in this region where the fields are dropping to zero over a finite distance is neglected, which is a recognition that the ohmic current $J = \sigma \mathbf{E}$ dominates the process.

Maxwell's curl equations then take the following form:

$$\vec{\nabla} \times \vec{E} = i\omega\mu\vec{H}, \tag{7.12a}$$

$$\vec{\nabla} \times \vec{H} \simeq \sigma\vec{E}. \tag{7.12b}$$

Changes parallel to the boundary are small, and all the field attenuation occurs over the normal direction, so the $\vec{\nabla}$ operator can be replaced by a derivative along the normal to the boundary. *viz.*

$$\vec{\nabla} \longrightarrow \hat{\mathrm{n}}\frac{\partial}{\partial\xi}.$$

After the usual manipulations of Eqs. 7.12, and implementing the no-magnetic monopoles stipulation ($\vec{\nabla} \cdot \vec{H} = 0$) the $\vec{H}$ field in the conductor is derived.

$$\frac{\partial^2}{\partial\xi^2}\left(\hat{\mathrm{n}} \times \vec{H}\right) = -\frac{i}{\delta^2}\left(\hat{\mathrm{n}} \times \vec{H}\right),$$

to which the solution is

$$\vec{H}_{\mathrm{c}} = \hat{\mathrm{n}} \times \vec{H} = \vec{H}_{\|}e^{-\xi/\delta}\, e^{i\xi/\delta}. \tag{7.13}$$

The skin depth

$$\delta = \sqrt{2/(\mu\omega\sigma)} \tag{7.14}$$

is the distance required for the $\vec{E}$ or $\vec{H}$ field to drop to e^{-1} of its value at the boundary.

Notice that the field in the conductor is given in terms of the tangential component of the $\vec{H}$ field at the boundary. Thus, the fields that are given by the solution to Maxwell's equations bounded by a perfect conductor can be corrected by Eq. 7.13. Going back to Maxwell's equations in the guide/horn, the tangential $\vec{E}$ field at the surface can now be corrected by the normal $\vec{H}$ field given by Eq. 7.13

$$\vec{E}_{\mathrm{c}} = \frac{1}{\sigma}\vec{\nabla} \times \vec{H}_{\mathrm{c}} = \frac{(-1+i)}{\sigma\delta}\left(\hat{\mathrm{n}} \times \left(\hat{\mathrm{n}} \times \vec{H}_{\mathrm{c}}\right)\right) e^{-\xi/\delta}e^{i\xi/\delta} \tag{7.15}$$

The ohmic loss which is the power flow into the wall, at the wall surface ($\xi = 0$) is given by the Poynting vector

$$\frac{dP}{dA} = \Re\left\{\hat{n}\cdot\frac{1}{2}\vec{E}_c\times\vec{H}_c^*\right\} = \frac{1}{2\sigma\delta}\left|\vec{H}_{||}\right|^2. \tag{7.16a}$$

Equation 7.16a is the ohmic loss per area of wall, and for a waveguide device, the wall area is related to the axial coordinate z as follows:

$$\frac{dP}{dz} = \oint a d\theta\, \Re\left\{\hat{n}\cdot\frac{1}{2}\vec{E}_c\times\vec{H}_c^*\right\} = \frac{1}{2\sigma\delta}\oint a d\theta\, \left|\vec{H}_{||}\right|^2. \tag{7.16b}$$

It now remains to determine the ohmic loss along the guide/horn. For a guide of constant cross section (*i.e.* not a horn) the attenuation of power flow is simply given by the imaginary part of the wavenumber in the guide,

$$P = P_0 e^{-2k_{\Im} z}.$$

from which it follows that

$$k_{\Im} = -\frac{1}{2P}\frac{dP}{dz},$$

and for a circular waveguide, incorporating the result of Eq. 7.16b

$$k_{\Im} = \frac{1}{2\sigma\delta P_{nm}}\left[\left(\frac{k_0 a}{\gamma_{nm}}\right)^2 J_{n+1}^2(\gamma_{nm}) + J_n^2(\gamma_{nm})\right] \tag{7.17a}$$

$$P_{nm} = \frac{k_0\omega a^2}{8{\gamma_{nm}}^2}\int\!\!\int_A r d\theta\, dr\, \left[J_{n-1}^2\left(\gamma_{nm}\frac{r}{a}\right) + J_{n+1}^2\left(\gamma_{nm}\frac{r}{a}\right)\right] \tag{7.17b}$$

Equation 7.17a is derived from the magnitude of the tangential component of the $\vec{H}$ field at the guide wall, and Eq. 7.17b is the power flow along the horn axis. All quantities on the right hand side of Eqs. 7.17 are the perfect conductor values, so that k_0 is given by

$$k_0 = (2\pi/\lambda)\sqrt{1-(\gamma_{nm}/\gamma)^2}.$$

The attenuation parameter $k_{\Im}$ derived above is valid at any point along the device, so the power loss can be generalized to horns as in the last section

$$P = P_0 \exp\left(\int_{z_m}^{z_e} -2k_{\Im}\, dz\right).$$

The results show that ohmic losses are negligible. In fact the waveguide length can be increased by a factor of ten without any significant consequences. The conductivity for gold used here is the value for 99.999% gold at $1K$: $\sigma \simeq 5\,\mathrm{G\mho\,m^{-1}}$ [Matula 1979]. Conductivity *increases* with decreasing temperature, but if there are impurities, in particular iron, then the conductivity will *decrease* as temperature decreases.

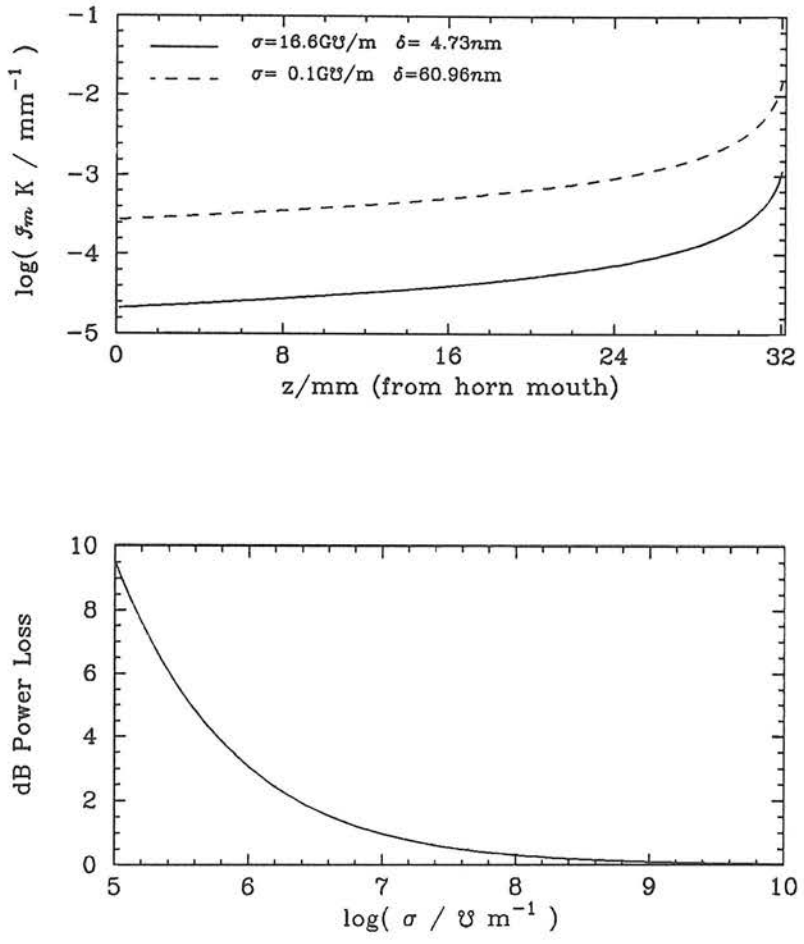

Figure 7.6: *Ohmic losses in the 438 μm horn.* **a)** *The imaginary part of the wavenumber in the horn increases as the horn narrows to the exit.* **b)** *The power loss is related to the integral under the wavenumber curve. For gold with conductivity* ~ 5 G$\Omega\,\mathrm{m}^{-1}$, *the ohmic loss is negligible.*

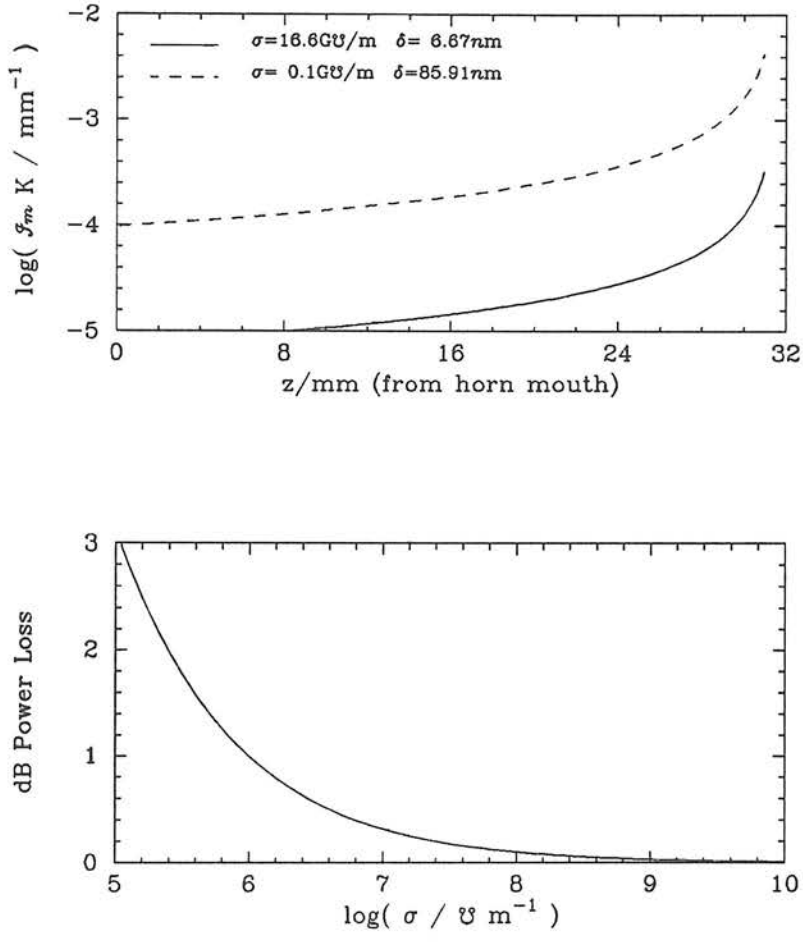

Figure 7.7: *Ohmic losses in the 855 μm horn.* **a)** *The imaginary part of the wavenumber in the horn increases as the horn narrows to the exit.* **b)** *The power loss is related to the integral under the wavenumber curve. For gold with conductivity* ~ 5 GΩ m^{-1}, *the ohmic loss is negligible.*

7.4 Signal Measurement

In order to compute the signal coupled to the antenna by a particular source the spillover and the atmosphere transmission $\mathcal{T}$ must be considered, as well as the aperture efficiency if it is a point source.

$$\begin{aligned} T_{\rm meas} &= \mathcal{T}(\eta'_{\rm B}\eta_{\rm Ap}T'_s + \eta_{\rm B}T_s) \;+\; (1-\mathcal{T})\eta_{\rm B}T_{\rm atm} \;+\; (1-\eta_{\rm B})T_{\rm atm} \\ &= \mathcal{T}(\eta'_{\rm B}\eta_{\rm Ap}T'_s + \eta_{\rm B}T_s) \;+\; (1-\mathcal{T}\eta_{\rm B})T_{\rm atm} \end{aligned} \tag{7.18}$$

where $T_{\rm meas}$ and $T_{\rm atm}$ are the equivalent Rayleigh-Jeans temperatures which is measured by the antenna, and emitted by the atmosphere respectively. T'_s and T_s are the temperatures emitted by the point source and an extended thermal source within the telescope beam. In the first term of Eq. 7.18 the spillover $\eta'_{\rm B}$ is that associated with the part of the horn profile which couples to a point source (*e.g.* column 6 of Table 7.1a for the infinite length horn).

An overmoded feed is most damaging to antenna efficiency because of increased background thermal loading. The Earth's atmosphere and any other black body or near black body source is an emission of random polarized radiation. Instantaneously, the antenna sees, on the average, radiation of any given polarization so each of the supported waveguide modes can couple to equal amounts of power. The spillover in this case is simply the average of those of the modes which propagate in the feed. For the 855 μm feedhorn $\eta_{\rm B} = 0.742$, and when it supports the first two waveguide modes ($\lambda = 623\,\mu$m), $\eta_{\rm B} = (0.832 + 0.607)/2 = 0.72$. The point source spillover is $\eta'_{\rm B} = 0.725$ for the aperture efficiency optimized horn (855 μm) and $\eta'_{\rm B} = 0.803$ in the overmoded case (481 GHz, 623 μm).

A typical calibrating source used from the JCMT might be Jupiter which emits as a point source black body of temperature $\sim$150 K. The Earth's atmosphere is at $\sim$275 K with transmission $\mathcal{T} \simeq 0.40$ at $\lambda = 623\,\mu$m. The first term of Eq. 7.18 gives the source signal measured by the antenna: $0.40 \times 0.803 \times 0.633 \times 150$ K $\simeq 30$ K, and the rest gives the background loading: $(1 - 0.40 \times 0.72) \times 275$ K $\simeq 196$ K. So in a given time t, the detector measures $\sim$226 K of which $\lesssim 13\%$ is signal from Jupiter, and $\gtrsim 87\%$ is background loading.

If the feed used was optimized for this frequency (481 GHz, 623 μm), it would be a single moded device with aperture efficiency of 0.71, spillover efficiency of 0.80, and point source spillover of 0.77. The source signal is now $0.40 \times 0.77 \times 0.71 \times 150$ K $\simeq 33$ K, and the background loading is $(1 - 0.70 \times 0.80) \times 275$ K $\simeq 121$ K. So in this single moded case, Jupiter accounts for $\sim 27\%$ of the flux entering the detector. Comparing the two cases, $(27\%/13\%)^2 = \sim 4$, implies that the integration time on the calibrating source Jupiter (the time required to obtain a given level of detection) is about 4 times longer if the feedhorn supports two waveguide modes.

7.5 Discussion

A further observational ability is added to the receiver when the single mode criteria is sacrificed and a filter drum allows the array to image radiation at its optimized frequency, or at a higher, and possibly overmoded, frequency. The flux from astronomical sources will be measured by SCUBA in five wavebands: 350 GHz (855 μm), 428 GHz (700 μm), 481 GHz (628 μm), 685 GHz (438 μm), and 857 GHz (350 μm). The two bolometer arrays mounted in the instrument are designed to operate with optimum efficiency at 438 μm and 855 μm. At the shorter wavelengths the arrays consist of non-optimized feeds and one must consider the higher order beam modes which are then permitted to propagate in the system.

Efficiencies in the Cassegrain telescope were computed using Gaussian Beam Analysis after first determining the horn $\vec{E}$ field profile using the cylindrical waveguide modes as the "source" functions. The aperture efficiency (point source efficiency) and the beam efficiency (spillover efficiency) were both considered. The Chapter also displayed the dependence of efficiency estimates on the number of L-G modes used in the profile synthesis, as well as the efficiency changes with the number of propagating waveguide modes.

A particular case of the detection of Jupiter as a calibrating source was discussed. The analysis shows that the 855 μm array receiving 600 μm radiation suffers a 5% reduction in aperture efficiency from 68% to 63%, and a 2% loss in beam efficiency from 74% to 72%. This last dominates the reduction in feedhorn performance since the background is normally brighter than the source, and a reduction in spillover efficiency implies increased background loading, in addition to the fact that only one of the propagating

modes is coupling to the point source. In terms of integration times for the example of Jupiter, this means that the telescope must look at a point source for roughly four times the duration when the receiver is overmoded at 600 μm than it would if the antenna feed was optimized at that frequency. For source fluxes which are significantly fainter than that of Jupiter (as most interesting objects are), this difference between single and overmoded optics will become more severe as the background dominates more and more.

Ohmic losses that might occur along such a long guide were considered, and shown to be negligible. The very high expected electrical conductivity of gold at cryogenic temperatures means that the device walls are sufficiently close to a perfect conductor for guided propagation to travel over large distances unmolested. Substantial power dissipation into the horn walls could only have been controlled by reducing the horn length which would then imply large flare angle horns, and re-introduction of the waveguide into the 438 μm feed. There would then be a substantial loss in aperture efficiency, and in manufacturability. It is therefore very important that ohmic losses can safely be disregarded.

Overall, overmoded optics do reduce aperture efficiency as expected. Nonetheless, this may be an acceptable price to pay when a "quick & dirty" scheme for increasing the number of channels is desired on a receiver. In the case of the Submillimetre Common User Bolometer Array, this means the 700 μm, 600 μm and 350 μm channels can be added to the instrument without manufacturing an array of bolometers dedicated to that frequency, and it will operate satisfactorily.

8 The SCUBA Integrating Cavity

When the first bolometer experiments were performed at Queen Mary College (now Queen Mary and Westfield College), the measured power falling on the bolometer was enormously less than expected [Holland 1990]. A number of causes were suspected, one of which was vignetting of the beam as it came through the cryostat windows and subsequent baffles, and this is the one which was eventually proven the culprit. However, a possibility which would have had dire consequences was that radiation was being reflected at the interface between the waveguide and the integrating cavity, or that a standing wave set-up in the resonant cavity implied an acute dependence on bolometer position within the cavity. This is what motivated the analysis presented in this Chapter.

Discontinuities in waveguide lines and networks commonly occur in microwave systems and the analysis of these structures are usually treated using the equivalent circuit [see *e.g.* Marcuvitz 1986]. Often such devices are ports with T-junctions, or L-junctions or other geometries where the feeding guide and the output guides all support the same single waveguide mode. Alternatively, the output guide might be slightly larger, but still supporting only the fundamental mode (TE_{11} for the case of the cylindrical waveguide). These problems are addressed by Marcuvitz.

For the case of a junction between two guides of significantly different cross sections, *and* when it is desired to have the field specification in the receiving guide, one must do a scattering analysis. Fortunately, the problem presented here is fairly straightforward since both guides are circular, and they share the same axial symmetry. The TE_{11} waveguide mode is scattered at the junction into an expanded TE_{11} and higher order TE_{1m} in the integrating cavity.

An important difference between the analysis presented in this Chapter, and a previous investigation of bolometer absorptivity [Peterson & Goldman 1988], is that the

in the opposite direction of the incident wave, *i.e. reflected wave* $= \Gamma_{nm}\left(\vec{E}^{*}_{nm}\ ,\ -\vec{H}^{*}_{nm}\right)$.

At this point, the analysis ignores the bolometer and considers both sides of the junction to be perfectly conducting, infinite cylinders. The azimuthal and time dependence of the modes is everywhere $\exp(in\theta - i\omega t)$. The incident mode is considered to have unit power. Equating the fields at the boundary between the cylinder on the left (denoted by superscript g) and on the right (superscript c) yields the following:

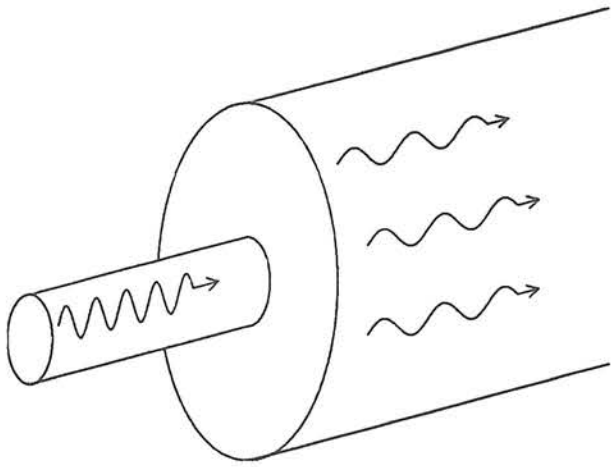

Figure 8.1: *The waveguide leads abruptly into the integrating cavity and the* TE_{11} *waveguide mode from the left-hand-side is scattered through the junction into an expanded* TE_{11} *mode and higher degree* TE_{1m} *modes.*

$$\vec{E}^{(\mathrm{g})}_{11} + \sum_p \sum_q \Gamma_{pq} \vec{E}^{(\mathrm{g})*}_{pq} = \sum_p \sum_q T_{pq} \vec{E}^{(\mathrm{c})}_{pq} \tag{8.1a}$$

$$\vec{H}^{(\mathrm{g})}_{11} - \sum_p \sum_q \Gamma_{pq} \vec{H}^{(\mathrm{g})*}_{pq} = \sum_p \sum_q T_{pq} \vec{H}^{(\mathrm{c})}_{pq} \tag{8.1b}$$

The reflection, and transmission coefficients of the $(nm)^{\mathrm{th}}$ beam mode can be obtained by taking the inner product with the beam modes $\vec{E}^{(\mathrm{g})}_{nm}$ and $\vec{H}^{(\mathrm{g})}_{nm}$. The junction is considered to be at $z = 0$ without loss of generality.

$$\left(\frac{\omega k^{*}_{nm} a^2}{4\mu\gamma^2_{nm}}\right)\left[\delta_{1n}\delta_{1m} + \Gamma_{nm}(P_{nm} - 2I_{nm})\right] = \sum_p \sum_q \left\langle T_{pq}\vec{E}^{(\mathrm{c})}_{pq} \,\middle|\, \vec{H}^{(\mathrm{g})}_{nm} \right\rangle \tag{8.2a}$$

$$\left(\frac{\omega k^{*}_{nm} a^2}{4\mu\gamma^2_{nm}}\right)\left[\delta_{1n}\delta_{1m} - \Gamma_{nm}(P_{nm} - 2I_{nm})\right] = \sum_p \sum_q \left\langle \vec{E}^{(\mathrm{g})}_{nm} \,\middle|\, T_{pq}\vec{H}^{(\mathrm{c})}_{pq} \right\rangle \tag{8.2b}$$

It should be noted that a beam mode can only be scattered to higher modes with identical azimuthal dependance; the inner products in Eqs. 8.2 will vanish otherwise. One can solve for the transmission coefficients:

$$2\left(\frac{\omega k_{1m}^{*} {a_c}^2}{4\gamma_{1m}^2}\right)\delta_{1m} = \sum_q T_{1q}\left[\left\langle \vec{E}_{1q}^{(c)} \,\middle|\, \vec{H}_{1m}^{(g)} \right\rangle + \left\langle \vec{E}_{1m}^{(g)} \,\middle|\, \vec{H}_{1q}^{(c)} \right\rangle\right] \tag{8.3}$$

Equation 8.3 is a matrix equation solveable for the transmission coefficients of the scattered modes.

The dimensionless frequency γ determines the modes which propagate in the guide and the cavity: $\gamma = 2\pi a/\lambda$. For the free-space wavelength $\lambda = 855\,\mu$m, $\gamma_g = 1.95$ in the waveguide and $\gamma_c = 12.936$ in the integrating cavity. Hence in the waveguide only the TE_{11} mode propagates and in the cavity the four modes up to TE_{14} propagate: the higher modes being evanescent (see Table 8.1). Solutions to Eq. 8.3 are given in the second column of Table 8.1.

Table 8.1: Scattering and Absorption of the TE Modes

Mode	γ_{nm}	Power fraction in cavity $\lvert T_{1q}\rvert^2$	Impedance in cavity	Impedance in crystal	Absorbed Power $1-\lvert\mathcal{R}_{1q}\rvert^2$
TE_{11}	1.84118	0.014	$0.9898\mathcal{Z}_0$	$0.3243\mathcal{Z}_0$	0.594
TE_{12}	5.33144	0.260	$0.9111\mathcal{Z}_0$	$0.2985\mathcal{Z}_0$	0.896
TE_{13}	8.53632	0.287	$0.7514\mathcal{Z}_0$	$0.2462\mathcal{Z}_0$	0.027
TE_{14}	11.70600	0.428	$0.4256\mathcal{Z}_0$	$0.1344\mathcal{Z}_0$	0.551
TE_{15}	14.86359	-	-	-	-
totals	-	0.989	-	-	0.484

The inner products of the waveguide modes are written out explicitly:

$$\left\langle \vec{E}_{nm} \,\middle|\, \vec{H}_{pq}^{*} \right\rangle = \delta_{np}\delta_{mq}\left(\frac{\omega k_{nm}^{*} a^2}{4\mu\gamma_{nm}^2}\right)\left[P_{nm} - 2I_{nm}\right] \tag{8.4a}$$

$$\left\langle \vec{E}_{pq}^{*} \,\middle|\, \vec{H}_{nm} \right\rangle = \delta_{np}\delta_{mq}\left(\frac{\omega k_{nm}^{*} a^2}{4\mu\gamma_{nm}^2}\right)\left[P_{nm} - 2I_{nm}\right] \tag{8.4b}$$

$$\left\langle \vec{E}_{pq}^{(c)} \,\middle|\, \vec{H}_{nm}^{(g)} \right\rangle = \delta_{np}\left(\frac{\omega k_{nm}^{(g)*} a_c a_g}{4\mu\gamma_{pq}\gamma_{nm}}\right) II_{mq}^{n} \tag{8.4c}$$

$$\left\langle \vec{E}_{nm}^{(g)} \,\middle|\, \vec{H}_{pq}^{(c)} \right\rangle = \delta_{np} \left(\frac{\omega k_{pq}^{(c)*} a_c a_g}{4\mu\gamma_{pq}\gamma_{nm}} \right) II_{mq}^{n} \tag{8.4d}$$

where,

$$I_{nm} = \int_0^1 \rho \, d\rho \left[J_n'^{\,2} (\gamma_{nm}\rho) \right] \tag{8.4e}$$

$$II_{mq}^{n} = \int_0^1 \rho \, d\rho \left[J_{n-1} (\gamma_{nm}\rho) \, J_{n-1} \left(\gamma_{nq} \frac{a_g}{a_c} \rho \right) + J_{n+1} (\gamma_{nm}\rho) \, J_{n+1} \left(\gamma_{nq} \frac{a_g}{a_c} \rho \right) \right] \tag{8.4f}$$

8.2 Absorption in the Integrating Cavity

Guided waves can be modelled by an equivalent transmission line problem [Marcuvitz 1986, Lesurf 1990] which is the procedure followed by Peterson & Goldman [1988]. In their calculation, the absorbing film within the rectangular cavity is partitioned into $2n$ strips and considered to be a transmission line with $2n$ components ($n \to \infty$). Here, however, the overall impedance of the absorbing film is considered to be a known quantity, equal to the value required for matching the TE_{11} mode.

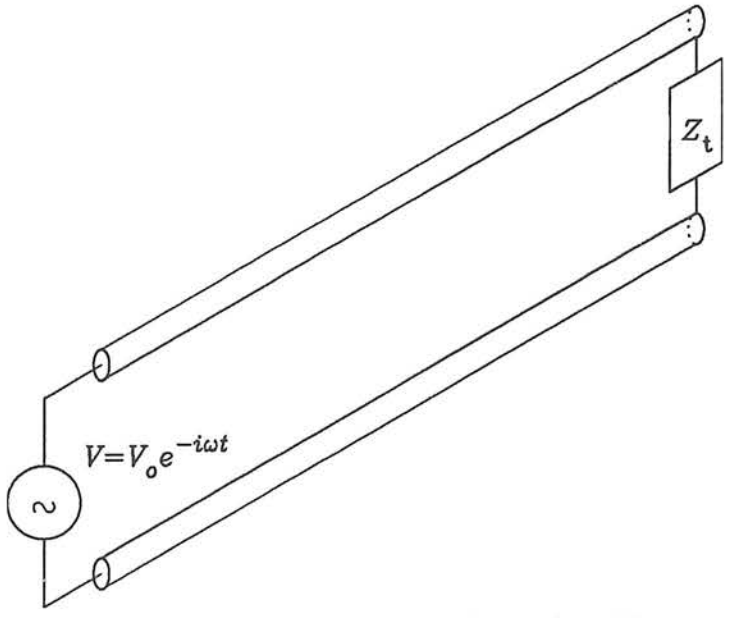

Figure 8.2: *A twin feeder transmission line fed by a voltage V at one end and terminated by an impedance Z_t.*

A 'Twin Feeder' transmission line, as in Figure 8.2, consists of two parallel wires, at one end an input voltage signal is generated of the following form:

$$V = V_0 e^{-i\omega t} \tag{8.5}$$

The result can be considered as a guided wave and everywhere along the transmission line the voltage between the wires is the following:

$$V = V_0 e^{i(kz-\omega t)} \tag{8.6}$$

The current in the wire is determined by Ohm's Law:

$$I = \frac{V}{\mathcal{Z}_{\rm ch}} \tag{8.7}$$

$\mathcal{Z}_{\rm ch}$ is the *characteristic impedance* determined by the wire diameter and material. When modelling a waveguide as a transmission line, $\mathcal{Z}_{\rm ch}$ is the characteristic impedance of the guide:

$$\mathcal{Z}_{\rm ch} = \mathcal{Z}_0 \left[1 - \left(\frac{\gamma_{nm}}{\gamma_{\rm c}}\right)^2\right]^{-\frac{1}{2}} \qquad \text{for TE}_{nm} \text{ modes} \tag{8.8a}$$

$$\mathcal{Z}_{\rm ch} = \mathcal{Z}_0 \left[1 - \left(\frac{\gamma_{nm}}{\gamma_{\rm c}}\right)^2\right]^{\frac{1}{2}} \qquad \text{for TM}_{nm} \text{ modes} \tag{8.8b}$$

and in the crystal substrate of refractive index $n_{\rm r}$:

$$\mathcal{Z}_{\rm b} = \frac{\mathcal{Z}_{\rm ch}}{n_{\rm r}} \tag{8.9}$$

If the transmission line is terminated by some impedance $\mathcal{Z}_{\rm t}$, then a fraction of the signal power is absorbed by the termination, and the rest is reflected back along the transmission line. The reflected mode will be an opposite propagating wave:

$$V_{\rm r} = \mathcal{R}\, V_0\, e^{i(-kz-\omega t)} \tag{8.10}$$

where $\mathcal{R}$ is the reflection coefficient. The current in the transmission line associated with the reflection will be in the opposite direction to the generated signal:

$$I_{\rm r} = -\frac{V_{\rm r}}{\mathcal{Z}_{\rm ch}}. \tag{8.11}$$

The voltage and current across the termination is the sum of the incident and reflected signals:

$$V_t = V_i + V_r \tag{8.12a}$$

$$I_t = I_i + I_r \tag{8.12b}$$

Substituting Eqs. 8.10 and 8.11 into Eqs. 8.12 results in an expression for the reflection coefficient:

$$\mathcal{R} = \frac{\mathcal{Z}_t - \mathcal{Z}_{ch}}{\mathcal{Z}_t + \mathcal{Z}_{ch}} e^{2ikz} \tag{8.13}$$

Some cases of particular interest are when the terminating impedance is nought, very large, or equal to the characteristic impedance. In the first case *all* of the incident signal is reflected and returns with a phase difference of $\pi/2$. If the terminating impedance is infinitely large, or the transmission line is infinitely long, then again all of the incident signal is reflected and returns in phase with the incident. In the final case, the termination is *well matched*; $\mathcal{Z}_t = \mathcal{Z}_{ch}$ and there is *no* reflected wave, which is the desired situation.

A final concept required is the equivalent impedance of a transmission line. The entire line can be simulated by some effective impedance at the signal generator, simply by employing Ohm's Law:

$$\begin{aligned} \mathcal{Z}_{eff} &= \frac{V_i + V_r}{I_i + I_r} \\ &= \mathcal{Z}_c \left(\frac{1 + \mathcal{R}}{1 - \mathcal{R}} \right). \end{aligned} \tag{8.14}$$

Figure 8.3a shows the integrating cavity of the SCUBA feed and Figure 8.3b is the equivalent transmission line. In order to find the reflectivity of the bolometer, the analysis is done in two stages. Firstly, the region between the film and the backshort is replaced by an effective impedance in parallel with the film impedance:

$$\frac{1}{\mathcal{Z}_{f_{eff}}} = \frac{1}{\mathcal{Z}_f} + \frac{i}{\mathcal{Z}_{ch} \tan(k_1 l_1)}. \tag{8.15}$$

Secondly, the region filled by the crystal is replaced by an effective impedance at the crystal-cavity interface (region 2 to region b in Figure 8.3a):

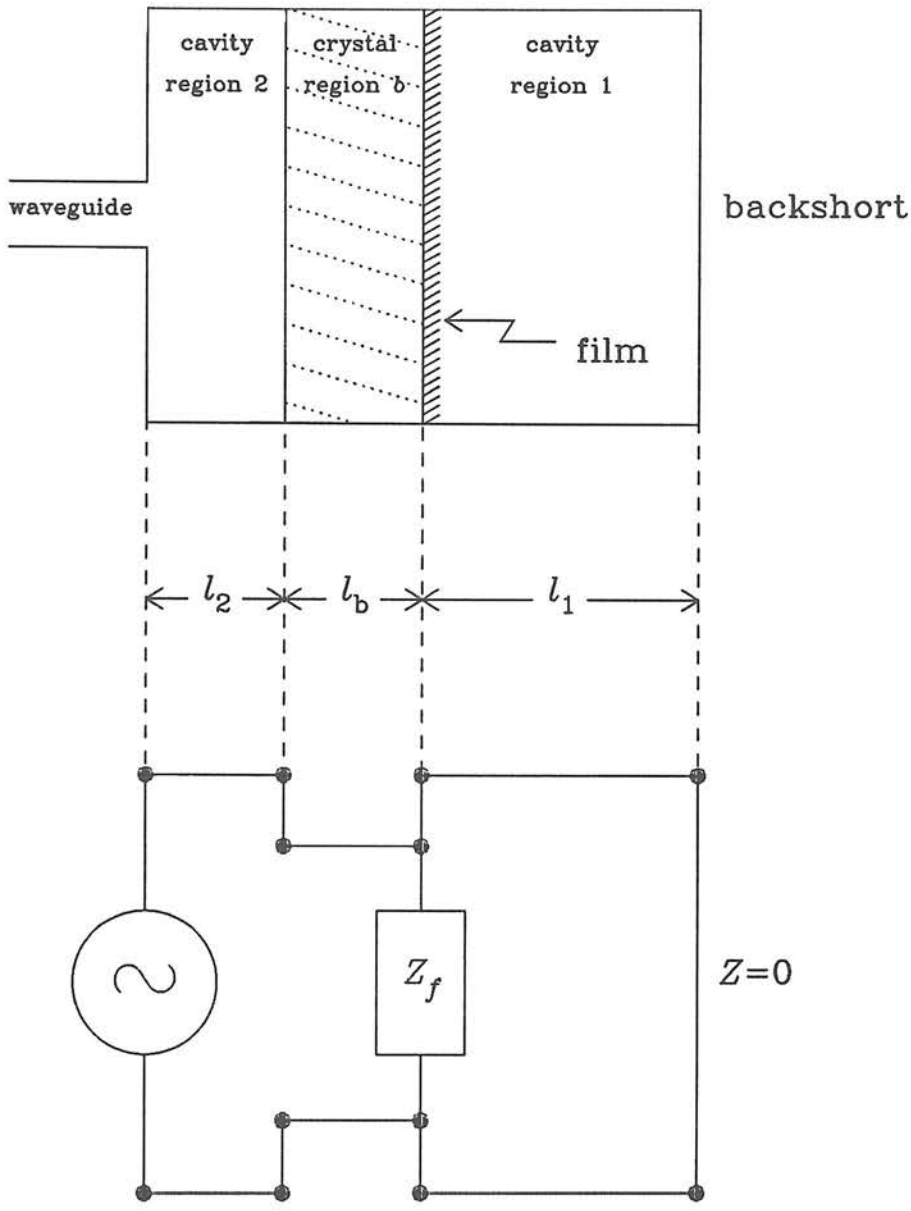

Figure 8.3: a) *The integrating cavity set-up. In Feed I,* $\lambda = 855\,\mu$m *or* $700\,\mu$m, $l_1 = 3.66mm$, $\mathcal{Z}_f = 370.0\Omega$. *In Feed II,* $\lambda = 438\,\mu$m *or* $350\,\mu$m, $l_1 = 3.60mm$, $\mathcal{Z}_f = 369.0\Omega$. *In both cases* $l_b = 30\,\mu$m *and the sapphire refractive index is 3.052.* b) *The equivalent transmission line.*

$$\mathcal{Z}_{\mathrm{b_{eff}}} = \mathcal{Z}_{\mathrm{b}} \left[\frac{\mathcal{Z}_{\mathrm{f_{eff}}} - i\mathcal{Z}_{\mathrm{b}} \tan(k_b l_b)}{-\mathcal{Z}_{\mathrm{f_{eff}}} \tan(k_b l_b) + \mathcal{Z}_{\mathrm{b}}} \right]. \tag{8.16}$$

Finally, we have the reflectivity of the integrating cavity:

$$\mathcal{R} = \frac{\mathcal{Z}_{\mathrm{b_{eff}}} - \mathcal{Z}_{\mathrm{ch}}}{\mathcal{Z}_{\mathrm{b_{eff}}} + \mathcal{Z}_{\mathrm{ch}}} \; \mathrm{e}^{2ik_c l_2}. \tag{8.17}$$

The power in the reflected modes is simply the square of the magnitude of the reflection coefficient. Note that reflectivity of each mode is different, as the characteristic impedance of the cavity and crystal depend on the mode considered. For the TE_{11} at the tuned frequency, the dimensions of cavity components, in particular $\mathcal{Z}_f$ and l_1, are chosen such that $\mathcal{R} = 0$.

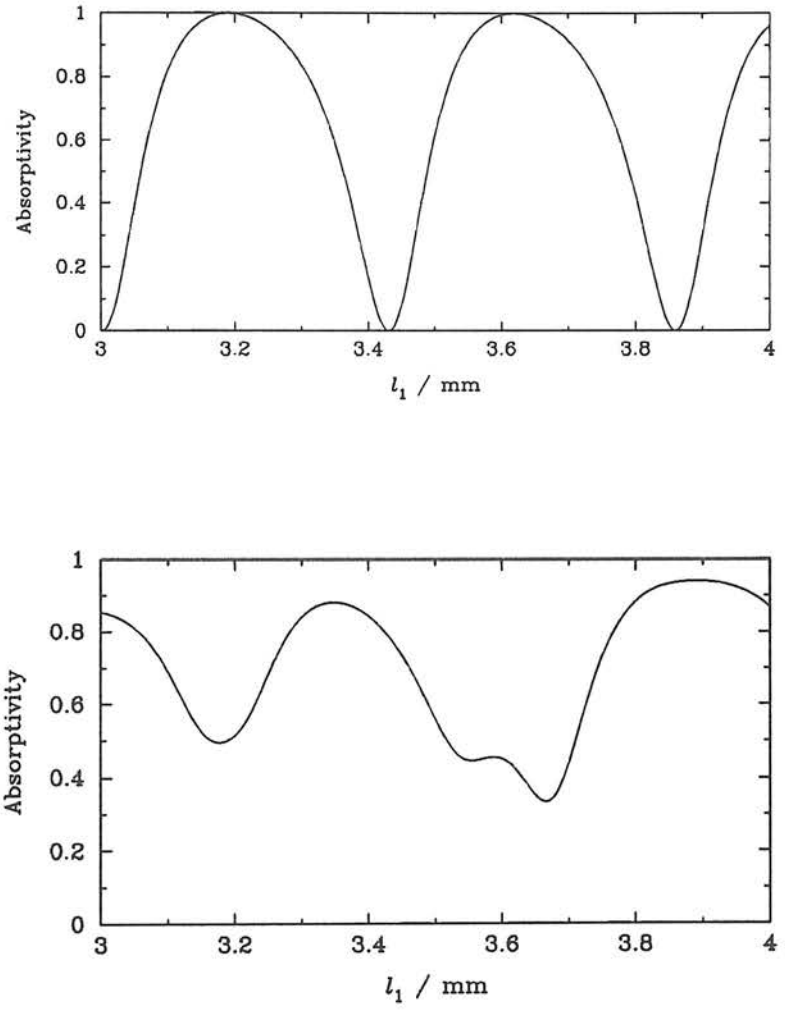

Figure 8.4: a) *The "first pass" absorptivity of the* TE_{11} *mode to the bolometer with the backshort at positions between* 3 mm *and* 4 mm *from the film and with* 855 μm *incident radiation.* b) *The total absorptivity for the sum of the modes that were scattered into the cavity. As can be seen, the worst case and best case in this* 1 mm *interval is* ~40% *and* ~90% *respectively.*

8.3 Discussion

The final consideration for the SCUBA feedhorn design was the behaviour of radiation inside the integrating cavity where it meets the bolometer. This was motivated by initial experiments which showed a very low absorbing efficiency. Although the cause of the poor performance was eventually found to be beam vignetting, still this analysis provided an understanding to the workings of the integrating cavity.

Firstly it was shown that while the incoming radiation is scattered at the junction between guide and cavity, still most of it gets through to the cavity in some form, and very little ($\lesssim 1\%$) is reflected back into the horn. This prediction was verified by later experiments carried out at Queen Mary and Westfield College.

Within the cavity, the "first pass" absorption is modelled as a twinfeeder transmission line problem. Care was taken to include all the modes which exist within the cavity. It is impossible to get close to 100% absorption on the first pass since the various wavemodes require the bolometer to be at different positions for 100% absorption. This would not be the case in a single moded integrating cavity.

Multiple reflections rescue the situation by allowing the bolometer several passes from the radiation, and eventually it is all absorbed. This can be seen as a consequence of the high conductivity of the gold plated integrating cavity; the walls very nearly perfectly reflect the radiation. Therefore, whether the cavity is single moded, or multimoded, it still operates well.

The proposed solution to low bolometer absorption would have been a tapered entrance into the cavity to prevent scattering at the junction, and then an integrating cavity designed specifically to match the TE_{11} wavemode. Positioning the bolometer within the cavity would then be critical to within 0.1 mm: a very difficult task. The lab work performed concurrently at QMW demonstrated that bolometer absorption is very high, but the analysis presented here was undertaken to modify the feedhorn design in case reflections in the cavity did not occur with enough multiplicity.

Summary

9 Summary

Throughout this thesis, a strong emphasis has been placed on the Submillimetre Common User Bolometer Array and the cosmologically orientated experiments it will perform. Simulations of clusters as gravitational lenses show that small scale distortions to the CBR can be amplified to fill larger beam sizes. This effect will be of the same order of magnitude as the S-Z microwave increment at the Wien end of the CBR. Chapter 4 described an attempt to detect the dusty primeval galaxies through the lensing cluster Cl 2244 using the present bolometer system on the JCMT. Finally, work on SCUBA itself was presented in Part II in which the importance of high aperture efficiency, and low background loading through single moded optics was emphasized in the design of the feedhorn antennas. CBR experiments such as the one simulated and then attempted during the course of this thesis are major motivators for building a bolometer array such as SCUBA.

The Microwave Background through Clusters

Based on the mass potential approach of Kochanek & Blandford [1987], a model for gravitational lensing by galaxy clusters was derived, and qualitatively compared to the work of Grossman & Narayan [1989] who successfully simulated the observed optical luminous arcs. Models of the clusters Abell 370 and Cl 2244 show that a random field of fluctuations at a redshift of $z = 10$ is spead out into larger area blobs near the cluster centre, and into arcs at further distances up to the region of the characteristic radius. Distortions in the CBR on the scale of $\sim 5'' - 10''$ can be amplified into beams that are a few times larger.

The motivation for a submillimetre background comes from the models of galaxy formation in which the primeval galaxies form, and undergo a burst of star formation leaving the next generation of stars enveloped in dust. The dust re-radiates thermally at

about 40 K the emission from the stars within. One can then construct a submillimetre sky composed of a bumpy background of thermal emitters of temperature ~5 K if the primeval galaxies are presumed to be at a redshift of ~10. The simple model of a Gaussian power spectrum to simulate the submillimetre background was ~~guaged~~ gauged against the detailed models of Bond *et al.* [1986, 1990]. The fluctuations are predominantly on the $\sim 5'' - 10''$ scale, and the maximum amplitude is strictly constrained by the spectral smoothness of the CBR as measured by COBE.

With the S-Z experiment becoming feasible at the Wien frequencies of the CBR, it is a significant result in Chapter 3 that care must be taken when measuring the Microwave Increment. Even the relatively small distortion amplitude due to dusty primeval galaxies would be amplified sufficiently to be within the same order of magnitude as the S-Z distortion. This is especially true of the established lensing clusters, but the gravitational lens effect will also play a part in other clusters, including S-Z candidate clusters. The estimate of H_0 will be erroneously effected if it is based solely on the measured microwave increment without taking into account other distortions to the CBR.

JCMT Observation of Cl 2244–02

Chapter 4 described a deep photometry experiment using the present bolometer system on JCMT. With UKT14, an attempt was made to detect the 850 μm flux towards the cluster Cl 2244. Before the publication of COBE's results, one could expect as much as 100 mJy flux from the gravitationally lensed submillimetre excess based on the rocket borne measurements of Matsumoto *et al.* [1988]. Based on the results of Chapter 3 which carefully took account of the COBE measurement, this expected flux was re-evaluated to ~5 mJy. UKT14 would require approximately nine observing shifts with good weather, however, the two shifts of 27-28 June, 1990 did produce a noise level of 11.6 mJy after sky subtraction (*i.e.* a flux differential of 11.6 mJy). The 1.7σ 'detection' corresponded to an upper limit on anisotropy of $\Delta T/T < 4.6 \times 10^{-3}$, at 850 μm and, when gravitational lensing is considered, the angular scale was ~5″.

Feedhorn Design for SCUBA

The technical aspects of SCUBA were the subject of the three Chapters in Part II which presented analyses for the design of the feedhorn antennas, waveguides, and inte-

grating cavities. The main motivation for a submillimetre camera is possibly for searches of protostars which are the embedded point sources that studies in star formation are desperate to uncover [see *e.g.* Moore 1989, Chandler 1990]. For this reason, high aperture efficiency was deemed a priority in designing the SCUBA horns. The SCUBA horns will also have excellent spillover efficiency, which is important for all types of observations, including those of extended regions of thermal emission, such as from the CBR.

The design of the feedhorn for the Submillimetre Common User Bolometer Array has therefore been undertaken within the confines of the following criteria: high aperture efficiency, minimal background loading, and ease of manufacture. Aperture efficiency is optimized by having a horn with mouth radius $a_m = F\lambda$ and with a small flare angle in order to have the beam phase centre near to the horn mouth. Background loading can be controlled by designing into the feed the ability to "pick out" the desired signal. For point source observations this is achieved through single moded optics, while observations of extended thermal sources also benefit because of the relatively high beam efficiency associated with single moded devices. The horns for the SCUBA array number 128, and although corrugated devices can possibly be manufactured to the small dimensions required for submillimetre feedhorn, the cost and time required to make such a large quantity is prohibitive. Therefore, for aperture efficiency, minimal background loading, and ease of manufacture, the SCUBA horns are very long, single moded conical horns.

In order to preserve the single moded integrity of the system it was shown in Chapter 6 that this can be achieved in some cases without the use of a waveguide component. This was submitted as a possible solution to the difficulty experienced in initial attempts to manufacture the feedhorns. The significant cost saving was weighed against the demand on manpower to the ROE workshop, and it was decided to contract out the horn manufacture to a specialist workshop. Their high RPM CNC lathe will make the manufacture of the tiny waveguide components less problematic, so horns with wider exit apertures and with waveguides will be used which allow for a wider bandpass.

The systems were also analysed to quantify their behaviour when receiving non-optimum frequencies of radiation. In the 700 μm case, the system is still single moded, although the aperture efficiency is not optimized. It was shown how overmodedness degrades the sensitivity of the receiver in the 600 μm and the 350 μm cases.

Finally, the SCUBA integrating cavity was investigated. A scattering analysis was done to show that virtually all the radiation survives the step junction between the waveguide and integrating cavity. Next, a transmission line model of the bolometer response to all the modes present in the cavity showed that 100% absorption is not possible in a multimoded system if one must rely on the tuning of a standing wave. Nonetheless, multiple reflections in the integrating cavity allow for nearly 100% absorption. The analysis was instructive in showing that the number and form of the propagating modes is an important consideration in a tuned cavity.

The SCUBA Project will have the horns fabricated by an outside contractor according to the specifications derived in Part II.

Future Cosmology Experiments with SCUBA

In addition to the S-Z and the primeval galaxy experiments discussed in this thesis, SCUBA will also be capable of further microwave background related observations. Two other distortions can occur to the CBR which rely on gravitational lensing. Both of these effects are powerful diagnostics in cosmology, with the transverse velocity of clusters of galaxies as one direct observable, and the existence of a cosmic string as the other.

It is fairly straightforward to show that a lens passing transversely across an observer's line of sight in front of a uniform blackbody background will cause an apparent distortion to the background with a particular signature. Photons that pass in front of the lens receive a kick, while those interacting with the retreating lens suffer a drag. In the first case the energy of the photons is increased and in the second decreased. The result is a bi-modal discontinuity in the uniform background with an amplitude directly proportional to the velocity of the lens. Thus, with a cluster of galaxies as the gravitational lens and the CBR as the uniform background, the transverse velocity of the cluster is measurable [Birkinshaw & Gull 1983].

Some models of galaxy formation require the existence of cosmic strings which provide the needed perturbations in the primordial density field around which matter can condense into stars and galaxies. To date, only circumstantial evidence exists in favour of a cosmic string. A relatively small sized field with a large number of twin galaxies

suggests a cosmic string, albeit a highly twisted one, at a redshift of $z = 0.07$ [Cowie & Hu 1987]. Verification of this cosmic string is possible in a submillimetre experiment. Once again, using the CBR, the cosmic string which is massive and expected to vibrate at nearly the speed of light, will cause a step discontinuity in the CBR that is directly a map of the string [Kaiser & Stebbins 1984]. SCUBA is particularly suited to this experiment since it will have the mapping capability peculiar to an array instrument.

Final Remarks

The emphasis of this thesis has been on cosmology experiments using a submillimeter continuum array receiver. Firstly, simulations of a submillimetre background due to dusty primeval galaxies were presented, along with the observations that would result when gravitational lensing by clusters of galaxies is considered. The experiment was tried with the single pixel bolometer system on the JCMT, and it was recognized that in the near future, SCUBA, with its more sensitive detectors would be capable of successfully carrying out this experiment. Finally, the extensive design considerations of the feedhorn antennas, and the bolometer integrating cavities were carried out.

References

Andernach, H., Schallwich, D., Sholomitski, G.B., Wielebinski, R., "A search for microwave background diminution towards the cluster 0016+16," *Astron. Astrophys.*, **vol. 124**, pp. 326-330, 1983

Arp, H.C., Burbidge, G., Hoyle, F., Norlikar, J.V., Wickramasinghe, N.C., "The Extra-Galactic Universe: An Alternative View," *Nature*, **vol. 346**, pp. 807-12, August 1990

Balanis, C.A., *Antenna Theory*, Harper & Row, 1982

Barrow W.L., "Transmission of electromagnetic waves in hollow tubes of metal," *Proc. IRE*, **vol. 24**, pp. 1298-1328, October 1936

Belland, P., Crenn, J.P., "Matching of a Gaussian Beam into Hollow Oversized Circular Waveguides," *Int. J. IR & MM Waves*, **vol. 10**, pp. 1279-87, October 1989

Berthon, A., Bills, R.P., "Integral Equation Analysis of Radiating Structures of Revolution," *IEEE Trans. Antennas & Propagation*, **vol. 37**, pp. 159-170, February 1989

Birkinshaw, M., Gull, S.F., Northover, K.J.E., "Measurements of the gas contents of clusters of galaxies by observations of the background radiation at 10.6 GHz," *Mon. Not. R. astr. Soc.*, **vol. 185**, pp. 245-62, 1978

Birkinshaw, M., "Limits to the value of the Hubble constant deduced from observations of galaxies," *Mon. Not. R. astr. Soc.*, **vol. 187**, pp. 847-62, 1979

Birkinshaw, M., Gull, S.F., Northover, K.J.E., "Measurements of the gas contents of clusters of galaxies by observations of the background radiation at 10.6 GHz - II," *Mon. Not. R. astr. Soc.*, **vol. 197**, pp. 571-92, 1981

Birkinshaw, M., Gull, S.F., Moffet, A.T., "Observations of a Decrement in the Microwave Background Radiation toward the distant Cluster of Galaxies 0016+16," *Astrophys. J.*, **vol. 251**, pp. L69-L73, December 1981

Birkinshaw, M., Gull, S.F., "A test for transverse motions of clusters of galaxies," *Nature*, **vol. 302**, pp. 315-17, March 1983

Birkinshaw, M., Gull, S.F., "Measurements of the gas contents of clusters of galaxies by observations of the background radiation at 10.6 GHz - III," *Mon. Not. R. astr. Soc.*, **vol. 206**, pp. 359-75, 1984

Birkinshaw, M., Gull, S.F., Hardebeck, H., "The Sunyaev-Zeldovich effect towards three clusters of galaxies," *Nature*, **vol. 309**, pp. 34-35, May 1984

Blandford, R.D., Kochanek, C.S., in *Dark Matter in the Universe,* **vol. 4,** eds. Bahcall, J., Piran, T., and Weinberg, S., World Scientific Pub. Co., Inc., Jerusalem 30 Dec. 1986 - 8 Jan. 1987

Blandford, R.D., Kochanek, C.S., "Gravitational Imaging by Isolated Elliptical Potential Wells. I. Cross Sections," *Astrophys. J.,* **vol. 321,** pp. 658-675, October 1987

Blume, S., Grafmüller, B., "Biconical Antennas and Conical Horns with Elliptic Cross Section," *IEEE Trans. Antennas & Propagation,* **vol. 36,** pp. 1066-1077, August 1988

Blumenthal, G.R., Faber, S.M., Primack, J.R., Rees, M.J., "Formation of galaxies and large scale structure with cold dark matter," *Nature,* **vol. 311,** pp. 517-525, October 1984

Bond, J.R., Carr, B.J., Hogan, C.J., "Spectrum and Anisotropy of the Cosmic Infrared Background," *Astrophys. J.,* **vol. 306,** pp. 428-450, 1986

Bond, J.R., "Distortions and Anisotropies of the Cosmic Background Radiation," in *The Early Universe,* W.G. Unruh & G.W. Semenoff eds., NATO ASI Series C, **vol. 219,** pp. 283-333, D. Reidel Publishing 1988

Bond, J.R., Carr, B.J., Hogan, C.J., "Cosmic Backgrounds from Primeval Dust," CITA preprint 1990, *Astrophys. J.* in press 1991

Bourassa, R.R., Kantowski, R., Norton, T.D., "The Spheroidal Gravitational Lens," *Astrophys. J.,* **vol. 185,** pp. 747, 1973

Bourassa, R.R., Kantowski, R., "The Theory of Transparent Gravitational Lenses," *Astrophys. J.,* **vol. 195,** pp. 13-21, January 1975

Bondyopadhyay, P.K., and reply by W.E. Gordon, "Comments on 'A Hundred Years of Radio Propagation'," *IEEE Trans. Antennas & Propagation,* **vol. 38,** pp. 1723-26, October 1990

Brittain, J.E., "The Evolution of the Electrical and Electronics Engineering and the Proceedings of the IRE: 1913-1937," *Proc. IEEE,* **vol. 77,** pp. 837-856, June 1989

Cavaliere, A., Fusco-Femiano, R., "X-rays from Hot Plasma in Clusters of Galaxies," *Astron. Astrophys.,* **vol. 49,** pp. 137-44, 1976

Cavaliere, A., Danese, L., de Zotti, G., "Unborn Clusters," *Astrophys. J.,* **vol. 217,** pp. 6-15, October 1977

Cavaliere, A., Danese, L., de Zotti, G., "Cosmic Distances from X-ray and Microwave Observations of Clusters of Galaxies," *Astron. Astrophys.,* **vol. 75,** pp. 322-5, 1979

Cecchini, R., Pelosi, G., "Diffraction: The First Recorded Observation," *IEEE Ant. & Prop. Soc. Mag.,* **vol. 32,** pp. 27-30, April 1990

Chandler, C.J., *A Study of Candidate Protostars,* Ph.D. Thesis, University of Edinburgh, 1990

Church, S.E., *PhD Thesis* University of Cambridge

Clarricoats, P.J.B., Olver, A.D., *Corrugated Horns for Microwave Antennas,* IEE EM Series No. 18, Peter Peregrinus Ltd. on behalf of IEE, 1984

Collins, C.A., Nichol, R.C., Lumsden, S.L., "The Edinburgh/Durham Southern Galaxy Catalogue – III: The Angular Correlation Function from the Full Survey," *Mon. Not. r. Astr. Soc.*, in press 1991

Cowie, L.L., Hu, E.M., "The Formation of Families of Twin Galaxies by String Loops," *Astrophys. J.*, **vol. 318**, pp. L33-L38, July 1987

Crenn, J.P., "Optical theory of Gaussian beam transmission through a hollow circular dielectric waveguide," *Appl. Opt.*, **vol. 21**, pp. 4533-41, December 1982

Crenn, J.P., "Gaussian beam transmission through circular waveguides with conducting wall material," *Appl. Opt.*, **vol. 24**, pp. 3648-58, November 1985

Christiansen, W.N., Högbom, J.A., *Radiotelescopes,* Cambridge University Press, 1985

Cunningham, C.R., Gear, W.K., "The Submillimetre Common User Bolometer Array," *Proc. of SPIE Symp. Astronomical Telescopes & Instrumentation,* February 1990

Dicke, R.H., Peebles, P.J.E., Roll, P.G., Wilkinson, D.T., "Cosmic Black-Body Radiation," *Astrophys. J.*, **vol. 142**, pp. 414-419, 1965

Duncan, W.D., Robson, E.I., Ade, P.A.R., Griffin, M.J., Sandell, G., "A millimetre/submillimetre common user photometer for the James Clerk Maxwell Telescope," *Mon. Not. R. astr. Soc.*, **vol. 243**, pp. 126-132, March 1990

Einstein, A., "Lens-Like Action of a Star by the Deviation of Light in the Gravitational Field," *Science,* **vol. 84**, pp. 506-7, December 1936

Elias, J.H., Ennis, D.J., Gezari, D.Y., Hauser, M.G., Houck, J.R., Lo, K.Y., Matthews, K., Nadeau, D., Neugebauer, G., Werner, M.W., Westbrook, W.E., "1 Millimeter Continuum Observations of Extragalactic Objects," *Astrophys. J.*, **vol. 220**, pp. 25-41, 1978

Fort, B., Prieur, J.L., Mathez, G., Mellier, Y., Soucail, G., "Faint distorted structures in the core of A370: Are they gravitationally lensed galaxies at $z \simeq 1$?," *Astron. Astrophys.*, **vol. 200**, pp. L17-L20, 1988

Fort, B., "Clusters of Galaxies: A New Observable Class of Gravitational Lenses," in *Gravitational Lensing,* Y. Mellier, B. Fort, G. Soucail, eds., pp. 221-9, Springer-Verlag, 1990

Gamow, G., "The Evolution of the Universe," *Nature,* **vol. 162**, pp. 680-682, October 1948

Gear, W.K., Ade, P.A.R., Griffin, M., Duncan, W.D., Joseph, R.D., Hough, J.H., Robson, E.I., Murphy, J.A., *The Submillimetre Common User Bolometer Array,* "The Blue Book," unpublished, 1986, available on request from the Royal Observatory, Edinburgh, Blackford Hill, Scotland, EH9 3HJ

Goldsmith, P.F., "Quasi-optical Techniques at Millimetre and Submillimetre Wavelengths," *Infrared and Millimetre Waves,* **vol. 6**, pp. 277-343, New York: Academic, 1982

Gordon, W.E., "A Hundred Years of Radio Propagation," *IEEE Trans. Antennas & Propagation*, **vol. 33**, pp. 126-130, February 1985

Grossman, S.A., Narayan, R., "Arcs from Gravitational Lensing," *Astrophys. J.*, **vol. 324**, pp. L37-L41, January 1988

Grossman, S.A., Narayan, R., "Gravitationally Lensed Images in Abell 370," *Astrophys. J.*, **vol. 344**, pp. 637-644, September 1989

Gulkis, S., Lubin, P.M., Meyer, S.S., Silverberg, R.F., "The Cosmic Background Explorer," *Sci. Am.*, pp. 122-129, January 1990

Gunn, J.E., in *Observational Cosmology*, eds. Maeder, A., Martinet, L., Tammann, G., Geneva Observatory, April 1978

Guth, A., "Inflationary universe: A possible solution to the horizon and flatness problems," *Phys. Rev. D*, **vol. 23**, pp. 347-356, January 1981

Harper, D.A., Hildebrand, R.H., Stiening, R., Winston, R., "Heat Trap: An Optimized Far Infrared Field Optics System," *Appl. Opt.*, **vol. 15**, pp. 53-60, January 1976

Henry, J.P., Lavery, R.J., "Multiaperture Spectroscopy of Galaxies in Abell 370," *Astrophys. J.*, **vol. 323**, pp. 473-9, December 1987

Holland, W.S., *PhD. Thesis*, Queen Mary and Westfield College, 1990

Jackson, J.D., *Classical Electrodynamics*, John Wiley & Sons, 1975

Jaffe, D.T., Becklin, E.E., Hildebrand, R.H., "Submillimeter Continuum Observations of M82," *Astrophys. J.*, **vol. 285**, pp. L31-L34, 1984

Jones, C., Forman, W., "The Structure of Galaxies Observed with *Einstein*," *Astrophys. J.*, **vol. 276**, pp. 38, January 1984

Jull, E.V., *Aperture Antennas and Diffraction Theory*, IEE EM Series No. 10, Peter Peregrinus Ltd. on behalf of IEE, 1981

Kaiser, N., Stebbins, A., "Microwave anisotropy due to cosmic strings," *Nature*, **vol. 310**, pp. 391-3, August 1984

King, A.P., "The Radiation Characteristics of Conical Horn Antennas," *Proc. IRE*, **vol. 38**, pp. 249-51, March 1950

Klein, U., Wielebinski, R., Morsi, H.W., "Radio continuum observations of M82," *Astron. Astrophys.*, **vol. 190**, pp. 41-46, 1988

Kochanek, C.S., Blandford, R.D., "Gravitational Imaging by Isolated Elliptical Potential Wells. II. Probability Distributions," *Astrophys. J.*, **vol. 321**, pp. 676-685, October 1987

Kogelnik, H., Li, T., "Laser Beams and Resonators," *Proc. IEEE*, **vol. 54**, pp. 1312-29, October 1966

Kolb, E., Turner, E., *The Early Universe,* Addison Wesley, 1990

Kompaneets, A.S., *J. Exp. Theor. Phys.*, **vol 31,** pg. 876, 1956

Koo, D.C., "Multicolor Photometry of the Red Cluster 0016+16 at $z = 0.54$," *Astrophys. J.*, **vol. 251**, pp. L75-L79, December 1981

Kreysa, E., Chini, A., *Proc. 3rd ESO-CERN Symp. on Astronomy, Cosmology and Fundamental Particles,* Bologna, 1988

Kreysa, E., Chini, A., *Proc. Particle Astrophysics Workshop,* Berkeley, 1989

Kristian, J., Sandage, A., Westphal, J.A., "The Extension of the Hubble Diagram. II. First Indication of a Deviation of the Hubble Diagram from a Straight Line," *Astrophys. J.*, **vol. 221**, pp. 383-394, April 1978

Lavery, R.J., Henry, J.P., "Two Blue Arcs Associated with the cD Galaxy of Abell 963," *Astrophys. J.*, **vol. 329**, pp. L21-L24, 1988

Lesurf, J.C.G., *Millimetre-Wave Optics, Devices and Systems,* IOP Publishing ltd., 1990

Love, A.W. ed., *Electromagnetic Horn Antennas,* IEEE Press, 1976

Ludwig, A.C., "Radiation Pattern Synthesis for Circular Aperture Horn Antennas," *IEEE Trans. Antennas & Propagation,* **vol. 14**, pp. 434-40, July 1966

Lynds, R., Petrosian, V., "Giant Luminous Arcs in Galaxy Clusters," *Bull. Amer. Astron. Soc.*, **vol 336,** pg. 1014, 1986

Lynds, R., Petrosian, V., "Luminous Arcs in Clusters of Galaxies," *Astrophys. J.*, **vol. 336**, pp. 1-8, January 1989

Maddox, S.J., Efstathiou, G., Sutherland, W.J., Loveday, J., "Galaxy correlations on large scales," *Mon. Not. R. astr. Soc.*, **vol. 242**, pp. 43p-47p, January 1990

Mahmoud, S.F., "Mode conversion on profiled corrugated conical horns," *IEE Proc. part H,* **vol. 130**, pp. 415-19, October 1983

Marcuse, D., *Light Transmission Optics,* Van Nostrand Reinholt, 1972

Marcuvitz, N., *Waveguide Handbook,* Peter Peregrinus Ltd. on behalf of IEE, 1986

Martin, D.H., Lesurf, J., "Submillimetre Wave Optics," *Infrared Physics,* **vol. 18**, pp. 405-412, 1978

Mather, J.C., "The Cosmic Background Explorer (COBE)," *Opt. Eng.*, **vol. 21**, pp. 769-774, July/August 1982

Mather, J.C., Cheng, E.S., Eplee, R.E.Jr., Isaacman, R.B., Meyer, S.S., Shafer, R.A., Weiss, R., Wright, E.L., Bennett, C.L., Boggess, N.W., Dwek, E., Gulkis, S., Hauser, M.G., Janssen, M., Kelsall, T., Lubin, P.M., Moseley, S.H.Jr., Murdock, T.L., Silverberg, R.F., Smoot, G.F., Wilkinson, D.T., "A Preliminary Measurement of the Cosmic Microwave Background Spectrum by the Cosmic Background Explorer (COBE) Satellite," *Astrophys. J.*, **vol. 354**, pp. L37-L40, May 1990

Matsumoto, T., Hayakawa, S., Matsuo, H., Murakami, H., Sato, S., Lange, A.E., Richards, P.L., "The Submillimeter Spectrum of the Cosmic Background Radiation," *Astrophys. J.*, **vol. 329**, pp. 567-571, June 1988

Matula, R.A., "Electrical Resistivity of Copper, Gold, Palladium, and Silver," *J.Phys.Chem.*, **vol. 8**, pp. 1147-1297, 1979

Merritt, D., "The Distribution of Dark Matter in the Coma Cluster," *Astrophys. J.*, **vol. 313**, pp. 121-135, February 1987

Moore, T.J.T., *Ph.D. Thesis*, University of Edinburgh, 1989

Murphy, J.A., "Aperture Efficiencies of Large Axisymmetric Reflector Antennas Fed by Conical Horns," *IEEE Trans. Antennas & Propagation*, **vol. 36**, pp. 570-575, April 1988

Murphy, J.A., Padman, R., "Radiation patterns of few-moded norns and condensing lightpipes," *Infrared Physics*, **vol. 31**, pp. 291-9, 1991

Mushotzky, R.F., "X-ray Emission from Clusters of Galaxies," *Phys. Scripta*, **vol. T7**, pp. 157-162, 1984

NAG, *The NAG Fortran Library*, Numerical Algorithms Group ltd., 1990, ISBN 1-85206-054-9

Nahin, P.J., "Oliver Heaviside," *Sci. Am.*, **vol. 262**, pp. 122-9, June 1990

Narasimhan, M.S., Govind, K.R., "Radiation Characteristics of a Corrugated Circular Cylindrical Waveguide Horn Excited in the TE_{11} Mode," *IEEE Trans. Antennas & Propagation*, **vol. 36**, pp. 1147-1152, August 1988

Narayan, R., Blandford, R.D., Nityananda, R., "Multiple imaging of quasars by galaxies and clusters," *Nature*, **vol. 310**, pp. 112-115, July 1984

Olver, A.D., Jun Xiang, "Design of Profiled Corrugated Horns," *IEEE Trans. Antennas & Propagation*, **vol. 36**, pp. 936-940, July 1988

Padman, R., Murphy, J.A., Hills, R.E., "Gaussian Mode Analysis of Cassegrain Antenna Efficiency," *IEEE Trans. Antennas & Propagation*, **vol. 35**, pp. 1093-1103, 1987

Partridge, R.B., "A Search for Primeval Galaxies at High Redshifts," *Astrophys. J.*, **vol. 192**, pp. 241-9, September 1974

Payne, J.M., "Millimeter and Submillimeter Wavelength Radio Astronomy," *Proc. IEEE*, **vol. 77**, pp. 993-1017, July 1989

Peacock, J.A., "The Power Spectrum of Galaxy Clustering," submitted to *Nature* 1991

Peterson, J.B., Goldman, M.A., "Reflectance of Broad Band Waveguide Bolometers," *Int. J. IR & MM Waves,* **vol. 9**, pp. 55-69, January 1988

Peterson, J.B., "Millimeter and Sub-millimeter Photometry from Antarctica," *preprint,*1989

Petrosian, V., "Arcs in Clusters of Galaxies as Gravitational Lens Images," in *Gravitational Lenses,* J.P. Moran, J.N. Hewitt, K.Y. Lo, eds., pp. 109-26, Springer-Verlag, 1989

Petrosian, V., Bergmann, A.G., Lynds, R., "Lens and Source Models for Arcs in Cluster Abell 370 and Cl 2244," in *Gravitational Lensing,* Y. Mellier, B. Fort, G. Soucail, eds., pp. 254-60, Springer-Verlag, 1990

Penzias, A.A., Wilson, R.W., "A Measurement of Excess Antenna Temperature at 4080 Mc/s," *Astrophys. J.,* **vol. 142**, pp. 419-421, 1965

Puxley, P.J. *Vigorous Star Formation In Galactic Nuclei,* Ph.D. Thesis, University of Edinburgh, 16 November, 1988

Rabl, A., Winston, R., "Ideal concentrators for finite sources and restricted exit angles," *Appl. Opt.,* **vol. 15**, pp. 2880-2883, November 1976

Ramsay, J.F., "Microwave Antenna and Waveguide Techniques Before 1900," *Proc. IRE,* **vol. 46**, pp. 405-415, February 1958

Rowan-Robinson, M., Broadhurst, T., Lawrence, A., McMahon, R.G., Lonsdale, C.J., Oliver, S.J., Taylor, A.N., Hacking, P.B., Conrow, T., Saunders, W., Ellis, R.S., Efstathiou, G.P., Condon, J.J., "A high-redshift IRAS galaxy with huge luminosity — hidden quasar or protogalaxy?," *Nature,* **vol. 351**, pp. 719-721, 27 June 1991

Sarazin, C.L., Bahcall, J.N., "X-Ray Line Emission for Clusters of Galaxies II: Numerical Models," *Astrophys. J. Supp,* **vol. 34**, pp. 451-467, August 1977

Sarazin, C.L., "X-Ray Emission from clusters of galaxies," *Rev. Mod. Phys.,* **vol. 58**, pp. 1-76, January 1986

Sarazin, C.L., *X-Ray Emissions from Clusters of Galaxies,* Cambridge U. Press, 1988

Sarazin, C.L., "Properties of Clusters of Galaxies," in *Cooling Flows in Clusters of Galaxies,* A.C. Fabian, ed., NATO ASI Series C, **vol. 229,** pp. 1-15, Kluwer Academic Publishers 1988

Siegmann, A.E., *An Introduction to Lasers and Masers,* McGraw Hill, 1971

Silk, J., White, S.D.M., "The Determination of q_o Using X-Ray and Microwave Observations of Galaxy Clusters," *Astrophys. J.,* **vol. 226**, pp. L103-L106, 1978

Soucail, G., Fort, B., Mellier, Y., Picat, J.P., "A blue ring-like structure in the center of the A370 cluster of galaxies," *Astron. Astrophys.,* **vol. 172**, pp. L14-L16, 1987

Soucail, G., Mellier, Y., Fort, B., Hammer, F., Mathez, G., "Further data on the blue ring-like structure in A370," *Astron. Astrophys.,* **vol. 184**, pp. L7-L9, 1987

Soucail, G., Mellier, Y., Fort, B., Mathez, G., Cailloux, M., "The giant arc in A370: spectroscopic evidence for gravitational lensing from a source at z=0.724," *Astron. Astrophys.*, **vol. 191**, pp. L19-L21, 1988

Soucail, G., "A Gravitational Telescope in Abell 370: Indeed it Works!" in *Gravitational Lenses*, Moran, J.P., Hewitt, J.N., Lo, K.Y., eds., pp. 127-33, Springer-Verlag, 1989

Soucail, G., Mellier, Y., Fort, B., Mathez, G., Cailloux, M., "Spectroscopy of Arcs in Cl 2244–02 and A370 (A5)," in *Gravitational Lensing*, Y. Mellier, B. Fort, G. Soucail, eds., pp. 291-4, Springer-Verlag, 1990

Southworth G.C., "Some fundamental experiments with wave guides," *Proc. IRE*, **vol. 25**, pp. 807-822, July 1937

Southworth, G.C., "Microwave Radiation from the Sun," *J. Franklin Inst.*, **vol. 239**, pp. 285-297, 1945

Sunyaev, R.A., Zel'dovich, Ya.B., "The Observation of Relic Radiation as a Test of the Nature of X-Ray Radiation from the Clusters of Galaxies," *Comments on Astrophysics and Space Physics*, **vol. 4**, pp. 173-178, 1972

Sunyaev, R.A., Zel'dovich, Ya.B., "The velocity of clusters of galaxies relative to the microwave background. The possibility of its measurement," *Mon. Not. R. astr. Soc.*, **vol. 190**, pp. 413-20, 1980

Sunyaev, R.A., Zel'dovich, Ya.B., "Microwave Background Radiation as a Probe of the Contemporary Structure and History of the Universe," *Ann. Rev. Astron. Astrophys.*, **vol. 18**, pp. 537-560, 1980

Snyder, A.W., Love, J.D., *Optical Waveguide Theory*, Chapman & Hall Ltd., 1983

Tammann, G.A., Sandage, A., "The Stellar Content and Distance of the Galaxy NGC 2403 in the M81 Group," *Astrophys. J.*, **vol. 151**, pp. 825-60, March 1968

Taub, J.J., Hindin, H.J., Hinckelmann, O.F., Wright, M.L., "Submillimeter Components Using Oversize Quasi-Optical Waveguide," *IEEE Trans. Microwave Theory & Techniques*, **vol. 11**, pp. 338-345, September 1963

Telesco, C.M., Harper, D.A., "Galaxies and Far Infrared Emission," *Astrophys. J.*, **vol. 235**, pp. 392-404, 1980

Thomas, B.MacA., "Design of Corrugated Conical Horns," *IEEE Trans. Antennas & Propagation*, **vol. 26**, pp. 367-372, 1978

Torchinsky, S.A., "Analysis of a Conical Horn fed by a Slightly Oversized Waveguide," *Int. J. IR & MM Waves*, **vol. 11**, pp. 791-808, July 1990

Tyson, J.A., "Lensing the Background Population of Galaxies," in *Gravitational Lensing*, Y. Mellier, B. Fort, G. Soucail, eds., pp. 230-5, Springer-Verlag, 1990

Weber, E., "The Evolution of Scientific Electrical Engineering," *IEEE A & P Magazine*, **vol. 33**, pp. 12-16, February 1991

Weinberg, S., *Gravitation and Cosmology*, John Wiley & Sons, Inc., 1972

White, S.D.M., Silk, J., "The X-Ray Structure of Two Rich Galaxy Clusters and its Implications for the Detectability of Microwave Diminutions," *Astrophys. J.*, **vol. 241**, pp. 864-874, 1980

White, S.D.M., Silk, J., Henry, J.P., "The X-Ray Structure of a Galaxy Cluster at $z = 0.54$: Implications for Cluster Evolution and Cosmology," *Astrophys. J.*, **vol. 251**, pp. L65-L68, December 1981

Winston, R., "Light Collection within the Framework of Geometrical Optics," *J.Opt.Soc.Am.*, **vol. 60**, pp. 245-247, February 1970

Wood, P.J., *Reflector Antenna Analysis and Design*, IEE EM Series No. 7, Peter Peregrinus Ltd. on behalf of IEE, 1980

Wylde, R.J., "Millimetre-wave Gaussian beam-mode optics and corrugated feed horns," *IEE Proc. Part H*, **vol. 131**, pp. 258-262, August 1984

Wynn-Williams, G., *communication to W.K. Gear*, 31 May, 1988, copied to SCUBA co-investigators.

Zeldovich, Ya.,B., Syunyaev, R.A., "The Interaction of Matter and Radiation in a Hot-Model Universe," *Astrophys. Space Sci.*, **vol. 4**, pp. 301-316, 1969

APPENDICES

A Cylindrical Waveguide Modes

Since the devices dealt with in Part II all have cylindrical symmetry, the analyses always begin with the fields that satisfy Maxwell's equations in a cylinder with perfectly conducting walls. These are the TE_{nm} and TM_{nm} cylindrical waveguide modes and they are written out explicitly here. Maxwell's equations in the absence of free charges take the following form:

$$\begin{aligned} \vec{\nabla}\cdot\vec{E} &= 0 & \vec{\nabla}\cdot\vec{H} &= 0 \\ \vec{\nabla}\times\vec{E} &= -\mu\frac{\partial\vec{H}}{\partial t} & \vec{\nabla}\times\vec{H} &= \varepsilon\frac{\partial\vec{E}}{\partial t} \end{aligned} \tag{A.1}$$

These can be recast into the wave equation which must be satisfied by each component of the EM fields. However, it is useful to consider the problem in terms of the direction of propagation, and the components transverse to this direction. Thus, the normal components must satisfy the wave equation:

$$\nabla^2 E_z - \frac{1}{c^2}\frac{\partial^2 E_z}{\partial t^2} = 0, \tag{A.2a}$$

$$\nabla^2 H_z - \frac{1}{c^2}\frac{\partial^2 H_z}{\partial t^2} = 0, \tag{A.2b}$$

and the transverse components are related to the normal according to

$$\vec{E}_\perp = \frac{1}{\mu\varepsilon\omega^2 - k^2}\left[-i\mu\hat{z}\times\vec{\nabla}_\perp H_z + ik\vec{\nabla}_\perp E_z\right] \tag{A.3a}$$

$$\vec{H}_\perp = \frac{1}{\mu\varepsilon\omega^2 - k^2}\left[i\varepsilon\omega\hat{z}\times\vec{\nabla}_\perp E_z + i\mu k\vec{\nabla}_\perp H_z\right]. \tag{A.3b}$$

Solutions of the kind which have no normal magnetic field are called the Transverse Magnetic (TM) and those with no normal electric field are the Transverse Electric (TE). In cylindrical geometry, bounded by a perfect conductor, these are the following:

$$\vec{E}_{nm}^{\mathrm{TE}} = \left(\frac{-\omega a}{2\gamma_{nm}}\right)\left[J_{n-1}\left(\gamma_{nm}\tfrac{r}{a}\right)\, e^{i(n-1)\theta} + J_{n+1}\left(\gamma_{nm}\tfrac{r}{a}\right)\, e^{i(n+1)\theta}\right]\hat{\mathrm{x}}$$
$$+ \left(\frac{-i\omega a}{2\gamma_{nm}}\right)\left[J_{n-1}\left(\gamma_{nm}\tfrac{r}{a}\right)\, e^{i(n-1)\theta} - J_{n+1}\left(\gamma_{nm}\tfrac{r}{a}\right)\, e^{i(n+1)\theta}\right]\hat{\mathrm{y}} \tag{A.4a}$$

$$\vec{H}_{nm}^{\mathrm{TE}} = \left(\frac{ika}{2\mu\gamma_{nm}}\right)\left[J_{n-1}\left(\gamma_{nm}\tfrac{r}{a}\right)\, e^{i(n-1)\theta} - J_{n+1}\left(\gamma_{nm}\tfrac{r}{a}\right)\, e^{i(n+1)\theta}\right]\hat{\mathrm{x}}$$
$$+ \left(\frac{-ka}{2\mu\gamma_{nm}}\right)\left[J_{n-1}\left(\gamma_{nm}\tfrac{r}{a}\right)\, e^{i(n-1)\theta} + J_{n+1}\left(\gamma_{nm}\tfrac{r}{a}\right)\, e^{i(n+1)\theta}\right]\hat{\mathrm{y}} \tag{A.4b}$$
$$+ \tfrac{1}{\mu}J_n\left(\gamma_{nm}\tfrac{r}{a}\right)\, e^{in\theta}\hat{\mathrm{z}}$$

$$\vec{E}_{nm}^{\mathrm{TM}} = \left(\frac{ika}{2\gamma_{nm}}\right)\left[J_{n-1}\left(\gamma_{nm}\tfrac{r}{a}\right)\, e^{i(n-1)\theta} - J_{n+1}\left(\gamma_{nm}\tfrac{r}{a}\right)\, e^{i(n+1)\theta}\right]\hat{\mathrm{x}}$$
$$+ \left(\frac{-ka}{2\gamma_{nm}}\right)\left[J_{n-1}\left(\gamma_{nm}\tfrac{r}{a}\right)\, e^{i(n-1)\theta} + J_{n+1}\left(\gamma_{nm}\tfrac{r}{a}\right)\, e^{i(n-1)\theta}\right]\hat{\mathrm{y}} \tag{A.4c}$$
$$+ J_n\left(\gamma_{nm}\tfrac{r}{a}\right)\, e^{in\theta}\hat{\mathrm{z}}$$

$$\vec{H}_{nm}^{\mathrm{TM}} = \left(\frac{-\omega a\varepsilon}{2\gamma_{nm}}\right)\left[J_{n-1}\left(\gamma_{nm}\tfrac{r}{a}\right)\, e^{i(n-1)\theta} + J_{n+1}\left(\gamma_{nm}\tfrac{r}{a}\right)\, e^{i(n+1)\theta}\right]\hat{\mathrm{x}}$$
$$+ \left(\frac{i\omega a\varepsilon}{2\gamma_{nm}}\right)\left[J_{n-1}\left(\gamma_{nm}\tfrac{r}{a}\right)\, e^{i(n-1)\theta} - J_{n+1}\left(\gamma_{nm}\tfrac{r}{a}\right)\, e^{i(n-1)\theta}\right]\hat{\mathrm{y}} \tag{A.4d}$$

where a is the radius of the guide, $\omega = 2\pi\nu$ is the frequency in radians per second, ε is the electric permitivity, and μ is the magnetic permeability. The impedence of free space is $\mathcal{Z}_0 = \sqrt{\mu/\varepsilon} = 377\Omega$, and the speed of light in a vacuum is $c = 1/\sqrt{\varepsilon\mu} = 2.9979\times10^{8}\mathrm{m\,s^{-1}}$. For the TE_{nm} modes, the γ_{nm} are the m^{th} zero of the first derivative *w.r.t.* the argument of Bessel function order n, and for the TM_{nm} modes they are the m^{th} zero of Bessel function order n. The wavenumber in the guide is

$$k = (\omega/c)\sqrt{1-(\gamma_{nm}/\gamma)^2} \tag{A.4e}$$

where γ is a dimensionless frequency parameter related to the frequency and the radius of the guide

$$\gamma = \omega a / c \tag{A.4f}$$

The power in each cylindrical wave mode is the integrated Poynting vector over the cross section of the guide:

$$\begin{aligned} \mathcal{P}_{nm} \left\{ \begin{smallmatrix} \text{TE} \\ \text{TM} \end{smallmatrix} \right\} &= \frac{1}{\pi a^2} \int_0^a \int_0^{2\pi} r \, d\theta \, dr \left| \vec{E}_{nm} \times \vec{H}^*_{nm} \right| \\ &= \left\{ \begin{smallmatrix} 1/\mu \\ \epsilon \end{smallmatrix} \right\} \left(\frac{\omega k^*_{nm} a^2}{4 \mu \gamma^2_{nm}} \right) P_{nm} \end{aligned} \tag{A.4g}$$

where

$$P_{nm} = \int_0^1 \rho \, d\rho \left[J^2_{n-1} (\gamma_{nm} \rho) + J^2_{n+1} (\gamma_{nm} \rho) \right] . \tag{A.4h}$$

Note that the axial component of the magnetic or electric fields in the TE or the TM modes doesn't contribute to the power flow.

B Laguerre–Gauss Beams

The propagation of electromagnetic radiation in free space when it emanates from a longitudinal source, such as a laser, or a feedhorn, is conveniently expressed in terms of the Laguerre–Gauss beams. This was first introduced in 1966 by Kogelnik & Li in order to analyze lasers. Reviews of Gaussian Beam theory can be found in Siegmann [1971], Marcuse [1972], and Martin & Lesurf [1978]. The subject of Quasi-Optics is extensively treated by Goldsmith [1982]. A derivation is presented in this appendix.

The wave equation,

$$\nabla^2\Psi - \frac{1}{c^2}\frac{\partial^2\Psi}{\partial t^2} = 0 \tag{B.1}$$

as in the previous appendix, can be reduced to the following problem when it is assumed that the propagation is strongly directional along the z axis. Substituting

$$\Psi(x,y,z) = \psi(x,y,z)e^{i\omega t - i\omega z/c} \tag{B.2}$$

where $\psi(x,y,z)$ is a *slowly varying* function in z reduces the wave equation to the Laplace equation,

$$\nabla^2\psi = 0. \tag{B.3}$$

Since ψ is slowly varying along the axis of propagation, the second ~~derivates~~ derivatives in z are neglected as being second order small compared to other terms. This leads to

$$\nabla_\perp^2\psi - 2i\omega\psi/c = 0, \tag{B.4}$$

and the propagation constant is set equal to ω/c as in a plane wave solution. In cylindrical polar geometry, the solution to Eq. B.4 is that used in Chapter 7:

$$\psi_{nm} = \frac{1}{\sqrt{\pi}\,W}\left(\frac{2r^2}{W^2}\right)^{n/2} L_{nm}\left(\frac{2r^2}{W^2}\right)\exp\left(-\frac{r^2}{W^2} + i\frac{\pi r^2}{\lambda R} + i\Phi + in\theta\right). \tag{B.5a}$$

The Laguerre polynomials are given by the generating function

$$L_{nm}(x) = \frac{d^n}{dx^n} L_{0\,m+n}, \quad L_{0m} = e^x \frac{d^m}{dx^m} \left(e^{-x} x^m\right), \tag{B.5b}$$

which is the well known Rodrigues' formula.

$$W = W_0 \sqrt{1 + \left(\lambda z / \pi W_0^2\right)^2}, \tag{B.5c}$$

and

$$R = z \left[1 + \left(\pi W_0^2 / \lambda z\right)^2\right]. \tag{B.5d}$$

W_0 is the beam waist radius which occurs at the focus of the L-G beam ($z = 0$), and Φ is the phase slippage, in addition to that of a spherical wave, relative to the fundamental L-G mode,

$$\Phi = (2m + n)\mathrm{Tan}^{-1}\left(z\lambda / \pi W_0^2\right). \tag{B.5e}$$

The functions are normalized such that the power in a L-G beam mode is unity. That is,

$$1 = \int_0^\infty \int_0^{2\pi} r d\theta\, dr\, 2\Psi_{nm} \cdot \Psi_{nm}^*.$$

The Gaussian Beam Telescope

One of the great advantages of using Gaussian beams apart from its convenient description of wave propagation in free space, is its use for analyzing optical systems. The Gaussian beam approach allows the use of geometric optic techniques to determine the beam configuration throughout an optical train, as well as the focus locations. This is the relatively new field of Quasi-Optics.

In analogy to a spherical wave, a complex wavefront radius can be defined for the Gaussian beam of Eq. B.5a,

$$1/q = 1/R + i\lambda/\pi W^2, \tag{B.6}$$

and the Gaussian beam will obey the normal lens law for determining the focus of a beam on either side of a lens. *viz.*

$$1/q_1 - 1/q_2 = 1/f. \tag{B.7}$$

At the lens itself, the waist radius of the incoming beam must equal that of the outgoing beam,

$$W_{01}\sqrt{1 + (\lambda d_1/\pi W_{01}^2)^2} = W_{02}\sqrt{1 + (\lambda d_2/\pi W_{02}^2)^2}. \tag{B.8}$$

Combining Eqs. B.7 and B.8 derives the position of the focus on the other side of a lens from a beam emanating (*i.e.* with waist radius) at the distance d_1 from a lens.

$$\frac{d_2}{f} = 1 + \frac{d_1/f - 1}{(d_1/f - 1)^2 + (\pi W_{01}^2/\lambda f)^2}. \tag{B.9}$$

One can see immediately that positioning the beam source at the focal distance of the lens ($d_1 = f$) leads to the *frequency independent* position of the beam focus on the other side of the lens at its focal distance. This then advocates an optical train setup in which lenses are separated by the sum of their focal lengths: the Gaussian Beam Telescope. A frequency independent focus is obviously essential in a system which hopes to detect radiation across a finite waveband, such as any continuum receiver.